NTNU – Trondheim
Norwegian University of
Science and Technology

Advanced Mueller Matrix Imaging Ellipsometry

Silicon Strain Imaging, Visualisation of
Collagen Fibre 3-D Orientation &
Development of a Mueller Matrix Imaging
Microscope

Vegard Stenhjem Hagen

Physics
Submission date: August 2014
Supervisor: Morten Kildemo, IFY
Co-supervisor: Magnus Lilledahl, IFY
Mikael Lindgren, IFY

Norwegian University of Science and Technology
Department of Physics

Abstract

A custom built near-infra-red (NIR) Mueller matrix imaging ellipsometer (MMI) based on ferroelectric liquid crystals (FLCs) and waveplates (WPs) is described in detail. The instrument is used to perform strain-induced birefringence imaging of crystalline silicon, and visualise the 3-D orientation of collagen fibres expressing linear retardance.

The development of a spectroscopic Mueller matrix imaging microscope ellipsometer (μMMI) is presented. Preliminary verification indicate that the constructed μMMI works as expected.

The theory behind Mueller matrix ellipsometry is outlined, including the description of polarised light, and its representation by the Mueller-Stokes formalism. Detailed analysis of the Mueller matrix, encompassing both the forward polar and the differential decomposition, is presented. These techniques are used in the study of both organic and in-organic samples.

Photoelastic theory is briefly discussed in order to explain the phenomena of birefringence in strained silicon crystals. A simple model is developed in order to estimate the maximum shear-stress. Vertical cross-sections of bi-crystal silicon separated by near-coincident site lattice grain boundaries $\Sigma 9$ and $\Sigma 27a$ ingots are studied using the custom built near NIR MMI at 1300 nm. The obtained images were decomposed using the forward polar decomposition. The resulting optical properties were used to map the internal shear-stress of the samples, found to be in the range of 2.5 MPa to 5 MPa. Further studies are proposed in order to verify the shear-stress estimation technique.

Chicken tendon is imaged at 940 nm with different incidence angles (0° and ±30°) using the custom built MMI. The differential decomposed Mueller matrix measurements were used to calculate the 3-D directional orientation of collagen fibres. Validation of the obtained 3-D directional orientation was done by comparing the results with second-harmonic generation (SHG) images. The two methods were found to be in good agreement.

Development of an optimal broadband spectroscopic Mueller matrix imaging system to work in the range 550 nm to 1150 nm is described. A design similar to the earlier presented MMI based on FLCs and WPs was chosen. The concept of genetic algorithms is introduced and utilised in order to improve on the design. Realisation of the instrument is documented from the choice of components, characterisation, re-optimisation of the design, and lastly, building and verification the instrument.

Sammendrag

Et spesiallaget nær-infrarødt (NIR) Mueller matrise ellipsometer (MMI) basert på ferroelektriske flytende krystaller (FLCs) og bølgeplater (WPs) er beskrevet. Dette instrumentet blir brukt for å avbilde belastnings-bifringens i krystallinsk silisium og visualisering av lineært retarderende kollagenfibre.

Utvikling av et nytt spektroskopisk Muellermatrise avbildende mikroskop ellipsometer (μMMI) er fremstilt. Innledende verifisering indikerer at det konstruerte instrumentet fungerer som forventet.

Teorien rundt Mueller matrise ellipsometri blir introdusert. Dette inkluderer beskrivelsen av polarisert lys og dets representasjon ved Mueller-Stokes formalismen. Detaljert analyse av Mueller matriser basert på både fremad-polar- og differensielldekomponering er presentert. Disse teknikkene blir så brukt i studie av både organisk og uorganisk materiale.

Fotoelastisk teori er kort diskutert for å kunne forklare bifringens i anstrengte silisiumkrystaller, og en enkel model for å estimere maksimalt skjær-stress ble utviklet. Vertikale tverrsnitt av to-krystallinsk silisium separert ved nær-sammenfallende gitterstruktur korngrenser $\Sigma 9$ og $\Sigma 27a$ blokker ble undersøkt med den spesialkonstruerte MMIen ved 1300 nm. Målingene ble deretter dekomponert ved å bruke fremad-polar dekomponering. De resulterende optiske egenskapene ble brukt til å kartlegge internt skjærstress i prøvene. Skjærstress ble funnet til å være i området 2,5 MPa til 5 MPa. Fremtidige studier er foreslått for å verifisere denne teknikken.

Teorien bak 3-dimensjonal retnings-avbilding er introdusert. Kyllingsener er avbildet ved 940 nm med forskjellige insidens-vinkler (0° og ±30°) ved å bruke den spesiallagde MMIen. Differensialdekomponerte Mueller matrise målinger ble brukt til å regne ut 3-D orienteringen av kollagenfibre. Validering av den oppnådde 3-D retningen ble gjort ved å sammenligne resultatet med andre-harmonisk genererte (SHG) bilder. Begge metodene ble funnet til å stemme bra overens.

Prosessen bak designet av et optimalt bredbånds spektroskopisk Mueller matrise avbildingsystem i området 550 nm til 1150 nm er beskrevet. Et design likt den tidligere beskrevne MMIen basert på FLCer og bølgeplater ble valgt. Konseptet bak genetiske algoritmer er introdusert og brukt for å forbedre designet. Realisering av instrumentet er dokumentert fra valg av komponenter, karakterisering, re-optimalisering av designet, og til slutt bygging og verifisering av instrumentet.

Acknowledgements

This Master's thesis is the culmination of work done during a 2 year MSc in Physics at NTNU. The project has been carried out at the Applied Optics Group, Department of Physics at the Norwegian University of Science and Technology under the supervision of professor Morten Kildemo. I thank you for your guidance and a challenging, but immensely rewarding assignment.

I would also like to thank Pål Gunnar Ellingsen and Lars Martin Sandvik Aas for their guidance, always answering my questions and instructing me in proper scientific work. I am also greatly appreciative of the opportunity to collaborate with Antoine Autruffe on an upcoming article, and with Pål Gunnar Ellingsen on a published article.

The final part of this thesis could not have been completed without the expertise of Solveig Rønning Almli at Finmekanisk verksted in realising my design for a component holder, and the provision of an old microscope by Astrid Bjørkøy at the Depertment of Physics. I thank you for being able to successfully complete such an ambitious and fun project.

A very special thanks goes to Camila Holven Sanhueza for providing me with ample moral support and helping me keep on track during the work in this thesis.

Trondheim, August 2014

Vegard Stenhjem Hagen

The world is not beautiful,
therefore it is.
– **Kino's Journey**, Keiichi Sigsawa

Contents

Abstract iii

Sammendrag v

Acknowledgements vii

List of abbreviations xiii

I. General Theory and Concepts 1

1. Introduction 3
1.1. Outline 4

2. Background & theory 5
2.1. Electromagnetic waves 5
2.2. Polarisation of light 5
2.3. Representation of polarised light 7
2.4. The Poincaré sphere 8
2.5. The Mueller matrix 9
2.5.1. Selected important Mueller matrices 11
2.6. Physical realisable Mueller matrices 13
2.6.1. Cloude filtration 14
2.7. Optics of anisotropic media 15
2.7.1. Birefringent media 16
2.7.2. Birefringence due to strain in crystal silicon 16
2.7.3. In-plane stress direction. 20
2.8. Polarimeter design 21
2.9. Genetic algorithms 22

3. Ellipsometry **25**
3.1. Mueller matrix ellipsometry 26
3.2. Calibration of a Mueller matrix ellipsometer 28
3.2.1. Eigenvalue calibration method 28
3.2.2. Validation 31

4. Analysing the Mueller matrix **33**
4.1. Forward product decomposition 34
4.2. Permutations of the forward product decomposition 36
4.2.1. Reverse polar decomposition 37
4.2.2. Symmetric decomposition 38
4.3. Differential decomposition 38
4.4. Mueller matrix roots decomposition 41
4.5. Out of plane directional calculation based on different incidence angles 42

II. Mueller Matrix Measurements and Analysis of the Results **45**

5. Performing Mueller matrix measurements **47**
5.1. Hardware 47
5.2. LabVIEW operation 48
5.2.1. GUI 49
5.2.2. Initial settings 50
5.2.3. Calibration pane 51
5.2.4. Stage control 52
5.2.5. Measurement tab 53
5.2.6. Calculation tab 54
5.2.7. Error messages 55
5.3. Remarks on the code 56
5.4. Calibration results 57
5.4.1. Image resolution 59

6. Results and discussion **61**
6.1. Strain induced birefringence in two bi-crystal silicon ingots 61
6.1.1. Sample preparation 62
6.1.2. Measurements 64
6.1.3. Near-CSL grain boundary $\Sigma 9$ 66
6.1.4. Near-CSL grain boundary $\Sigma 27a$ 69
6.1.5. Conclusion 70
6.2. 3-D Visualisation of collagen fibres 72
6.2.1. Sample preparation 72
6.2.2. Measurements 73
6.2.3. Results 73
6.2.4. Conclusion 75

III. Development of a Spectroscopic Mueller Matrix Imaging Microscope **79**

7. Development **81**
7.1. Preliminary design 81
7.2. Realisation 84
7.2.1. Characterisation and design optimisation 84
7.2.2. Assembly 87
7.3. Verification 89
7.4. Conclusion 94

IV. Afterword **95**

8. Final thoughts and outlook **97**
8.1. Instrumentation 97
8.2. Silicon strain imaging 97
8.3. Visualisation of 3-D structures 98
8.4. Mueller matrix imaging microscopy 98

References **99**

Appendices **109**

A. Selected Jones matrices **109**

B. Modified Dirac matrices of $SU(4)$ **111**

C. Orientation dependent stress-optic coefficient **113**

D. Coordinate transfer matrices **117**

E. Implementation of the ECM-routine in MATLAB **119**

F. An unrealisable polarimeter design **127**

G. Schematics for uMMI PSG/PSA **129**

H. Datasheet for CODIXX colorPol VISIR polarisers **139**

Glossary **141**

List of abbreviations

EM . . . . . ElectroMagnetic

MMI . . . . . Mueller Matrix (transmission) Imaging Ellipsometer.

μMMI . . . . . Mueller Matrix (transmission) Imaging Microscope Ellipsometer.

PSA . . . . . Polarisation State Analyser.

PSG . . . . . Polarisation State Generator.

ROI . . . . . Region of Interest.

DOP . . . . . Degree of Polarisation.

FLC . . . . . Ferroelectric Liquid Crystal.

WP . . . . . Waveplate.

QWP . . . . . Quarter Waveplate.

HWP . . . . . Half Waveplate.

ECM . . . . . Eigenvalue Calibration Method.

LED . . . . . Light Emitting Diode.

GUI . . . . . Graphical User Interface.

GB . . . . . Grain Boundary.

CSL . . . . . Coincident Site Lattice.

mc-Si . . . . . Multicrystalline Silicon

EBSD . . . . . Electron BackScatter Diffraction

SHG . . . . . Second Harmonics Generation.

NIR . . . . . Near Infra-Red.

VIS . . . . . VISible light.

∇ . . . . . Del-operator, $\nabla = \hat{\mathbf{x}}\frac{\partial}{\partial x} + \hat{\mathbf{y}}\frac{\partial}{\partial y} + \hat{\mathbf{z}}\frac{\partial}{\partial z}$.

$\mathbb{R}$ . . . . . Set of real numbers.

$\mathbb{C}$ . . . . . Set of complex numbers.

i . . . . . Imaginary unit, $\mathrm{i} = \sqrt{-1}$.

$\Re\{\cdot\}$ . . . . . Real part of a complex number.

$\Im\{\cdot\}$ . . . . . Imaginary part of a complex number.

$\mathbb{M}_{n\times m}(\mathbb{R})$ . . . . . The space of real valued $n \times m$ matrices.

$\mathbf{M}$ . . . . . Boldface upper-case letter often represents a theoretical matrix.

$\mathbf{I}_{n\times n}$ . . . . . The $n \times n$ Identity matrix.

$\mathbf{b}$ . . . . . A measured matrix or a sub-matrix.

$\vec{J}$ . . . . . A column or row vector.

$\widehat{U}$ . . . . . A unit vector.

$[\mathbf{X}]_U$ . . . . . The matrix $\mathbf{X}$ expressed in the elements of the basis U.

$\sum_{i,j=n}^{m}$ . . . . . Double sum over both i and j from n to m.

$||\cdot||$ . . . . . The euclidean 2-norm.

$\cdot^T$ . . . . . Transpose operation.

$\overline{\cdot}$ . . . . . Complex conjugate operation.

$\cdot^*$ . . . . . The adjoint, or complex-conjugate transpose operation, $\cdot^* = (\overline{\cdot})^T$.

$\cdot^{-1}$ . . . . . The inverse.

$\cdot^\dagger$ . . . . . Moore-Penrose pseudo-inverse.

$\otimes$ . . . . . Kronecker product.

Part I.

General Theory and Concepts

Chapter 1

Introduction

One of the fundamental properties of light, or more generally electromagnetic (EM) waves, is its state of polarisation. Other fundamental properties of EM waves include intensity, wavelength and coherence.[1] A method for measuring the polarisation state of light was introduced by the German physicist Paul Drude in two articles published in 1889.[2,3] These articles describe an instrument known as an ellipsometer, and lay the foundation for the work presented in this thesis.

Many naturally occurring phenomena produce polarised light, e.g. the partial polarisation of the sky due to Rayleigh scattering,[4] or light reflected from a surface. Polarisation effects are also exploited to display images in liquid crystal displays (LCD), where (in the case of a twisted nematic LCD screen) small cells of liquid crystals are sandwiched between two crossed linear polarisers and two electrodes to regulate the degree of transmitted light.[5] By adjusting the voltage between the electrodes, the liquid crystals will twist and alter the orientation of the polarisation, thus changing the degree of light transmitted through the cell.

Polarised light offers non-destructive methods for probing materials. Photoelasticity is one such property, which can easily be demonstrated by holding a piece of clear plastic between two polarisers. In figure 1.1 photoelasticity is demonstrated by holding a ruler between an LCD monitor and a linear polarisation filter. Internal stresses of the ruler make the plastic act as a waveplate, thereby changing the polarisation of the light. The rainbow-like pattern is caused by a wavelength dependent phase-shift, or retardation, of the light, resulting in some wavelengths having a higher transmittance-ratio through the polarisation filter. This effect is the basis of the measurements done in section 6.1 and is breifly explained in section 2.7.

The structure of a material can also express polarising effects. An example of this is called form birefringence and can observed from e.g. long strands of molecules. Form birefringence is utilised in section 6.2 to investigate the 3-dimensional structure of collagen fibres in chicken tendon.

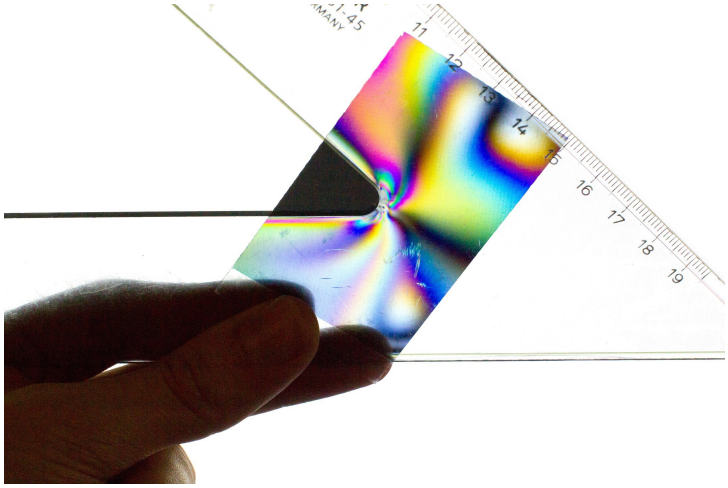

Figure 1.1: Photoelasticity demonstrated by holding a plastic ruler between an LCD monitor and a linear polarisation filter. Note that the filter is essentially blocking the light that does not travel through the ruler.

1.1. Outline

In Part I, necessary background theory is presented. Chapter 2 introduces the Mueller-Stokes formalism for describing polarised which is used in this thesis. Some polarisation-state changing mechanisms is briefly introduced before moving on to ellipsometry in chapter 3. Here traditional ellipsometry is outlined before talking about Mueller matrix ellipsometry and the eigenvalue calibration method (ECM) for MMI systems. Methods for analysing a measured Mueller matrix is presented in chapter 4.

Part II starts with chapter 5 describing the MMI instrument used for most of the measurements in this thesis. Chapter 6 presents measurements quantifying the magnitude and direction of shear stresses in a silicon wafer, and measurements visualising the 3-dimensional structure of collagen fibres.

A successful design and implementation of a new Mueller matrix imaging microscope (μMMI) is documented in Part III. This documentation starts out with the preliminary design, borrowing from earlier designs and ideas. The acquired components needed to realise the design is quantified and carefully aligned before being installed in an old microscope in order to validate the design.

Part IV closes the thesis with an afterword, containing final comments and musings on further work.

Chapter 2

Background & theory

2.1. Electromagnetic waves

Classically, electromagnetic waves in can be described by Maxwell's equations,

$$\nabla \cdot \vec{E} = \frac{1}{\epsilon_0}\rho, \qquad \nabla \times \vec{E} = -\frac{\partial \vec{B}}{\partial t},$$
$$\nabla \cdot \vec{B} = 0, \qquad \nabla \times \vec{B} = \mu_0 \vec{J} + \mu_0 \epsilon_0 \frac{\partial \vec{E}}{\partial t},$$

here represented in their general differential form as in the book *Introduction to Electrodynamics*.[6] $\vec{E}$ represents the electric field and $\vec{B}$ the magnetic field. The constants ϵ_0 and μ_0 are the permittivity and the permeability of free space, respectively. ρ represents charge density, t time, and $\vec{J}$ electric current density. ∇ is the Del-operator.

In the case where both the magnetic and electrical field, as well as the direction of propagation are mutually perpendicular, the oscillation orientation of the electromagnetic field component can be described by the transversal polarisation of the wave.

Generally, there is a possibility for longitudinal polarisation.[7,8] A longitudinal polarised beam requires radially polarised light, and current design allows for distance up to fifty thousand wavelengths of the longitudinal beam.[9] Although these beams express some desirable properties like a divergence free beam,[8] they will not be further expanded on in this thesis as they are considered a special case.

2.2. Polarisation of light

Wavelength, frequency, and polarisation are fundamental properties of light. According to Chipman,[10] fully polarised light is defined as light with a fixed elliptical polarisation state as shown in figure 2.1. One solution to Maxwell's equations is a monochromatic plane wave, travelling in the z-direction with no explicit x or y dependence.

The electric field of this plane wave can be described as[11]

$$\vec{E}(z,t) = \Re\{E_x(z,t)\}\hat{\mathbf{x}} + \Re\{E_y(z,t)\}\hat{\mathbf{y}} \tag{2.1}$$

where $\hat{\mathbf{x}}$ and $\hat{\mathbf{y}}$ are the unit vectors in x and y direction respectively, and $\Re\{\cdot\}$ denotes the real value. The orthogonal field components $E_x(z,t)$ and $E_y(z,t)$ are given by the complex fields

$$\begin{aligned} E_x(z,t) &= \mathscr{E}_x \exp[\mathrm{i}(\omega t - kz + \delta_x)], \\ E_y(z,t) &= \mathscr{E}_y \exp[\mathrm{i}(\omega t - kz + \delta_y)]. \end{aligned} \tag{2.2}$$

Here $\mathscr{E}_i$ is the real amplitude of the electric field in the i-direction, $k = 2\pi/\lambda$ is the wave number, in which λ represents the wavelength, ω is the angular frequency and t is the time. δ_i is the phase factor of the respective field. The polarisation state is

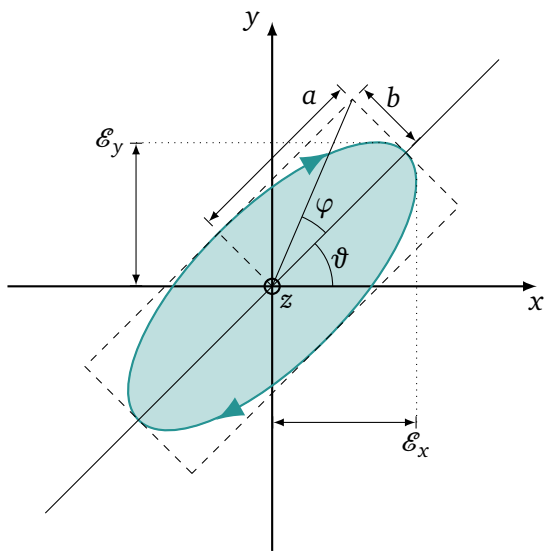

Figure 2.1: The general right-handed polarisation ellipse. The angle ϑ defines the direction of the major axis, whereas the angle φ defines ellipticity which is the ratio b/a. Given $\varrho = \mathscr{E}_y/\mathscr{E}_x$, $\tan 2\vartheta = (2\varrho/(1-\varrho^2))\cos\delta$ and $\sin 2\varphi = (2\varrho/(1+\varrho^2))\sin\delta$.

determined by the ratio $\mathscr{E}_x/\mathscr{E}_y$ and $\delta = \delta_y - \delta_x$. Equation (2.2) can be rewritten as[1]

$$\left(\frac{\mathfrak{E}_x}{\mathscr{E}_x}\right)^2 + \left(\frac{\mathfrak{E}_y}{\mathscr{E}_y}\right)^2 - 2\left(\frac{\mathfrak{E}_x\mathfrak{E}_y}{\mathscr{E}_x\mathscr{E}_y}\right)\cos(\delta) = \sin^2(\delta), \tag{2.3}$$

where $\mathfrak{E}_i = \Re\{E_i\}$. Comparing this form with the general equation of an ellipse found in mathematical texts covering conic sections (e.g. Elementary Linear Algebra by Anton & Rorres[12]), it is evident that all transversal polarisation states can be described by a rotated ellipse. A linear polarisation state is given by $\delta = n\pi$ where $n \in \mathbb{N}$, while $\mathscr{E}_x = \mathscr{E}_y$ and $\delta = n\pi + \pi/2$ gives circular polarised light.

Hauge et al.[11] defines right-handed polarisation as having an instantaneous electric field vector forming a right-handed helix in space. This definition is equivalent with the

electric field vector of right-handed polarised light rotating in a clockwise fashion in the plane perpendicular to the propagation axis, looking into the source (see fig. 2.1). Equivalent, given the condition $\sin\delta > 0$, equation (2.3) will describe right-handed polarisation.[13] The reader should note that there exists two opposing definitions on the right/left-handedness of circular polarised light due to historical reasons. The definition presented here will be used throughout this text.

2.3. Representation of polarised light

A common representation of polarised light is the *Jones vector formalism* which is defined as the vector of the plane monochromatic complex field of equation (2.1), with explicit time and space dependencies removed,[14]

$$\vec{J} = \begin{bmatrix} E_x \\ E_y \end{bmatrix} = \begin{bmatrix} \mathscr{E}_x e^{i\delta_x} \\ \mathscr{E}_y e^{i\delta_y} \end{bmatrix}. \tag{2.4}$$

Optical components that change the polarisation state can be described by matrices acting on the Jones vector. The aptly named *Jones matrix*[15] is represented by a 2×2 matrix

$$\mathbf{J} = \begin{bmatrix} a & b \\ c & d \end{bmatrix}, \tag{2.5}$$

where the matrix elements a, b, c and d are complex transmission or reflection coefficients. These coefficients determine the properties of the Jones matrix. An incoming Jones vector $\vec{J}$ is transformed by the Jones matrix $\mathbf{J}$ into an outgoing Jones vector $\vec{J}'$ as

$$\vec{J}' = \mathbf{J}\vec{J}. \tag{2.6}$$

Selected Jones matrices can be found in appendix A for completeness.

Depolarisation of light is a major issue in samples with scattering properties, e.g. biological tissue and structured surfaces such as silicon solar cells. The Jones vector formalism is unsuited to describe partially polarised light. Another formalism, called the *Mueller-Stokes formalism* is preferred in these situations. This formalism is suited to describe unpolarised light, fully polarised light, and partially polarised light, since it is based on average intensity measurements. This basis makes the Mueller-Stokes formalism applicable to quasi-monochromatic light (light with a finite bandwidth). The Mueller-Stokes formalism is also arguably easier than the Jones formalism as the former only uses real numbers, while the latter uses complex numbers. Other formalisms for describing partially polarised light exists,[16] but will not be further discussed in this thesis.

Hauge et al.[11] defines the Stokes vector as a column vector with four elements

$$\vec{S} = \begin{bmatrix} s_0 \\ s_1 \\ s_2 \\ s_3 \end{bmatrix} = \begin{bmatrix} I_{0^\circ} + I_{90^\circ} \\ I_{0^\circ} - I_{90^\circ} \\ I_{45^\circ} - I_{-45^\circ} \\ I_R - I_L \end{bmatrix} = \begin{bmatrix} \langle \mathscr{E}_x^2 \rangle + \langle \mathscr{E}_y^2 \rangle \\ \langle \mathscr{E}_x^2 \rangle - \langle \mathscr{E}_y^2 \rangle \\ 2\langle \mathscr{E}_x \mathscr{E}_y \rangle \cos\delta \\ 2\langle \mathscr{E}_x \mathscr{E}_y \rangle \sin\delta \end{bmatrix}, \tag{2.7}$$

where I is the intensity of the subscripted polarisation relative to the x-axis (0°), right circular (R), or left circular (L) polarised light. $\langle\cdot\rangle$ signifies the time average. The parameter s_0 represents the total intensity of the light, s_1 the difference in intensity between linear vertical (x) and horizontal polarised (y) light, s_2 the intensity difference between linear (+45°) and (−45°) polarised light, and s_3 the difference in intensity between right and left circular polarised light.

The degree of polarisation (DOP) can now be expressed as[10]

$$\mathrm{DOP} = \frac{\sqrt{s_1^2 + s_2^2 + s_3^3}}{s_0}. \tag{2.8}$$

For fully polarised light $s_0 = \sqrt{s_1^2 + s_2^2 + s_3^3}$, and the degree of polarisation is unity, while DOP = 0 represents unpolarised light. It is worth noting that $s_0 = I_{0^\circ} + I_{90^\circ} = I_{45^\circ} + I_{-45^\circ} = I_R + I_L$ depending on which basis is used.

Different types of polarised light can be represented in the following manner in both Stokes and Jones formalism.

Polarisation	Stokes vector	Jones vector
Linear Horizontal	$\begin{bmatrix}1 & 1 & 0 & 0\end{bmatrix}^T$	$\begin{bmatrix}0 & 1\end{bmatrix}^T$
Linear Vertical	$\begin{bmatrix}1 & -1 & 0 & 0\end{bmatrix}^T$	$\begin{bmatrix}1 & 0\end{bmatrix}^T$
Linear + 45°	$\begin{bmatrix}1 & 0 & 1 & 0\end{bmatrix}^T$	$\frac{1}{\sqrt{2}}\begin{bmatrix}1 & 1\end{bmatrix}^T$
Linear − 45°	$\begin{bmatrix}1 & 0 & -1 & 0\end{bmatrix}^T$	$\frac{1}{\sqrt{2}}\begin{bmatrix}1 & -1\end{bmatrix}^T$
Right Circular	$\begin{bmatrix}1 & 0 & 0 & 1\end{bmatrix}^T$	$\frac{1}{\sqrt{2}}\begin{bmatrix}1 & -\mathrm{i}\end{bmatrix}^T$
Left Circular	$\begin{bmatrix}1 & 0 & 0 & -1\end{bmatrix}^T$	$\frac{1}{\sqrt{2}}\begin{bmatrix}1 & +\mathrm{i}\end{bmatrix}^T$
Unpolarised	$\begin{bmatrix}1 & 0 & 0 & 0\end{bmatrix}^T$	N/A

2.4. The Poincaré sphere

A more geometric approach for describing polarised light is the Poincaré sphere.[17] A Stokes vector can be traced on the Poincaré sphere using the vector defined by

$$\vec{u} = \frac{1}{s_0}\begin{bmatrix}s_1 \\ s_2 \\ s_3\end{bmatrix}.$$

Starting with unpolarised light at the origin, the degree of polarisation increases towards the surface of the sphere where the light is fully polarised. Stokes vectors

pointing to the upper pole of the sphere are defined as right polarised, while vectors pointing toward the lower pole are left polarised. The latitude in between determine the ellipticity. Linear polarised light is represented along the equator with the orientation determined by the meridian. A representation of the Poincaré sphere is found in figure 2.2.

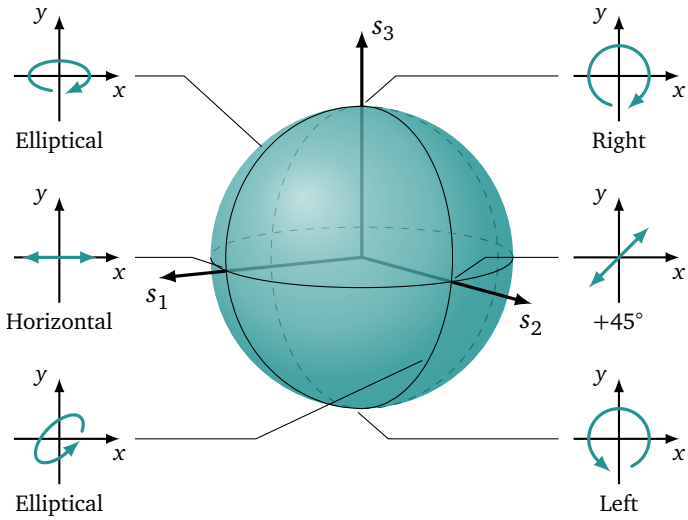

Figure 2.2: The Poincaré sphere with select polarisation states indicated. The degree of polarisation increases towards the surface of the sphere where the light is fully polarised. An Illustration by F. Jonsson[18] inspired this figure.

2.5. The Mueller matrix

Analogous to the Jones vector and its transformation matrices, the Stokes vector is transformed by *Mueller matrices*. The Mueller matrix is a 4×4 matrix denoted as[11]

$$\mathbf{M} = \begin{bmatrix} m_{11} & m_{12} & m_{13} & m_{14} \\ m_{21} & m_{22} & m_{23} & m_{24} \\ m_{31} & m_{32} & m_{33} & m_{34} \\ m_{41} & m_{42} & m_{43} & m_{44} \end{bmatrix}. \tag{2.9}$$

Optical components, such as polarisers, retarders, diattenuators, depolarisers, etc. can be described using Mueller matrices. A Mueller matrix $\mathbf{M}$ transforms an incoming

Stokes vector $\vec{S}$ into an outgoing Stokes vector $\vec{S}'$ via

$$\vec{S}' = \mathbf{M}\vec{S} \tag{2.10}$$

$$\begin{bmatrix} s_0' \\ s_1' \\ s_2' \\ s_3' \end{bmatrix} = \begin{bmatrix} m_{11} & m_{12} & m_{13} & m_{14} \\ m_{21} & m_{22} & m_{23} & m_{24} \\ m_{31} & m_{32} & m_{33} & m_{34} \\ m_{41} & m_{42} & m_{43} & m_{44} \end{bmatrix} \begin{bmatrix} s_0 \\ s_1 \\ s_2 \\ s_3 \end{bmatrix}. \tag{2.11}$$

Looking at a system of optical components, the Mueller matrix for the system $\mathbf{M}_{\text{sys}}$ is found by multiplication of each component. For light propagating from component 1 to component N as illustrated in figure 2.3, the system Mueller matrix is found by

$$\mathbf{M}_{\text{sys}} = \mathbf{M}_N \mathbf{M}_{N-1} \cdots \mathbf{M}_1,$$

i.e. starting with the last component and working backwards to the first component.

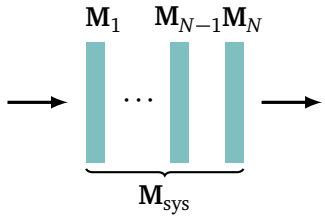

Figure 2.3: A cascade of Mueller-components.

A non-depolarising Mueller matrix $\mathbf{M}_J$ (i.e. the DOP of the incoming and outgoing Stokes vector is unchanged) can be constructed from a Jones matrix using the map[19]

$$\begin{aligned} \mathbb{A}_M : \mathbb{M}_{2\times 2}(\mathbb{C}) &\longrightarrow \mathbb{M}_{4\times 4}(\mathbb{R}) \\ \mathbf{J} &\longmapsto \mathbf{A}\left(\mathbf{J}\otimes\bar{\mathbf{J}}\right)\mathbf{A}^{-1}, \end{aligned} \tag{2.12}$$

where

$$\mathbf{A} = \begin{bmatrix} 1 & 0 & 0 & 1 \\ 1 & 0 & 0 & -1 \\ 0 & 1 & 1 & 0 \\ 0 & \mathrm{i} & -\mathrm{i} & 0 \end{bmatrix}. \tag{2.13}$$

$\otimes$ denotes the Kronecker product[20] of the Jones matrix $\mathbf{J}$ and its complex conjugate $\bar{\mathbf{J}}$. A Mueller matrix constructed in this fashion is sometimes called a *Mueller-Jones matrix*. Equation (2.12) can be written more plainly as

$$\mathbf{M}_J = \mathbf{A}\left(\mathbf{J}\otimes\bar{\mathbf{J}}\right)\mathbf{A}^{-1}. \tag{2.14}$$

2.5.1. Selected important Mueller matrices

The Mueller matrix for air (vacuum) is intuitively given as the identity matrix since it should not alter the Stokes vector,

$$\mathbf{M}_{\text{Air}} = \begin{bmatrix} 1 & 0 & 0 & 0 \\ 0 & 1 & 0 & 0 \\ 0 & 0 & 1 & 0 \\ 0 & 0 & 0 & 1 \end{bmatrix} = \mathbf{I}_{4\times 4}. \tag{2.15}$$

Rotation of a Mueller matrix around the coordinate system by an angle θ is given by[11]

$$\mathbf{R}(\theta) = \begin{bmatrix} 1 & 0 & 0 & 0 \\ 0 & \cos(2\theta) & \sin(2\theta) & 0 \\ 0 & -\sin(2\theta) & \cos(2\theta) & 0 \\ 0 & 0 & 0 & 1 \end{bmatrix}, \tag{2.16}$$

which is the same as the Mueller matrix for an optical rotator. A Mueller rotator can be used to rotate a Mueller matrix $\mathbf{M}$ by θ using

$$\mathbf{M}(\theta) = \mathbf{R}(-\theta)\mathbf{M}\mathbf{R}(\theta). \tag{2.17}$$

An ideal horizontal polariser is given by

$$\mathbf{M}_{0^\circ\text{-pol}} = \frac{1}{2}\begin{bmatrix} 1 & 1 & 0 & 0 \\ 1 & 1 & 0 & 0 \\ 0 & 0 & 0 & 0 \\ 0 & 0 & 0 & 0 \end{bmatrix}, \tag{2.18}$$

which can be rotated using (2.17) yielding

$$\mathbf{M}_{\theta\text{-pol}}(\theta) = \frac{1}{2}\begin{bmatrix} 1 & \cos(2\theta) & \sin(2\theta) & 0 \\ \cos(2\theta) & \cos^2(2\theta) & \sin(2\theta)\cos(2\theta) & 0 \\ \sin(2\theta) & \sin(2\theta)\cos(2\theta) & \sin^2(2\theta) & 0 \\ 0 & 0 & 0 & 0 \end{bmatrix}. \tag{2.19}$$

A system consisting of non-polarised light transmitted in the z-direction normal on a perfect polariser rotated 45° from the x-axis can then be described by

$$\mathbf{M}_{45^\circ\text{-pol}}(45^\circ)\vec{S} = \frac{1}{2}\begin{bmatrix} 1 & 0 & 1 & 0 \\ 0 & 0 & 0 & 0 \\ 1 & 0 & 1 & 0 \\ 0 & 0 & 0 & 0 \end{bmatrix}\begin{bmatrix} 1 \\ 0 \\ 0 \\ 0 \end{bmatrix} = \frac{1}{2}\begin{bmatrix} 1 \\ 0 \\ 1 \\ 0 \end{bmatrix} = \vec{S}', \tag{2.20}$$

where $\vec{S}'$ describes 45° linear polarised light with half the intensity of the incoming light.

The Mueller matrix for a perfect linear retarder with fast axis parallel to the x-axis and phase change $\delta = \delta_y - \delta_x$ is given by

$$\mathbf{M}_{\text{Ret}}(\delta) = \begin{bmatrix} 1 & 0 & 0 & 0 \\ 0 & 1 & 0 & 0 \\ 0 & 0 & \cos\delta & \sin\delta \\ 0 & 0 & -\sin\delta & \cos\delta \end{bmatrix}. \tag{2.21}$$

Sending 45° linear polarised light through a linear quarter wave plate ($\delta = \pi/2$) with fast axis at 0° can then be described as

$$\mathbf{M}_{\text{Ret}}\left(\frac{\pi}{2}\right)\vec{S} = \begin{bmatrix} 1 & 0 & 0 & 0 \\ 0 & 1 & 0 & 0 \\ 0 & 0 & 0 & 1 \\ 0 & 0 & -1 & 0 \end{bmatrix} \begin{bmatrix} 1 \\ 0 \\ 1 \\ 0 \end{bmatrix} = \begin{bmatrix} 1 \\ 0 \\ 0 \\ -1 \end{bmatrix} = \vec{S}', \tag{2.22}$$

where $\vec{S}'$ describes left circular polarised light as illustrated in figure 2.4.

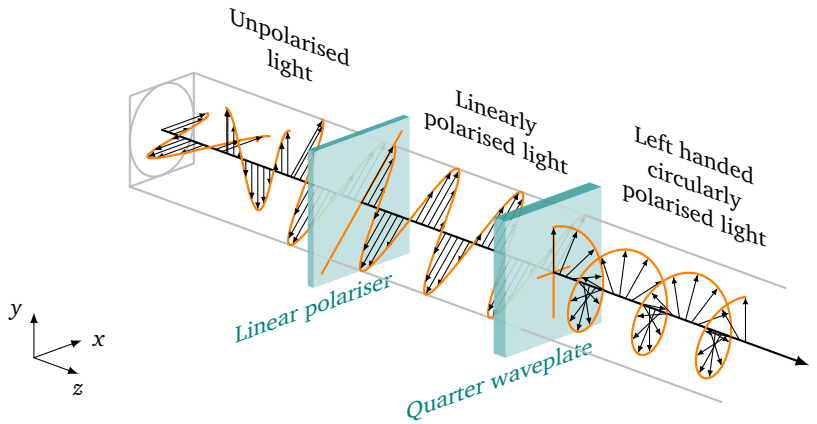

Figure 2.4: Light is polarised using a linear polariser (eq. (2.20)) before transmitting through a quarter waveplate which changes the polarisation to left circular (eq. (2.22)). The illustrated cascade of optical components thus creates a circular polariser. Image based on work by Mark Wibrow at tex.stackexchange.com/questions/113900/.

A non-depolarising sample where the eigenpolarisation states (the polarisation states that are transmitted unaltered by a polarisation element except for a change of amplitude and phase) of the retardation are aligned with the eigenpolarisation states of the diattenuation is referred to as a homogeneous diattenuating retarder[10] and can be described by the matrix

$$\mathbf{M}_{\text{Diat}}(\tau, \delta, \alpha) = \frac{\tau}{2} \begin{bmatrix} 1 & \cos(2\alpha) & 0 & 0 \\ \cos(2\alpha) & 1 & 0 & 0 \\ 0 & 0 & \sin(2\alpha)\cos(\delta) & \sin(2\alpha)\sin(\delta) \\ 0 & 0 & -\sin(2\alpha)\cos(\delta) & \sin(2\alpha)\cos(\delta) \end{bmatrix} \tag{2.23}$$

where τ is the transmission coefficient, δ the retardance, and α the diattenuation.

2.6. Physical realisable Mueller matrices

In order for a Mueller matrix to be physically realisable it must satisfy certain criteria. These criteria are[21]

- **Polarisation constraint** — The matrix must not over-polarise, i.e. the matrix may not produce a Stokes vector with a polarisation degree greater than unity.
- **Gain constraint** — In a passive system, the gain of a matrix must be less than unity, i.e. the matrix may not increase the intensity of an outgoing Stokes vector on par with the first law of thermodynamics.

As a result, not all real 4×4 matrices are Mueller matrices, i.e. the set of all Mueller matrices is a strict subset of $\mathbb{M}_{4\times4}(\mathbb{R})$. Even matrices which transfer one Stokes vector into another physical Stokes vector (i.e. a Stokes matrix) may not be a Mueller matrix.[22] Numerical verification for if a matrix is a physically realisable Mueller matrix is valuable in order to determine computational errors, noise and systematic errors.

Polarisation constraint

The polarisation constraint can be verified using the eigenvalues of the *Hermitian coherency matrix*,[23–25] defined as[26,27]

$$\mathbf{H} = \frac{1}{2}\sum_{i,j=1}^{4} m_{ij}\mathbf{\Omega}_{ij} \tag{2.24}$$

where $\{\mathbf{\Omega}_{ij}\}$ is the set of modified Dirac matrices spanning the special unitary group $SU(4)$,[28,29] with the exception of $\mathbf{\Omega}_{11}$ which is equal to the identity matrix. The modified Dirac matrices are listed in appendix B. m_{ij} denotes the elements of the Mueller matrix being tested. If the coherency matrix $\mathbf{H}$ is positive semi-definite, i.e. all its eigenvalues are non-negative, the matrix passes the polarisation constraint for being a physical realisable Mueller matrix. Measured Mueller matrices may contain errors, e.g. random noise, that contributes to the measurement not passing the polarisation constraint. Cloude therefore defined a measure of how close a matrix is to being a Mueller matrix given by a system fidelity[24]

$$H_{\text{fid.}} = -10\log_{10}\left(\left|\frac{\sum_i^{\lambda_i\geq 0}\lambda_i}{\sum_i^{\lambda_i<0}\lambda_i}\right|\right), \tag{2.25}$$

where λ_i are the eigenvalues of $\mathbf{H}$.

Gain constraint

In order to uphold conservation of energy, i.e. the energy of the transmitted or reflected Stokes vector does not increase, the gain constraint defined by[21,25]

$$g_f = m_{11} + \sqrt{m_{12}^2 + m_{13}^2 + m_{14}^2} \leq 1, \tag{2.26a}$$

for forward transmitted light, and

$$g_r = m_{11} + \sqrt{m_{21}^2 + m_{31}^2 + m_{41}^2} \leq 1, \tag{2.26b}$$

in the reverse transmittance case, must be fulfilled in a passive system.

2.6.1. Cloude filtration

A measured Mueller matrix $\mathbf{M}$ may contain measurement errors which invalidates it as a Mueller matrix, i.e. it is not physical. In order to rectify this, the measured matrix can be approximated/filtered to its nearest physical Mueller matrix. This is done by forming the Hermitian coherency matrix defined in equation (2.24) and unitarily diagonalising it, yielding[12,29,30]

$$\mathbf{H} = \mathbf{U}\mathbf{\Lambda}\mathbf{U}^*, \tag{2.27}$$

where $\cdot^* = (\overline{\cdot})^T$ denotes the complex-conjugate transpose. $\mathbf{\Lambda}$ is a diagonal matrix containing the eigenvalues of $\mathbf{H}$, with the corresponding eigenvectors held in $\mathbf{U}$ as columns. Any negative values in $\mathbf{\Lambda}$ are removed by setting them equal to zero. This filters $\mathbf{M}$ according to the polarisation constraint. Forming $\mathbf{\Lambda}'$ from the new eigenvalues, the filtered $\mathbf{H}'$ is then constructed as

$$\mathbf{H}' = \mathbf{U}\mathbf{\Lambda}'\mathbf{U}^*.$$

The filtered mueller matrix $\mathbf{M}'$ is then readily found by using equation (2.24) which is its own inverse,

$$\mathbf{M}' = \frac{1}{2}\sum_{i,j=1}^{4} h'_{ij}\mathbf{\Omega}_{ij} \tag{2.28}$$

where h'_{ij} are the elements of $\mathbf{H}'$.

2.7. Optics of anisotropic media

If the optical properties of a dielectric medium is direction dependent, the medium is said to be anisotropic. In a linear anisotropic dielectric medium (e.g. a quartz crystal), the components of the electric flux density $\vec{\mathfrak{D}}$ is a linear combination of the three components of the electric field $\vec{E}$. Mathematically this is expressed as[17]

$$\vec{\mathfrak{D}} = \begin{bmatrix} \epsilon_{11} & \epsilon_{12} & \epsilon_{13} \\ \epsilon_{21} & \epsilon_{22} & \epsilon_{23} \\ \epsilon_{31} & \epsilon_{32} & \epsilon_{33} \end{bmatrix} \begin{bmatrix} E_1 \\ E_2 \\ E_3 \end{bmatrix} = \boldsymbol{\epsilon}\vec{E}, \tag{2.29}$$

where $\boldsymbol{\epsilon}$ is a second rank tensor called the *electric permittivity tensor*. For most dielectric media (i.e. nonmagnetic materials with no optical activity) this tensor is symmetric ($\epsilon_{ij} = \epsilon_{ji}$), which warrants the need for only 6 independent coefficients in an arbitrary coordinate system. With certain symmetries, even fewer coefficients are needed to fully describe the media since some will vanish or be related to one another.

It is useful to define an *electric impermeability tensor*[17]

$$\boldsymbol{\eta} = \epsilon_0 \boldsymbol{\epsilon}^{-1}, \tag{2.30}$$

which is a symmetric second order tensor and can be represented geometrically by

$$\sum_{i,j=1}^{3} \eta_{ij} x_i x_j = 1 \tag{2.31}$$

where x_1, x_2, x_3 are the coordinates. This representation is known as the quadratic representation and is invariant to the choice of coordinate system.[17]

Since $\boldsymbol{\eta}$ is a 3×3 real symmetric matrix, it will have three mutually orthogonal unit-eigenvectors $\hat{e}_1$, $\hat{e}_2$ and $\hat{e}_3$ and three real eigenvalues ζ_1, ζ_2 and ζ_3. Therefore, in a coordinate system with axes $\hat{e}_1$, $\hat{e}_2$, and $\hat{e}_3$, called the principal coordinate system, the impermeability tensor $\boldsymbol{\eta}$ is represented by the diagonal matrix $\mathrm{diag}(\zeta_1, \zeta_2, \zeta_3)$.

In the principal coordinate system, equation (2.31) becomes more recognisable as an ellipsoid

$$\zeta_1 \hat{e}_1^2 + \zeta_2 \hat{e}_2^2 + \zeta_3 \hat{e}_3^2 = 1, \tag{2.32}$$

where $\hat{e}_1, \hat{e}_2, \hat{e}_3$ are the principal axes. The elements η_{ij} are related to the refractive index of the material ($n_{ij} = \sqrt{\epsilon_{ij}/\epsilon_0}$) as[31]

$$\eta_{ij} = \frac{\epsilon_0}{\epsilon_{ij}} = \frac{1}{n_{ij}^2}. \tag{2.33}$$

This relation naturally also holds in the principal coordinate system. With $\zeta_i = 1/n_i^2$, where n_1, n_2, n_3 are the principal refractive indices. Rewriting equation (2.32) as

$$\frac{\hat{e}_1^2}{n_1^2} + \frac{\hat{e}_2^2}{n_2^2} + \frac{\hat{e}_2^2}{n_2^2} = 1, \tag{2.34}$$

gives the index ellipsoid shown in figure 2.5.

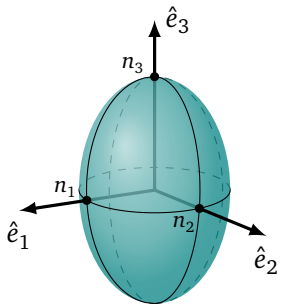

Figure 2.5: The index ellipsoid. The coordinates $\hat{e}_1$, $\hat{e}_2$ and $\hat{e}_3$ are the principal axes, while n_1, n_2 and n_3 are the principal refractive indices of the crystal.

2.7.1. Birefringent media

A medium in which all three principal refractive indices are different is called optical *biaxial*. If two of the principal refractive indices are equal, the medium is called optical *uniaxial*. In the latter case the axes are usually denoted as ordinary $n_o = n_1 = n_2$ and extraordinary $n_e = n_3$. If $n_e > n_o$, the medium is said to be positive uniaxial, conversely if $n_e < n_0$ the medium is called negative uniaxial.[17] Since birefringence is simply the retardance associated with propagation through an anisotropic medium,[10] the retardance δ for a optical uniaxial medium with thickness d at a given wavelength λ is[15]

$$\delta = \frac{2\pi d}{\lambda}(n_e - n_o) = \frac{2\pi d}{\lambda}\Delta n, \tag{2.35}$$

observed along one of the ordinary axes.

A crystal where all principal refractive indices are equal is called isotropic and will not display birefringence under normal conditions. An optical isotropic crystal (e.g. silicon) can however display birefringence if it is subjected to strain which will break the symmetry of the crystal.

2.7.2. Birefringence due to strain in crystal silicon

In photoelastic materials, such as silicon, differences in the refractive index can arise due to mechanical stress or strain.[32] Assuming a constant stress state along the axis of propagation, and that the principal axes of the impermeability and stress tensors coincide, the retardation caused by stress can be expressed as[33,34]

$$\delta = \frac{2\pi d}{\lambda}(n_1 - n_2) = \frac{2\pi d}{\lambda}C(\sigma_1 - \sigma_2) = \frac{2\pi d}{\lambda}C \cdot 2\tau_{\max}, \tag{2.36}$$

where C is the isotropic stress-optic coefficient of the material, and σ_1 and σ_2 are the first and second principal stresses in the plane perpendicular to the light propagation. $\tau_{\max}$ is the maximal shear stress. In general the stress-optic coefficient may be dependent on the direction of observation and principal stresses.

The anisotropic stress-optic coefficient can be derived from Pockel's phenomenological theory of photoelasticity,[31,35] which states that the difference between the deformed $\boldsymbol{\eta}$ and non-deformed $\boldsymbol{\eta}_0$ electric impermeability tensors is a linear function of the components of the stress as

$$\Delta\boldsymbol{\eta} = \boldsymbol{\eta} - \boldsymbol{\eta}_0 = \boldsymbol{\pi}\boldsymbol{\sigma}, \tag{2.37}$$

where $\boldsymbol{\pi}$ is a fourth-rank piezo-optical coefficient tensor expressible as a 6×6 matrix in a Cartesian coordinate system, and $\boldsymbol{\sigma}$ is the symmetric stress tensor

$$\boldsymbol{\sigma} = \begin{bmatrix} \sigma_x & \tau_{xy} & \tau_{xz} \\ \tau_{xy} & \sigma_y & \tau_{yz} \\ \tau_{xz} & \tau_{yz} & \sigma_z \end{bmatrix},$$

where $\sigma_x, \sigma_y, \sigma_z$ are the orthogonal normal stresses and $\tau_{xy}, \tau_{xz}, \tau_{yz}$ are the orthogonal shear stresses illustrated in figure 2.6.

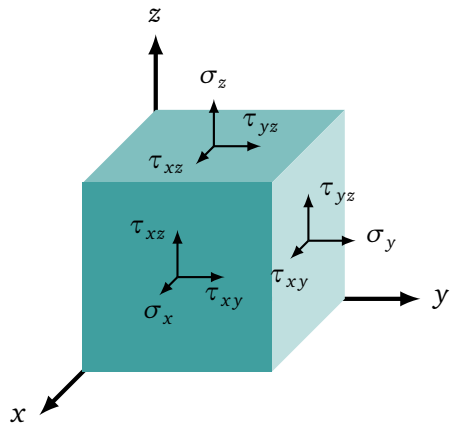

Figure 2.6: The symetric rank 2 stress tensor $\boldsymbol{\sigma}$. σ_x, σ_y and σ_z are the orthogonal normal stresses, and τ_{xy}, τ_{xz}, and τ_{yz} are the orthogonal shear stresses.

Due to the cubic symmetry of Si-crystals, there are only three independent components π_{11}, π_{12}, and π_{44} in the piezo-optical tensor.[36,37] In matrix form equation (2.37) becomes[38]

$$\begin{bmatrix} \Delta\eta_{11} \\ \Delta\eta_{22} \\ \Delta\eta_{33} \\ \Delta\eta_{23} \\ \Delta\eta_{13} \\ \Delta\eta_{12} \end{bmatrix} = \begin{bmatrix} \pi_{11} & \pi_{12} & \pi_{12} & 0 & 0 & 0 \\ \pi_{12} & \pi_{11} & \pi_{12} & 0 & 0 & 0 \\ \pi_{12} & \pi_{12} & \pi_{11} & 0 & 0 & 0 \\ 0 & 0 & 0 & \pi_{44} & 0 & 0 \\ 0 & 0 & 0 & 0 & \pi_{44} & 0 \\ 0 & 0 & 0 & 0 & 0 & \pi_{44} \end{bmatrix} \begin{bmatrix} \sigma_x \\ \sigma_y \\ \sigma_z \\ \tau_{yz} \\ \tau_{xz} \\ \tau_{xy} \end{bmatrix}. \tag{2.38}$$

For a silicon wafer sufficiently thin in the z-direction, the shear stresses τ_{xz}, τ_{yz}, and the normal stress σ_z vanishes, and the non-zero components σ_x, σ_y and τ_{xy} can be

approximated uniform through the sample thickness.[38] Under these conditions, the stress in a thin silicon wafer can therefore be considered as plane stress.

The orientation of the principal axes of the impermeability is determined by the isoclinic angle,[38] or fast axis angle θ as it is referred to in this thesis. The relation in equation (2.37) can be transformed to the principal axes of the impermeability (where $\Delta\zeta_i$ represents the eigenvalues of $\Delta\eta$, see section 2.7), yielding[38]

$$\begin{bmatrix} \Delta\zeta_1 \\ \Delta\zeta_2 \\ \Delta\zeta_3 \\ 0 \\ 0 \\ 0 \end{bmatrix} = \begin{bmatrix} \pi'_{11} & \pi'_{12} & \pi_{12} & 0 & 0 & \pi'_{16} \\ \pi'_{12} & \pi'_{11} & \pi_{12} & 0 & 0 & -\pi'_{16} \\ \pi_{12} & \pi_{12} & \pi_{11} & 0 & 0 & 0 \\ 0 & 0 & 0 & \pi_{44} & 0 & 0 \\ 0 & 0 & 0 & 0 & \pi_{44} & 0 \\ \frac{\pi'_{16}}{2} & \frac{-\pi'_{16}}{2} & 0 & 0 & 0 & \pi'_{66} \end{bmatrix} \begin{bmatrix} \sigma'_x \\ \sigma'_y \\ 0 \\ 0 \\ 0 \\ \tau'_{xy} \end{bmatrix}, \tag{2.39}$$

where σ'_x, σ'_y and τ'_{xy} are the stress components in the principal axes of the impermeability tensor.[38] Generally, the piezo-optical coefficients π'_{ij} in these principal axes are functions of θ, which depend on the crystal plane that is observed, and along which direction. Hence, the stress-optic coefficient C will generally depend on these parameters. For completeness, the derivation of the stress-optic coefficient pertaining to selected planes can be found in appendix C. A simpler model will however be used in this thesis, as it is found adequate for proof-of-concept.

In the simpler model, the stress-optic coefficient is estimated by assuming that the principal axes of both stress and impermeability coincide, i.e. that the material is mechanical isotropic. Hence, the normal stresses are equal to the principal stresses, and the shear stress vanishes, i.e $\sigma'_x = \sigma_1$, $\sigma'_y = \sigma_2$ and $\tau'_{xy} = 0$. Looking at equation (2.39), the following relations

$$\Delta\zeta_1 = \pi'_{11}\sigma_1 + \pi'_{12}\sigma_2, \tag{2.40}$$

$$\Delta\zeta_2 = \pi'_{12}\sigma_1 + \pi'_{11}\sigma_2, \tag{2.41}$$

hold true under this assumption. Subtracting these equations yield

$$\Delta\zeta_1 - \Delta\zeta_2 = (\sigma_1 - \sigma_2)(\pi'_{11} - \pi'_{12}) = 2\tau_{\max}(\pi_{11} - \pi_{12}), \tag{2.42}$$

using the fact that $2\tau_{\max} = \sigma_1 - \sigma_2$ from Mohr's circle (fig. 2.7), and the approximation $\pi'_{11} - \pi'_{12} \simeq \pi_{11} - \pi_{12}$ (cf. appendix C).

Looking back at the definition of ζ_i, the difference $\Delta\zeta_1 - \Delta\zeta_2$ can also be expressed as

$$\begin{aligned} \Delta\zeta_1 - \Delta\zeta_2 &= \left(\frac{1}{n_1^2} - \frac{1}{n_0^2}\right) - \left(\frac{1}{n_2^2} - \frac{1}{n_0^2}\right) = \frac{1}{n_1^2} - \frac{1}{n_2^2} \\ &= \frac{n_2^2 - n_1^2}{n_1^2 n_2^2} = \frac{-(n_1 - n_2)(n_1 + n_2)}{n_1^2 n_2^2} \\ &\simeq \frac{-(n_1 - n_2)\cdot 2n_0}{n_0^4} \\ &\simeq -2\Delta n / n_0^3, \end{aligned} \tag{2.43}$$

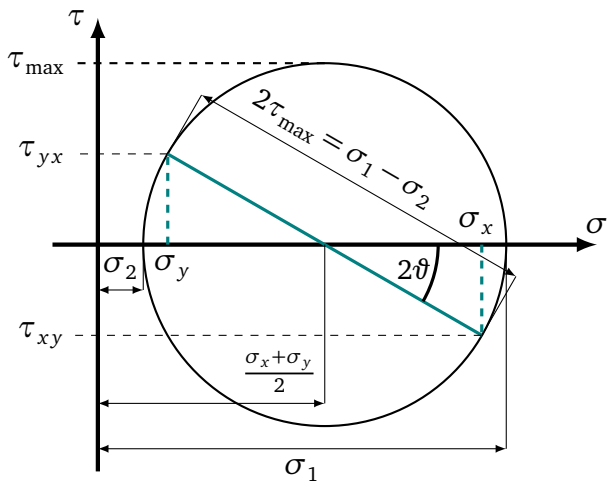

Figure 2.7: Mohr's circle in the plane. The orientation of the principal axes is denoted by ϑ, σ_1 and σ_2 is the principal stresses, while $\tau_{\max}$ is the corresponding maximum shear stress.

where n_0 is the non-perturbed refractive index of the medium, and n_1 and n_2 represents the refractive indices of the stressed medium in the principal directions. The changes in the refractive index due to strain is assumed small, such that the approximation $n_i \approx n_0, i = 1,2$ hold. Using this approximation with equation (2.42) gives the relation

$$\tau_{\max} \simeq -\frac{\Delta n}{n_0^3(\pi_{11} - \pi_{12})}. \tag{2.44}$$

Substituting Δn with equation (2.35) yields

$$\tau_{\max} \simeq \frac{\lambda}{2\pi d n_0^3(\pi_{11} - \pi_{12})} \cdot \delta, \tag{2.45}$$

indicating that the isotropic stress-optic coefficient of the material can be expressed as

$$C = \frac{n_0^3}{2}(\pi_{11} - \pi_{12}).$$

Equation (2.45) can thus be rewritten as a proportional relationship between the maximum shear-stress and the retardance as

$$\tau_{\max} \simeq \mathscr{H} \cdot \delta, \tag{2.46}$$

where the proportionality coefficient

$$\mathscr{H} = \frac{\lambda}{4\pi d C} = \frac{\lambda}{2\pi d n_0^3(\pi_{11} - \pi_{12})}, \tag{2.47}$$

is dependent on the wavelength λ, thickness d, refractive index n_0, and piezo-optical coefficients of the material π_{ij}.

A third approach is to take the average stress-optic coefficient for all crystal orientations. This method is reported to decrease the accuracy of the measurements by about 35 %.[39] The simpler coefficient presented here is assumed to be worse, but is chosen adequate for a proof-of-concept.

He et al. has reported the difference $\pi_{11} - \pi_{12}$ to be $9.88 \times 10^{-13}\,\mathrm{Pa}^{-1}$, and $\pi_{44} = 6.50 \times 10^{-13}\,\mathrm{Pa}^{-1}$ for crystalline silicon.[38] Similar, but different values for these coefficients have been reported in literature by Giardini[40] and Iwaki et al.[41] The values obtained by He et al. will however be used in this thesis as these are the most recent results and also lie in between the other reported values. The reported values are summarised in table 2.1.

Table 2.1: Reported piezo-optical coefficients for crystal silicon.

	$\pi_{11} - \pi_{12}$	π_{44}
He et al.[38]	$9.88 \times 10^{-13}\,\mathrm{Pa}^{-1}$	$6.50 \times 10^{-13}\,\mathrm{Pa}^{-1}$
Iwaki et al.[41]	$8.48 \times 10^{-13}\,\mathrm{Pa}^{-1}$	$4.58 \times 10^{-13}\,\mathrm{Pa}^{-1}$
Giardini[40]	$14.4 \times 10^{-13}\,\mathrm{Pa}^{-1}$	$10.0 \times 10^{-13}\,\mathrm{Pa}^{-1}$

2.7.3. In-plane stress direction.

A relaxed optical isotropic crystal will have uniform optical density. The relaxed 2-D unit cell is illustrated in figure 2.8 where each atom is equidistant from its closest neighbour. In this relaxed state there is no clearly defined slow or fast axis as the refractive index is the same in all directions.

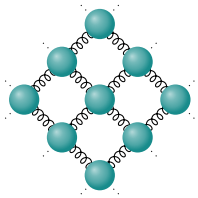

Figure 2.8: A relaxed 2-D lattice, the density is uniform throughout the crystal.

If the crystal experiences either horizontal tensile stress or vertical compressive stress, the unit cell will deform as shown in figure 2.9 according to this model. This will result in increased vertical density and decreased horizontal density, giving a clearly defined slow axis along the vertical direction. Given only a slow or fast axis direction, it will therefore be ambiguous pertaining to if the crystal experiences compression parallel to the slow axis, or tension perpendicular to the slow axis, or possible a superposition of the two.

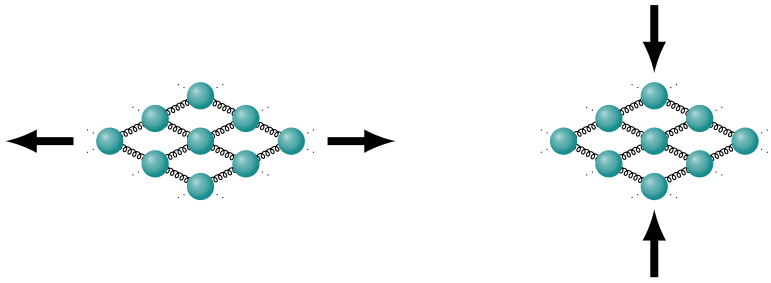

Figure 2.9: A 2-D crystal experiencing horizontal tensile stress (left) and vertical compressive stress (right). Notice that both cases deform the crystal lattice in the same manner.

2.8. Polarimeter design

A general Mueller matrix polarimeter consists of four main parts, a light source, a polarisation state generator (PSG), a polarisation state Analyser (PSA), and a detector, not including the sample being measured. The principle behind polarimetry is probing a sample with a set of appropriate polarisation sates generated by the PSG, and then analysing the polarisation changes from the sample with the PSA.

At least four intensity measurements are required to determine a single Stokes vector.[42] In order to get the full 4×4 Mueller matrix, a minimum of four probing states are needed for each Stokes vector measurement.[10] Two main approaches exists for this purpose, one where the polarisation state is continuously modulated and analysed, and the other where discrete states are generated and analysed. Many technical solutions exists for the purpose of generating and analysing polarisation sates, e.g. systems based on photo-elastic modulators,[43] electro-optical modulators,[44,45] Pockel's cells,[46,47] liquid crystals,[48–53] and rotating prism retarders or waveplates.[54–56]

Continuous modulation can operate very fast, but requires complicated modulation techniques. Since this thesis mainly focuses on discrete modulation techniques using liquid crystals, continuous modulation will not be further explored. To uniquely determine the Mueller matrix using a discrete polarimeter, the polarisation states of the PSG and PSA must span the polarisation space, i.e. the Poincaré sphere presented in section 2.4. It has been shown by Sabatke et al.[57] that the four optimal Stokes vectors for the PSG and PSA make up a regular tetrahedron when plotted on the Poincaré sphere.

2.9. Genetic algorithms

Inspired by the principle of natural selection, genetic algorithms[58] excel in finding near-optimal configurations efficiently in complicated systems.[59] In order to employ a genetic algorithm, the system variables that are to be optimised must be translated into *genes* as illustrated in figure 2.10. A common way of doing this is to represent each variable by a binary string, i.e. a row of zeroes and ones. The genes are then concatenated into a single *genome* for a system configuration.

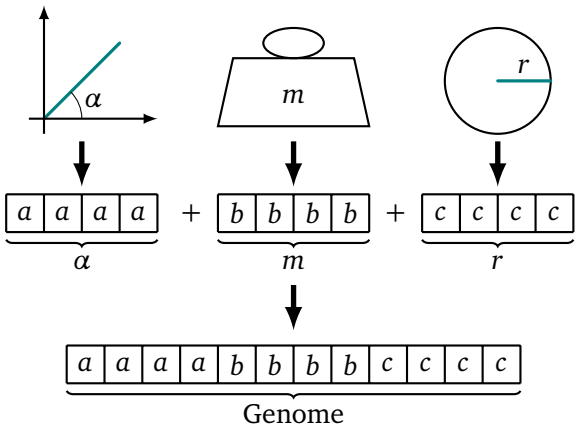

Figure 2.10: The system variables are transcribed into genes which are then linked to form a system genome.

In order to evaluate if a given genome is favourable, a *goodness-of-fit* test is needed. Analogous to nature, this evaluation can be how good a species is able to find food, or run from predators. An unfit *phenotype* (the expressed genome) will be unable to pass on its genetic material since it is either dead from starvation, or eaten. Similar, a genome having a poor goodness-of-fit have a higher possibility to be removed from the *gene-pool*.

The starting genes of the genetic algorithm can either be predetermined or randomly seeded. This initial population is then tested using the goodness-of-fit function through what is known as a *tournament*.[59,60] The tournament rules arbitrate the selection, determining which genomes are allowed to pass on their genes. Survivors of the tournament are then cloned (asexual reproduction) or mated (genetic crossover), creating children for the next iteration of the algorithm. During either cloning or mating, mutation may occur, which is simulated using either random or controlled bit-flipping.[60] This process is illustrated in figure 2.11.

The genetic algorithm can run indefinitely, or until certain criteria are met, e.g. *generation* count or a satisfactory goodness-of-fit value. Having run the algorithm, the genome is expressed as its phenotype, revealing the system variables giving a favourable configuration.

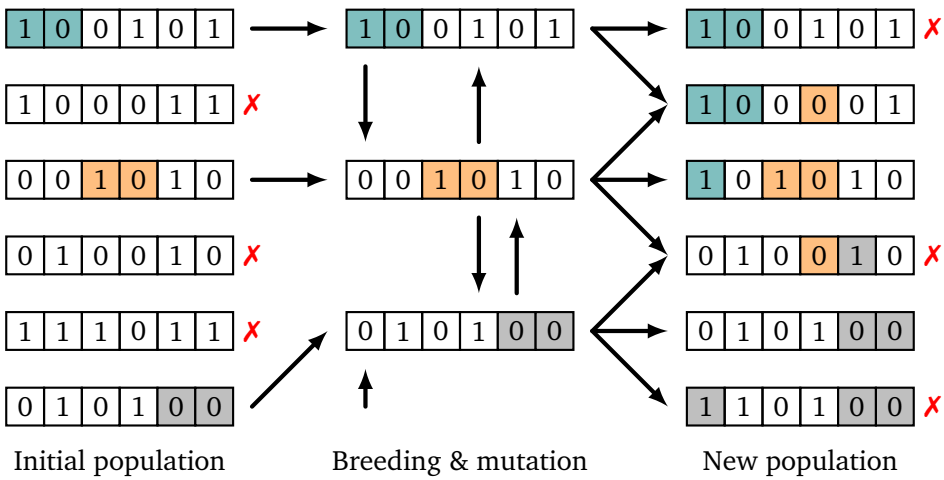

Figure 2.11: Tournament survivors are chosen from the population, these then breed, mutate or copy themselves to create the next population. The new generation is then re-evaluated, and the tournament survivors repeat the cycle until the end condition is met.

Chapter 3

Ellipsometry

One of the simplest ellipsometers, sketched in figure 3.1, is a configuration where the complex reflectance ratio ρ, of p-polarised and s-polarised light is measured. p-polarised light is parallel to the plane of incidence, while s-polarised light (from the German word *senkrecht*) is perpendicular to the plane of incidence. The complex reflectance ratio may be parametrised by the amplitude component Ψ and the phase difference Δ as

$$\rho = \frac{r_p}{r_s} = \left|\frac{r_p}{r_s}\right| \cdot \arg\left(\frac{r_p}{r_s}\right) = \tan(\Psi) \cdot e^{i\Delta}, \tag{3.1}$$

where r_i is the reflected i-polarised light.

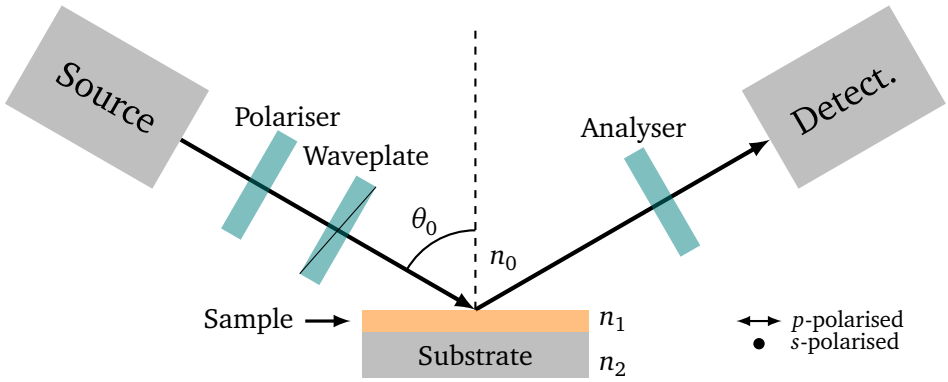

Figure 3.1: Sketch of a simple ellipsometer.

The optical constants of the sample can be found indirectly from the measurement of Ψ and Δ. This is done by constructing a model of the reflection using Snell's law

$$n_l \sin(\theta_l) = n_m \sin(\theta_m), \tag{3.2}$$

and the Fresnel equations,[15,17] which from isotropic medium l to isotropic medium

$m = l + 1$ are

$$r_{lm,s} = \frac{n_l \cos(\theta_l) - n_m \cos(\theta_m)}{n_l \cos(\theta_l) - n_m \cos(\theta_m)}, \qquad t_{lm,s} = \frac{2n_l \cos(\theta_l)}{n_l \cos(\theta_l) + n_m \cos(\theta_m)}, \tag{3.3}$$

and

$$r_{lm,p} = \frac{n_m \cos(\theta_l) - n_l \cos(\theta_m)}{n_m \cos(\theta_l) - n_l \cos(\theta_m)}, \qquad t_{lm,p} = \frac{2n_l \cos(\theta_l)}{n_l \cos(\theta_m) + n_m \cos(\theta_l)}. \tag{3.4}$$

n_i is the refractive index of medium i, θ_l is the incident angle, while θ_m is the angle of the transmitted light. $t_{lm,i}$ is the transmitted light, while $r_{lm,i}$ is the reflected light. The constructed model is then fitted to the measurements in order to infer e.g. the refractive index of the sample, or the sample thickness.

For a layered stack of isotropic films, the Abeles transfer matrix formalism, or the scattering formalism can be used to calculate the reflection coeficients r_p and r_s for the sandwiched system.[61] Recursive Airy type formulas are also commonly used to find the reflection coefficients.[61,62]

For anisotropic samples, the relations are more complex. In general, ellipsometry is the experimental technique of measuring the polarisation changing properties of a sample, either using light reflected from the sample, or light transmitted through it as illustrated in figure 3.2. There exist different types of ellipsometers varying in complexity, depending on what is to be measured or imaged. A more general approach to ellipsometry is the Mueller-Stokes formalism, which is the main topic of this thesis.

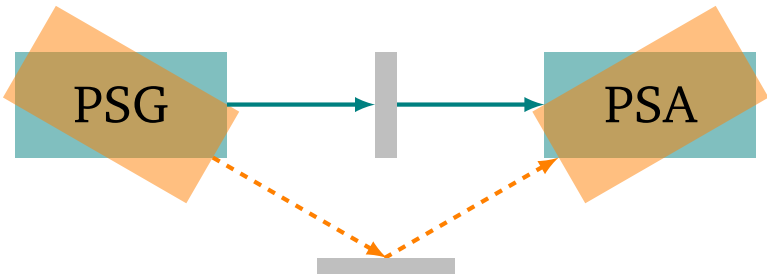

Figure 3.2: General ellipsometry design where polarised light is sent out through a polarisation state generator (PSG) and received in a polarisation state analyser (PSA) after either being transmitted through a sample (solid line), or reflected from the surface of a sample (dashed line).

3.1. Mueller matrix ellipsometry

The general idea behind a Mueller matrix ellipsometer is to generate different polarisation states, and measure the resulting state after the light has either reflected of a surface, or transmitted through a sample. This is achieved by inserting a polarisation

state generator (PSG) between the light source and sample, and a polarisation state analyser (PSA) between the sample and detector.

A state i of the PSA is represented by the Mueller matrix

$$\mathbf{M}_{Ai} = \begin{bmatrix} a^i_{11} & a^i_{12} & a^i_{13} & a^i_{14} \\ a^i_{21} & a^i_{22} & a^i_{23} & a^i_{24} \\ a^i_{31} & a^i_{32} & a^i_{33} & a^i_{34} \\ a^i_{41} & a^i_{42} & a^i_{43} & a^i_{44} \end{bmatrix}, \tag{3.5}$$

which will transform an incoming Stokes vector $\vec{S}$ according to equation (2.11). Assuming an optical detector that is only able to detect the intensity of the incoming light, i.e. the s'_0 element of the Stokes vector $\vec{S}'$ (cf. equation (2.7)), only the first row of $\mathbf{M}_{Ai}$ will influence the measurement, since

$$s'_0 = a^i_{11}s_0 + a^i_{12}s_1 + a^i_{13}s_2 + a^i_{14}s_3.$$

A different state of the PSA will result in a different measured intensity. By having at least four well chosen states of the PSA it is possible to reconstruct the incoming Stokes vector from the outgoing intensity. By defining the *analyser vector* corresponding to state i of the PSA as

$$\vec{A}_i = \begin{bmatrix} a^i_{11} & a^i_{12} & a^i_{13} & a^i_{14}, \end{bmatrix}, \tag{3.6}$$

an *analyser matrix* $\mathbf{A}$ can be constructed containing the analyser vectors as rows

$$\mathbf{A} = \begin{bmatrix} \vec{A}_1 \\ \hline \vec{A}_2 \\ \hline \vdots \\ \hline \vec{A}_n \end{bmatrix}. \tag{3.7}$$

Similar to the PSA, the PSG can be characterised by a *modulation matrix* $\mathbf{W}$ with columns equal to the Stokes vectors the PSG can generate.

$$\mathbf{W} = \begin{bmatrix} \vec{W}_1 & \vec{W}_2 & \cdots & \vec{W}_m \end{bmatrix}. \tag{3.8}$$

The PSG must produce a minimum of 4 sufficiently dissimilar (orthogonal) states in order be able to characterise the sample Mueller matrix.

The matrix $\mathbf{B}$ defined as[63]

$$\mathbf{B} = \mathbf{AMW}, \tag{3.9}$$

can be constructed by performing a minimum of 16 intensity measurements (measuring at least 4 Stokes vectors, each requiring at least 4 intensity measurements (cf. section 2.8). $\mathbf{B}$ can then be used to determine the Mueller matrix of the sample $\mathbf{M}$, if the $\mathbf{W}$ and $\mathbf{A}$ matrices are know. If the number of analyser rows n and modulation columns

m both equal the minimum of 4 this is done by simply multiplying with the inverse of $\mathbf{W}$ and $\mathbf{A}$ on both sides

$$\mathbf{M} = \mathbf{A}^{-1}\mathbf{B}\mathbf{W}^{-1}. \tag{3.10}$$

By introducing the Moore-Penrose pseudo-inverse,[64] denoted with a dagger $\cdot^{\dagger}$, the more general case where $m, n \geq 4$ can be solved as

$$\mathbf{M} = \mathbf{A}^{\dagger}\mathbf{B}\mathbf{W}^{\dagger}. \tag{3.11}$$

3.2. Calibration of a Mueller matrix ellipsometer

The $\mathbf{W}$ and $\mathbf{A}$ matrices can be analytically determined by modelling the system components. This can call for complex models taking into account dispersion and misalignment, among other effects. Another alternative called the *Eigenvalue Calibration Method* (ECM), developed by Compain et al.[63] for Mueller matrix ellipsometers, can also be used to determine the system matrices $\mathbf{W}$ and $\mathbf{A}$. With the ECM, $\mathbf{W}$ and $\mathbf{A}$ are determined with matrix algebra from measurements of known reference samples.

3.2.1. Eigenvalue calibration method

In the following section, boldface capital-letters (e.g. $\mathbf{M}$) refer to theoretical matrices, whereas boldface lower-case letters (e.g. $\mathbf{b}$) correspond to real experimental measurements. Only the case where the number of analyser n and modulation vectors m are equal will be discussed here.

From the set of calibration samples $\{\mathbf{m}\}$, there is a corresponding set $\{\mathbf{b}\}$ of intensity matrices given by equation (3.9)

$$\mathbf{b}_i = \mathbf{a}\mathbf{m}_i\mathbf{w}, \tag{3.12}$$

representing the measurement of calibration sample i with Mueller matrix $\mathbf{m}_i$. Note that $\mathbf{b}_0 \equiv \mathbf{a}\mathbf{w}$ is the measurement of air since the Mueller matrix of air is equal to the identity matrix $\mathbf{I}_{4\times4}$. The elements of the sets $\{\mathbf{c}^W\}$ and $\{\mathbf{c}^A\}$ are constructed as[63]

$$\mathbf{c}_i^W = \mathbf{b}_0^{\dagger}\mathbf{b}_i = (\mathbf{a}\mathbf{w})^{\dagger}(\mathbf{a}\mathbf{m}_i\mathbf{w}) = \mathbf{w}^{\dagger}\mathbf{m}_i\mathbf{w} \tag{3.13}$$

and

$$\mathbf{c}_i^A = \mathbf{b}_i\mathbf{b}_0^{\dagger} = (\mathbf{a}\mathbf{m}_i\mathbf{w})(\mathbf{a}\mathbf{w})^{\dagger} = \mathbf{a}\mathbf{m}_i\mathbf{a}^{\dagger}. \tag{3.14}$$

Note that $\mathbf{c}_i^W$ is independent of $\mathbf{a}$ and that $\mathbf{c}_i^A$ is independent of $\mathbf{w}$. In the special case where $n = 4$, $\mathbf{c}_i^W$, $\mathbf{c}_i^A$, and $\mathbf{m}_i$ are similar matrices with the same eigenvalues, apart from random measurement noise.

A sample with only retardation and diattenuation takes the form of that of equation (2.23), which has two real and two complex eigenvalues independent of the angle of rotation θ,

$$\lambda_{\mathfrak{R}_1} = 2\tau\cos^2(\alpha), \qquad \lambda_{\mathfrak{R}_2} = 2\tau\sin^2(\alpha), \tag{3.15}$$

$$\lambda_{\mathfrak{C}_1} = \tau\sin(2\alpha)e^{-\mathrm{i}\delta} \qquad \lambda_{\mathfrak{C}_2} = \tau\sin(2\alpha)e^{+\mathrm{i}\delta}. \tag{3.16}$$

By associating the eigenvalues of $\mathbf{c}_i^W$ or $\mathbf{c}_i^A$ with the theoretical eigenvalues of $\mathbf{m}_i$, it is possible to reconstruct the Mueller matrix of each calibration sample as

$$\tau_{\text{pol}} = \text{Tr}(\mathbf{c}_{\text{pol}}), \qquad \tau_{\text{ret}} = \frac{1}{2}(\lambda_{\mathfrak{R}_1} + \lambda_{\mathfrak{R}_2}), \tag{3.17}$$

$$\delta = \frac{1}{2}\arg\left(\frac{\lambda_{\mathfrak{C}_1}}{\lambda_{\mathfrak{C}_2}}\right), \qquad \alpha = \arctan\sqrt{\frac{\lambda_{\mathfrak{R}_1}}{\lambda_{\mathfrak{R}_2}}}. \tag{3.18}$$

This property also enables the direct measurement of Mueller matrices with known form, without the need of a calibration, as the physical properties can be found directly from either $\mathbf{c}^W$ or $\mathbf{c}^A$. However, this does not uniquely define the sample as there is an indetermination in the sign of δ, and the phase of α. Permuting $\lambda_{\mathfrak{C}_1}$ and $\lambda_{\mathfrak{C}_2}$ changes the sign of δ, and permuting the real eigenvalues $\lambda_{\mathfrak{R}_1}$ and $\lambda_{\mathfrak{R}_2}$ changes α to $\pi/2-\alpha$. Some prior knowledge is therefore required to get rid of the indetermination by comparing the obtained values with the theoretical ones.

In the case where $n > 4$, the 4 eigenvalues of the $\mathbf{c}_i$-matrix that gives the closest approximation to the expected $\mathbf{M}_i$ should be used.[53,65] In practice this might be difficult, and a suggested solution is to calculate the 4×4 matrices $\mathbf{c}_i'^W$ and $\mathbf{c}_i'^A$ from the 4×4 subsets of $\mathbf{b}_0$ and $\mathbf{b}_i$ which give the lowest condition number in $\mathbf{b}_0$.[53] The eigenvalues from $\mathbf{c}_i'^W$ and $\mathbf{c}_i'^A$ can then be used to reconstruct $\mathbf{m}_i$ less ambiguously. The full $\mathbf{c}_i^W$ and $\mathbf{c}_i^A$ matrices will be used for the rest of the calculations.

The linear maps from the space of real-valued matrices into itself are defined as[63]

$$\begin{aligned} \mathbb{H}_{M_i}^W : \mathbb{M}_{4\times n}(\mathbb{R}) &\longrightarrow \mathbb{M}_{4\times n}(\mathbb{R}) \\ \mathbf{X} &\longmapsto \mathbf{M}_i\mathbf{X} - \mathbf{X}\mathbf{c}_i^W, \end{aligned} \tag{3.19}$$

and

$$\begin{aligned} \mathbb{H}_{M_i}^A : \mathbb{M}_{n\times 4}(\mathbb{R}) &\longrightarrow \mathbb{M}_{n\times 4}(\mathbb{R}) \\ \mathbf{X} &\longmapsto \mathbf{X}\mathbf{M}_i - \mathbf{c}_i^A\mathbf{X}, \end{aligned} \tag{3.20}$$

have the properties of containing $\mathbf{W}$ and $\mathbf{A}$ within their respective null space, i.e.

$$\mathbb{H}_{M_i}^W(\mathbf{W}) = \mathbb{H}_{M_i}^A(\mathbf{A}) = 0,$$

if there are no experimental errors or noise.

The $\mathbb{H}_{M_i}^W$ and $\mathbb{H}_{M_i}^A$ maps can be written as $4n \times 4n$ coordinate transfer matrices by expressing the $\mathbf{X}$ matrices as $4n \times 1$ column vectors $[\mathbf{X}]_{U^W}^W$ and $[\mathbf{X}]_{U^A}^A$ in their respective standard basis. The standard basis for $\mathbb{M}_{4\times n}(\mathbb{R})$ is[12,30]

$$\{\mathbf{U}^W\} = \left\{ \mathbf{U}_1^W = \begin{bmatrix} 1 & 0 & \cdots & 0 \\ 0 & 0 & \cdots & 0 \\ 0 & 0 & \cdots & 0 \\ 0 & 0 & \cdots & 0 \end{bmatrix}, \mathbf{U}_2^W = \begin{bmatrix} 0 & 1 & \cdots & 0 \\ 0 & 0 & \cdots & 0 \\ 0 & 0 & \cdots & 0 \\ 0 & 0 & \cdots & 0 \end{bmatrix}, \cdots, \mathbf{U}_{4n}^W = \begin{bmatrix} 0 & 0 & \cdots & 0 \\ 0 & 0 & \cdots & 0 \\ 0 & 0 & \cdots & 0 \\ 0 & 0 & \cdots & 1 \end{bmatrix} \right\}, \tag{3.21}$$

while for $\mathbb{M}_{n\times 4}(\mathbb{R})$ it is

$$\{\mathbf{U}^A\} = \left\{ \mathbf{U}_1^A = \begin{bmatrix} 1 & 0 & 0 & 0 \\ 0 & 0 & 0 & 0 \\ \vdots & \vdots & \vdots & \vdots \\ 0 & 0 & 0 & 0 \end{bmatrix}, \mathbf{U}_2^A = \begin{bmatrix} 0 & 1 & 0 & 0 \\ 0 & 0 & 0 & 0 \\ \vdots & \vdots & \vdots & \vdots \\ 0 & 0 & 0 & 0 \end{bmatrix}, \cdots, \mathbf{U}_{4n}^A = \begin{bmatrix} 0 & 0 & 0 & 0 \\ 0 & 0 & 0 & 0 \\ \vdots & \vdots & \vdots & \vdots \\ 0 & 0 & 0 & 1 \end{bmatrix} \right\}. \tag{3.22}$$

Note that in principle, any basis that spans $\mathbb{M}_{4\times n}(\mathbb{R})$ or $\mathbb{M}_{n\times 4}(\mathbb{R})$ respectively may be used.

$\mathbb{H}_{M_i}^W$ can now be written as

$$\mathbf{H}_{M_i}^W = \left[[\mathbf{M}_i\mathbf{U}_1^W - \mathbf{U}_1^W\mathbf{c}_i^W]_{U^W} \middle| [\mathbf{M}_i\mathbf{U}_2^W - \mathbf{U}_2^W\mathbf{c}_i^W]_{U^W} \middle| \cdots \middle| [\mathbf{M}_i\mathbf{U}_{4n}^W - \mathbf{U}_{4n}^W\mathbf{c}_i^W]_{U^W} \right], \tag{3.23}$$

and $\mathbb{H}_{M_i}^A$ as

$$\mathbf{H}_{M_i}^A = \left[[\mathbf{U}_1^A\mathbf{M}_i - \mathbf{c}_i^A\mathbf{U}_1^A]_{U^A} \middle| [\mathbf{U}_2^A\mathbf{M}_i - \mathbf{c}_i^A\mathbf{U}_2^A]_{U^A} \middle| \cdots \middle| [\mathbf{U}_{4n}^A\mathbf{M}_i - \mathbf{c}_i^A\mathbf{U}_{4n}^A]_{U^A} \right]. \tag{3.24}$$

The full $\mathbf{H}_{M_i}^W$ and $\mathbf{H}_{M_i}^A$ for the $n = 4$ case can be found in appendix D. $\mathbf{W}$ and $\mathbf{A}$ may now be found by solving the overdetermined systems

$$\mathbf{H}_{M_i}^W[\mathbf{X}]_{U^W} = 0, \qquad \mathbf{M_i} \in \{\mathbf{M}_1, \ldots, \mathbf{M}_n\} \tag{3.25}$$

$$\mathbf{H}_{M_i}^A[\mathbf{X}]_{U^A} = 0, \qquad \mathbf{M_i} \in \{\mathbf{M}_1, \ldots, \mathbf{M}_n\} \tag{3.26}$$

for an appropriate set of reference samples $\{\mathbf{M}\} = \{\mathbf{M}_1, \ldots, \mathbf{M}_n\}$. This is done by a least-squares method by introducing the matrices

$$\mathbf{K}^W = \sum_{i=1}^{n} (\mathbf{H}_{M_i}^W)^T \mathbf{H}_{M_i}^W, \tag{3.27}$$

$$\mathbf{K}^A = \sum_{i=1}^{n} (\mathbf{H}_{M_i}^A)^T \mathbf{H}_{M_i}^A, \tag{3.28}$$

which are positive semi-definite symmetric real matrices, meaning they have only non-negative eigenvalues and can be diagonalized. Furthermore, they will in theory have 15 non-zero and 1 zero eigenvalue since

$$\mathbf{K}^W[\mathbf{X}]_{U^W} = 0, \tag{3.29}$$

$$\mathbf{K}^A[\mathbf{X}]_{U^A} = 0, \tag{3.30}$$

have unique solutions $\mathbf{W}$ and $\mathbf{A}$ respectively. With real measurements, the equalities $\mathbb{H}^W_{M_i}(\mathbf{w}) = 0$ and $\mathbb{H}^W_{M_i}(\mathbf{a}) = 0$ can not be exactly verified due to random noise. A good approximation can be found by sorting all the eigenvalues

$$\lambda^w_1 > \lambda^w_2 > \ldots > \lambda^w_{4n} \gtrsim 0, \tag{3.31}$$
$$\lambda^a_1 > \lambda^a_2 > \ldots > \lambda^a_{4n} \gtrsim 0, \tag{3.32}$$

and take the eigenvector corresponding to λ^w_{4n} and λ^a_{4n} which gives the best solutions for equation (3.29) and (3.30), being $[\mathbf{w}]_{U^W}$ and $[\mathbf{a}]_{U^A}$ respectively. Evaluating the coordinate vectors $[\mathbf{w}]_{U^W}$ and $[\mathbf{a}]_{U^A}$ will result in the sought for $\mathbf{W}$ and $\mathbf{A}$ matrices apart from a multiplicative real factor. As the matrices are normalised, this factor does not matter.

Since rotation, defined in equation (2.17), produces a similar matrix, the rotation of the calibration samples can not be found by their matrix eigenvalues. Therefore, if the rotation of the calibration samples are not perfectly known beforehand, a θ-dependency can be established for all unknown calibration samples by

$$\mathbf{M}'_i(\theta_i) = \mathbf{R}(-\theta_i)\mathbf{M}_i\mathbf{R}(\theta_i) \tag{3.33}$$

inducing a $(\theta_1, \ldots, \theta_k)$ dependency in $\mathbf{K}^W = \mathbf{K}^W(\theta_1, \ldots, \theta_k)$ and $\mathbf{K}^A = \mathbf{K}^A(\theta_1, \ldots, \theta_k)$. The angles can then be deduced by minimising the ratio of the smallest eigenvalue λ_{4n} with the sum of the other non-null eigenvalues[66]

$$\epsilon_w = \frac{\lambda^w_{4n}}{\sum_{i=1}^{4n-1}\lambda^w_i}, \qquad \epsilon_a = \frac{\lambda^a_{4n}}{\sum_{i=1}^{4n-1}\lambda^a_i}. \tag{3.34}$$

Note that without random noise these ratios will be equal to zero.

The ECM algorithm was re-written and optimised for the $n = 4$ case based on code written by earlier members of the optics group, including L.M. Aas, F. Stabo-Eeg and J. Ladstein. The resulting code can be found in appendix E.

3.2.2. Validation

The noise in $\mathbf{m}$ is related to the measurement noise in $\mathbf{b}$, as well as the noise of the inverse of $\mathbf{w}$ and $\mathbf{a}$. A validation parameter for the calibration is given by[26,66]

$$\frac{||\Delta\mathbf{M}||}{||\mathbf{M}||} \lesssim \kappa_A\frac{||\Delta\mathbf{A}||}{||\mathbf{A}||} + \kappa_W\frac{||\Delta\mathbf{W}||}{||\mathbf{W}||} + \kappa_W\kappa_A\frac{||\Delta\mathbf{B}||}{||\mathbf{B}||}, \tag{3.35}$$

where κ_W and κ_A are the condition numbers of the $\mathbf{W}$ and $\mathbf{A}$ matrices. $\Delta\mathbf{W}$ and $\Delta\mathbf{A}$ are the calibration errors, whereas $\Delta\mathbf{B}$ is intensity measurement errors. The condition number for a square non-singular matrix is defined as the ratio between the norm of itself and the norm of its inverse

$$\kappa_W = \frac{||\mathbf{W}||}{||\mathbf{W}^{-1}||}. \tag{3.36}$$

Here $||\cdot||$ represents the 2-norm, or euclidean norm, which for square $n \times n$ matrices is defined as[30]

$$||\mathbf{W}|| = \max_{\vec{x}\neq\vec{0}} \frac{||\mathbf{W}\vec{x}||}{||\vec{x}||}, \quad \vec{x} \in \mathbb{R}^n, \tag{3.37}$$

the condition number for a matrix is then the square root of the ratio between the largest and smallest eigenvalue λ^{W^*W} of $\mathbf{W}^*\mathbf{W}$ where $\mathbf{W}^*$ denotes the adjoint, or complex-conjugate transpose of $\mathbf{W}$,

$$\kappa_W = \sqrt{\frac{\lambda^{W^*W}_{\max}}{\lambda^{W^*W}_{\min}}}. \tag{3.38}$$

The reader should note that there exist other methods for calculating the condition number.

The lowest possible condition number for a matrix constructed from four Stokes vectors, i.e. the best possible polarimeter, is $\kappa = \sqrt{3}$,[67] therefore the lowest possible condition number for $\mathbf{W}$ and $\mathbf{A}$ is $\sqrt{3}$. When this is the case, the four Stokes vectors constituting the PSG/PSA will span a regular tetrahedron when inscribed on the Poincaré sphere, filling out the largest possible volume a tetrahedron embedded inside a sphere can occupy.[57]

Chapter 4

Analysing the Mueller matrix

A model can be fitted to a measured Mueller matrix in order to extract sample parameters. This method can be used to deduce e.g. sample thickness or refractive index. This approach is often used in thin film production[68,69] and is employed commercially by *J.A. Woollam Co., Inc.* in their CompleteEASE program to be used with their ellipsometers. It should be noted that this approach does not necessarily make use of the full Mueller matrix. A drawback of this method is the requirement of a priori knowledge of the sample in order to deduce sample parameters.

The Mueller matrix can also be analysed in order to get the optical properties of the sample, some of these can be extracted directly from the Mueller matrix without any assumptions. These include diattenuation, polarisance, transmittance/reflectance and depolarisation. Introducing a shorthand notation for the Mueller matrix, these properties become more evident;

$$\mathbf{M} = m_{11}\begin{bmatrix} 1 & \vec{D}^T \\ \vec{P} & \widetilde{\mathbf{m}} \end{bmatrix}, \tag{4.1}$$

where $\vec{D}$ is the diattenuation vector defined as

$$\vec{D} = \frac{1}{m_{11}}\begin{bmatrix} m_{12} \\ m_{13} \\ m_{14} \end{bmatrix} = \begin{bmatrix} D_H \\ D_{45} \\ D_C \end{bmatrix}. \tag{4.2}$$

The three components of $\vec{D}$ are called the horizontal (D_H), 45°-linear (D_{45}), and circular (D_C) diattenuation respectively. Further, the polarisance vector[70,71] $\vec{P}$ is given as

$$\vec{P} = \frac{1}{m_{11}}\begin{bmatrix} m_{21} \\ m_{31} \\ m_{41} \end{bmatrix} = \begin{bmatrix} P_H \\ P_{45} \\ P_C \end{bmatrix}, \tag{4.3}$$

where the components signify horizontal (P_H), 45°-linear (P_{45}), and circular (P_C) polarisance respectively. The sub-matrix $\widetilde{\mathbf{m}}$ is obtained by striking the first row and

column in $\mathbf{M}$ and dividing by the m_{11} element

$$\widetilde{\mathbf{m}} = \frac{1}{m_{11}} \begin{bmatrix} m_{22} & m_{23} & m_{24} \\ m_{32} & m_{33} & m_{34} \\ m_{42} & m_{43} & m_{44} \end{bmatrix}. \tag{4.4}$$

One of the important properties of the Mueller matrix is its depolarisation index, defined by Gil and Bernabeu as[72]

$$P_d = \left[\frac{\left(\sum_{i,j=1}^{4} m_{ij}^2\right) - m_{11}^2}{3m_{11}^2} \right]^{1/2}, \tag{4.5}$$

where $P_d = 1$ signifies a non-depolarising matrix, while $P_d = 0$ identifies a completely depolarising matrix.

A general Mueller matrix may be complex and difficult to fully interpret, and can be decomposed for easier analysis. One such decomposition is the forward polar decomposition,[71,73] where the Mueller matrix $\mathbf{M}$ is expressed as the product of three Mueller matrices. This imposes the assumption that all optical effects happen in a certain order. Another decomposition is the differential decomposition.[74–76] In the differential decomposition the assumption is made that the sample is adequately laterally homogeneous with respect to the resolution.[76] A third approach, called the Mueller matrix roots decomposition,[77] slices the sample into infinitesimal Mueller matrices. The latter decomposition is proven to be equivalent with the differential decomposition.[78]

4.1. Forward product decomposition

In the forward product, or *polar*, decomposition proposed by Lu and Chipman,[71] the sample matrix $\mathbf{M}$ is assumed to be a product of three Mueller matrices, each representing a different optical effect as

$$\mathbf{M} = \mathbf{M}_\Delta \mathbf{M}_R \mathbf{M}_D, \tag{4.6}$$

where $\mathbf{M}_\Delta$ is the depolarisation matrix, $\mathbf{M}_R$ is the retardance matrix, and $\mathbf{M}_D$ is the diattenuation matrix. The 4×4 diattenuation Mueller matrix is defined as

$$\mathbf{M}_D = \begin{bmatrix} 1 & \vec{D}^T \\ \vec{D} & \widetilde{\mathbf{m}}_D \end{bmatrix}, \tag{4.7}$$

where $\vec{m}_D$ is defined as the 3×3 matrix

$$\widetilde{\mathbf{m}}_D = \left(\sqrt{1 - ||\vec{D}||^2}\right) \mathbf{I}_{3\times 3} + \left(1 - \sqrt{1 - ||\vec{D}||^2}\right) \widehat{D}\widehat{D}^T. \tag{4.8}$$

Here $||\cdot||$ is the euclidean norm, while $\widehat{D}$ is the normalised $\vec{D}$ vector given by

$$\widehat{D} = \frac{\vec{D}}{||\vec{D}||} = \frac{1}{\sqrt{m_{12}^2 + m_{13}^2 + m_{14}^2}} \begin{bmatrix} m_{12} \\ m_{13} \\ m_{14} \end{bmatrix}.$$

Using $\mathbf{M}_D$ it is possible to find $\mathbf{M}_R$ and $\mathbf{M}_\Delta$ by introducing $\mathbf{M}'$, defined as

$$\mathbf{M}' = \mathbf{M}\mathbf{M}_D^{-1} = \mathbf{M}_\Delta \mathbf{M}_R.$$

These matrices can now be written as

$$\mathbf{M}_\Delta = \begin{bmatrix} 1 & \vec{0}^T \\ \vec{P}_\Delta & \widetilde{\mathbf{m}}_\Delta \end{bmatrix}, \qquad \mathbf{M}_R = \begin{bmatrix} 1 & \vec{0}^T \\ \vec{0} & \widetilde{\mathbf{m}}_R \end{bmatrix}, \qquad \mathbf{M}' = \begin{bmatrix} 1 & \vec{0}^T \\ \vec{P}_\Delta & \widetilde{\mathbf{m}}' \end{bmatrix}, \tag{4.9}$$

with

$$\vec{P}_\Delta = \frac{\vec{P} - \widetilde{\mathbf{m}}\vec{D}}{1 - ||\vec{D}||^2}. \tag{4.10}$$

The 3×3 matrix $\widetilde{\mathbf{m}}'$ is obtained in the same manner as $\widetilde{\mathbf{m}}$ by striking the first row and column of the matrix. $\vec{P}_\Delta$ is the polarisance vector of $\mathbf{M}_\Delta$. Both $\vec{P}$ and $\vec{P}_\Delta$ determine how much incoming unpolarised light is polarised by the respective Mueller matrix. From the depolarisation matrix ($\mathbf{M}_\Delta$), the depolarisation power Δ_p can be calculated in the following manner

$$\Delta_p = 1 - \frac{|\mathrm{Tr}(\widetilde{\mathbf{m}}_\Delta)|}{3} = 1 - \frac{|\mathrm{Tr}(\mathbf{M}_\Delta) - 1|}{3}. \tag{4.11}$$

From this equation it can be seen that the depolarisation will always be in the range from 0 (non-depolarising) to 1 (fully depolarising). This depolarisation index is found to be numerical similar to the one defined by Gil and Bernabeu in equation (4.5) by

$$P_d = 1 - \Delta_p \tag{4.12}$$

Given the eigenvalues λ_1, λ_2 and λ_3 of $\widetilde{\mathbf{m}}'(\widetilde{\mathbf{m}}')^T$, the diagonal matrix $\widetilde{\mathbf{m}}_\Delta$ can be constructed as[71]

$$\begin{aligned} \widetilde{\mathbf{m}}_\Delta = \pm \Big[\widetilde{\mathbf{m}}'(\widetilde{\mathbf{m}}')^T + \Big(\sqrt{\lambda_1\lambda_2} + \sqrt{\lambda_2\lambda_3} + \sqrt{\lambda_1\lambda_3} \Big) \Big]^{-1} \times \\ \Big[\Big(\sqrt{\lambda_1} + \sqrt{\lambda_2} + \sqrt{\lambda_3} \Big) \widetilde{\mathbf{m}}'(\widetilde{\mathbf{m}}')^T + \sqrt{\lambda_1\lambda_2\lambda_3}\, \mathbf{I}_{3\times 3} \Big], \end{aligned} \tag{4.13}$$

making it possible to calculate $\mathbf{M}_R$ as,

$$\mathbf{M}_R = \mathbf{M}_\Delta^{-1} \mathbf{M}', \tag{4.14}$$

in turn enabling the total retardance R to be found by

$$R = \arccos\left(\frac{\mathrm{Tr}(\mathbf{M}_R)}{2} - 1 \right). \tag{4.15}$$

A retardance vector $\vec{R}$ can be defined as

$$\vec{R} = \begin{bmatrix} Ra_1 \\ Ra_2 \\ Ra_3 \end{bmatrix} = \begin{bmatrix} R_H \\ R_{45} \\ R_C \end{bmatrix} \tag{4.16}$$

with

$$a_i = \frac{1}{2\sin R}\sum_{j,k=1}^{3}\epsilon_{ijk}(\tilde{\mathbf{m}}_R)_{jk}, \qquad i \in \{1,2,3\}, \tag{4.17}$$

where ϵ_{ijk} is the Levi-Civita permutation symbol. R_H,R_{45} and R_C are the horizontal, 45°-linear and circular retardance respectively.

By writing $\mathbf{M}_R$ as a combination of a rotated linear retarder and an optical rotation matrix (cf. section 2.5.1)

$$\mathbf{M}_R = \begin{bmatrix} 1 & 0 & 0 & 0 \\ 0 & \cos^2 2\theta + \sin^2 2\theta\cos\delta & \sin 2\theta\cos 2\theta(1-\cos\delta) & -\sin 2\theta\cos\delta \\ 0 & \sin 2\theta\cos 2\theta(1-\cos\delta) & \sin^2 2\theta + \cos^2 2\theta\cos\delta & \cos 2\theta\sin\delta \\ 0 & \sin 2\theta\cos\delta & -\cos 2\theta\sin\delta & \cos\delta \end{bmatrix} \times \begin{bmatrix} 1 & 0 & 0 & 0 \\ 0 & \cos 2\psi & \sin 2\psi & 0 \\ 0 & -\sin 2\psi & \cos 2\psi & 0 \\ 0 & 0 & 0 & 1 \end{bmatrix}, \tag{4.18}$$

it is possible to extract the linear retardance (δ), the orientation of the fast axis (θ) and the optical rotation (ψ). Using equation (4.15), the total retardance can thus be written

$$R = \arccos\left(2\cos^2\psi\cos^2(\delta/2) - 1\right). \tag{4.19}$$

This enables us to write R_C^2 as

$$R_C^2 = \frac{\sin^2\psi\cos^2(\delta/2)}{1-\cos^2\psi\cos^2(\delta/2)},$$

which can be solved to yield the linear retardance by

$$\delta = 2\arccos\left[\sqrt{R_C^2[1-\cos^2(R/2)] + \cos^2(R/2)}\right]. \tag{4.20}$$

Further, both optical rotation ψ, and fast axis angle of rotation θ, can be determined by

$$\psi = \frac{1}{2}\arcsin\left(\frac{2R_C\sin R}{1+\cos\delta}\right) \tag{4.21}$$

$$\theta = \frac{1}{2}\arctan\left(\frac{R_{45}}{R_H}\right) \tag{4.22}$$

4.2. Permutations of the forward product decomposition

The polar decomposition presented in the preceding section is part of a class of decompositions called forward polar decomposition. Forward polar decompositions assumes

that the diattenuating effect occurs before the depolarisation, giving the possible product decompositions

$$\mathbf{M} = \mathbf{M}_\Delta \mathbf{M}_R \mathbf{M}_D, \tag{4.23a}$$
$$\mathbf{M} = \mathbf{M}_\Delta \mathbf{M}'_D \mathbf{M}_R, \tag{4.23b}$$
$$\mathbf{M} = \mathbf{M}_R \mathbf{M}'_\Delta \mathbf{M}_D. \tag{4.23c}$$

To recap, $\mathbf{M}_D$, $\mathbf{M}_R$ and $\mathbf{M}_\Delta$ is the diattenuation-, retardance-, and depolarisation matrix respectively. Morio et al.[79] showed that all the forward representations are equivalent. The form given by Lu et al., (4.23a) is called the the normal form.

4.2.1. Reverse polar decomposition

The name forward polar decomposition warrants that there should exist a reverse product decomposition. Ossikovski et al.[80] proposed a polar decomposition where the depolarisation is assumed taking place before the diattenuation, which give the decompositions

$$\mathbf{M} = \mathbf{M}_{D_r} \mathbf{M}_R \mathbf{M}_{\Delta_r}, \tag{4.24a}$$
$$\mathbf{M} = \mathbf{M}_R \mathbf{M}''_{D_r} \mathbf{M}_{\Delta_r}, \tag{4.24b}$$
$$\mathbf{M} = \mathbf{M}_{D_r} \mathbf{M}''_{\Delta_r} \mathbf{M}_R. \tag{4.24c}$$

Equation (4.24a) is commonly referred to as the normal form.

The reverse decomposition defines the matrices

$$\mathbf{M}_{\Delta_r} = \begin{bmatrix} 1 & \vec{D}_{\Delta_r}^T \\ \vec{0} & \widetilde{\mathbf{m}}_{\Delta_r} \end{bmatrix}, \qquad \mathbf{M}_R = \begin{bmatrix} 1 & \vec{0}^T \\ \vec{0} & \widetilde{\mathbf{m}}_R \end{bmatrix}, \qquad \mathbf{M}_{D_r} = \begin{bmatrix} 1 & \vec{P}^T \\ \vec{P} & \widetilde{\mathbf{m}}_P \end{bmatrix}, \tag{4.25}$$

with the depolarising diattenuation $\vec{D}_{\Delta_r}$ vector defined as

$$\vec{D}_{\Delta_r} = \frac{\vec{D} - \widetilde{\mathbf{m}}\vec{P}}{1 - ||\vec{P}||^2}. \tag{4.26}$$

Following the same procedure as the forward decomposition, defining

$$\mathbf{M}' = \mathbf{M}_{D_r}^{-1} \mathbf{M} = \mathbf{M}_R \mathbf{M}_{\Delta_r} \tag{4.27}$$

the sub-matrix $\widetilde{\mathbf{m}}_{\Delta_r}$ can be calculated using equation (4.13). Observing the "transpositionlike" relationship between the two depolariser matrices $\mathbf{M}_\Delta$ and $\mathbf{M}_{\Delta_r}$ it should come as no surprise that the reverse decomposition can be solved by applying the forward polar decomposition on the transpose of the Mueller matrix. As shown by Ossikovski et al.,[80] by first transposing $\mathbf{M}$,

$$\mathbf{M}^T = \left(\mathbf{M}_\Delta \mathbf{M}_R \mathbf{M}_D\right)^T = \mathbf{M}_D^T \mathbf{M}_R^T \mathbf{M}_\Delta^T, \tag{4.28}$$

and solving the system using the forward decomposition, the reverse decomposition can be obtained by transposing the result back to their normal form.

4.2.2. Symmetric decomposition

A third product decomposition also suggested by Ossikovski[81] is called the symmetric decomposition. This decomposition handles the case where a diagonal depolarising Mueller matrix is arranged between two pairs of retarders and diattenuators

$$\mathbf{M} = \mathbf{M}_{D2}\mathbf{M}_{R2}\mathbf{M}_{\Delta d}\mathbf{M}_{R1}^{T}\mathbf{M}_{D1}. \tag{4.29}$$

A requirement for the symmetric decomposition is that the sample matrix is a *Stokes diagonalisable matrix*.[82] This means that $\mathbf{M}_{\Delta}$ must be a diagonal depolariser.

Since the symmetric decomposition is not used in this thesis it will not be further expanded on.

4.3. Differential decomposition

A differential matrix formalism for linear optically anisotropic media was first proposed for Jones matrices by Azzam[74] stemming from the work of Jones on N-matrix formalism.[83] This was later generalised for a medium exhibiting depolarisation along the light-propagation direction z.[75,76,84] In order for the differential decomposition to hold, it is assumed that the polarisation and depolarising effects occur simultaneously, and that the sample is transversally homogeneous. For all practical purposes this translates into the criterion that the sample should be adequately homogeneous in the xy-plane with respect to the resolution.

The differential matrix $\mathbf{m}'$ relates the measured Mueller matrix $\mathbf{M}$ as

$$\frac{\mathrm{d}\mathbf{M}}{\mathrm{d}z} = \mathbf{m}'\mathbf{M}, \tag{4.30}$$

which for a non-depolarising medium, the differential $\mathbf{m}'$ contains the seven elementary properties of the medium given by[74]

$$\mathbf{m}' = \begin{bmatrix} \alpha & \beta & \gamma & \xi \\ \beta & \alpha & \mu & \nu \\ \gamma & -\mu & \alpha & \eta \\ \xi & -\nu & -\eta & \alpha \end{bmatrix}. \tag{4.31}$$

Where α is the "isotropic" absorption. β, γ and ξ represents the xy linear-, ±45° linear- and circular dichroism respectively, whereas η, ν and μ are the xy linear-, ±45° linear- and circular birefringence of the sample.

By introducing symmetry breaking, the matrix

$$\mathbf{m} = \begin{bmatrix} \alpha & \beta & \gamma & \xi \\ \beta' & \alpha + \alpha_H & \mu & \nu \\ \gamma' & -\mu' & \alpha + \alpha_{45} & \eta \\ \xi' & -\nu' & -\eta' & \alpha + \alpha_C \end{bmatrix}, \tag{4.32}$$

describes depolarising media with anisotropic absorption/depolarisation along xy-linear, ±45°-linear and circular axes represented by α_H, α_{45} and α_C respectively. The primed variables and their plain counterparts are generally different in the depolarising case. The six elementary polarisation properties, dichroism d_i, and birefringence B_i, both for xy linear- ($i = H$), ±45° linear- ($i = 45$), and circular polarised ($i = C$) light, can be extracted as the mean value of the plain and primed pairs.

$$d_H = (\beta + \beta')/2 \qquad d_{45} = (\gamma + \gamma')/2 \qquad d_C = (\xi + \xi')/2 \tag{4.33}$$

$$B_H = (\eta + \eta')/2 \qquad B_{45} = (\nu + \nu')/2 \qquad B_C = (\mu + \mu')/2 \tag{4.34}$$

Assuming both the polarising and depolarising medium properties to be uniformly distributed along the propagation direction z, and the initial condition that $\mathbf{M}(z = 0) \equiv \mathbf{M}_{Air}$, i.e. assuming the differential matrix $\mathbf{m}$ is z-independent and that $\mathbf{m}$ at $z = 0$ is the identity matrix, it can be shown that equation (4.30) can be integrated to yield

$$\mathbf{L} = \ln \mathbf{M} = l\mathbf{m}, \tag{4.35}$$

where $\mathbf{L}$ is the matrix logarithm of $\mathbf{M}$ and l is the optical path length. Optical path length in this sense refers to the equivalent length light would travel in the medium if optical properties and depolarisation occurred truly simultaneously and perfectly uniformly distributed longitudinally.[76]

Introducing the Minkowski metric tensor

$$\mathbf{G} = \begin{bmatrix} 1 & 0 & 0 & 0 \\ 0 & -1 & 0 & 0 \\ 0 & 0 & -1 & 0 \\ 0 & 0 & 0 & -1 \end{bmatrix}, \tag{4.36}$$

the Lorentz antisymmetric $\mathbf{L}_m$, and symmetric $\mathbf{L}_u$ can be constructed as

$$\mathbf{L}_m = \frac{1}{2}\left(\mathbf{L} - \mathbf{G}\mathbf{L}^T\mathbf{G}\right) \qquad \mathbf{L}_u = \frac{1}{2}\left(\mathbf{L} + \mathbf{G}\mathbf{L}^T\mathbf{G}\right), \tag{4.37}$$

which yields

$$\mathbf{L}_m = \frac{1}{2}\begin{bmatrix} 0 & \beta + \beta' & \gamma + \gamma' & \xi + \xi' \\ \beta' + \beta & 0 & \mu + \mu' & \nu + \nu' \\ \gamma' + \gamma & -\mu' - \mu & 0 & \eta + \eta' \\ \xi' + \xi & -\nu' - \nu & -\eta' - \eta & 0 \end{bmatrix} \tag{4.38}$$

$$\mathbf{L}_u = \frac{1}{2}\begin{bmatrix} 2\alpha & \beta - \beta' & \gamma - \gamma' & \xi - \xi' \\ \beta' - \beta & 2(\alpha + \alpha_H) & \mu - \mu' & \nu - \nu' \\ \gamma' - \gamma & -\mu' + \mu & 2(\alpha + \alpha_{45}) & \eta - \eta' \\ \xi' - \xi & -\nu' + \nu & -\eta' + \eta & 2(\alpha + \alpha_C) \end{bmatrix}, \tag{4.39}$$

or written more clearly (with $\mathbf{L}_u' = \mathbf{L}_u - \alpha\mathbf{I}_{4\times4}$) as

$$\mathbf{L}_m = \begin{bmatrix} 0 & \overline{d}_H & \overline{d}_{45} & \overline{d}_C \\ \overline{d}_H & 0 & \overline{B}_C & \overline{B}_{45} \\ \overline{d}_{45} & -\overline{B}_C & 0 & \overline{B}_H \\ \overline{d}_C & -\overline{B}_4 5 & -\overline{B}_H & 0 \end{bmatrix} \quad \mathbf{L}_u' = \begin{bmatrix} 0 & \Delta d_H & \Delta d_{45} & \Delta d_C \\ -\Delta d_H & \alpha_H & \Delta B_C & \Delta B_{45} \\ -\Delta d_{45} & \Delta B_C & \alpha_{45} & \Delta B_H \\ -\Delta d_C & \Delta B_{45} & \Delta B_H & \alpha_C \end{bmatrix}. \tag{4.40}$$

For each property p_i accumulated over path length l, $\overline{p}_i$ denotes the average, while the uncertainty is represented by Δp_i.

From the elements of $\mathbf{L}_m$ and $\mathbf{L}_u$ the accumulated depolarisation Δ_p', dichroism d, linear retardance δ and its orientation θ, optical rotation ψ, and retardance R can be extracted as

$$\Delta_p' = \frac{1}{3}|3\alpha + \alpha_H + \alpha_{45} + \alpha_C|, \tag{4.41a}$$

$$d = \sqrt{\overline{d}_H^2 + \overline{d}_{45}^2 + \overline{d}_C^2}, \tag{4.41b}$$

$$\delta = \sqrt{\overline{B}_{45}^2 + \overline{B}_H^2}, \tag{4.41c}$$

$$\theta = \frac{1}{2}\arctan\left(\frac{\overline{B}_{45}}{\overline{B}_H}\right), \tag{4.41d}$$

$$\psi = \frac{1}{2}\overline{B}_C, \tag{4.41e}$$

$$R = \sqrt{\overline{B}_H^2 + \overline{B}_{45}^2 + \overline{B}_C} = \sqrt{\delta^2 + 4\psi^2}. \tag{4.41f}$$

The standard deviation for these parameters, except for the depolarisation, follows readily from standard propagation of error calculations,[85] e.g. for the angle of fast axis[86]

$$\sigma_\theta = \frac{\sqrt{\left(\Delta B_{45}\overline{B}_H\right)^2 + \left(\Delta B_H\overline{B}_{45}\right)^2}}{2\left(\overline{B}_{45}^2 + \overline{B}_H^2\right)}. \tag{4.42}$$

In order to compare the polar and differential decomposition one can derive the relations[76]

$$D = \tanh(d), \tag{4.43a}$$

$$\Delta_p^{\mathrm{diff}} = 1 - \frac{\mathrm{e}^\alpha}{3}(\mathrm{e}^{\alpha_H} + \mathrm{e}^{\alpha_{45}} + \mathrm{e}^{\alpha_C}), \tag{4.43b}$$

for the diattenuation D and depolarisation Δ_p^{diff}, which introduces the same limiting values of 0 and 1 as the product decomposition for these quantities. As noted by Ellingsen et al.,[85] the signs of the exponentials as suggested by equation (19) in the paper by Kumar et al.[76] is wrong.

It should be noted that the differential decomposition is reported to currently only work for measurements in transmission (forward scattering), as it breaks down for Mueller matrices in the backscattering regime.[87]

4.4. Mueller matrix roots decomposition

In the Mueller matrix roots decomposition proposed by Noble et al,[77,88] the medium is subdivided along its length into infinitesimal slices. The Mueller matrix of each slice contains the commuting elementary polarisation properties.

The roots decomposition can be seen as a special kind of a continuous (i.e. differential) product decomposition since the product of the infinitesimal Mueller matrices yields the original matrix $\mathbf{M}$. Formulated in mathematical terms, the roots decomposition algorithm consists of calculating the limit given by

$$\mathbf{D} = \lim_{q\to\infty} q\left(\sqrt[q]{\mathbf{M}} - \mathbf{I}\right), \tag{4.44}$$

where q is the number of slices. In practice this is done for a sufficiently large q. A q in the order of 10^5 is reported to give good results.[77]

Equation (4.44) can readily be solved for $\mathbf{M}$,[78] yielding

$$\mathbf{M} = \lim_{q\to\infty} \left(\mathbf{I} + \frac{1}{q}\mathbf{D}\right)^q = \exp(\mathbf{D}), \tag{4.45}$$

from which it follows that $\mathbf{D} \equiv \mathbf{L}$ by looking at equation (4.35). Hence, the roots and differential decompositions are equivalent although obtained from different mathematical standpoints.[78]

4.5. Out of plane directional calculation based on different incidence angles

A method to determine the direction of linear retarding fibres have previously been reported by Ellingsen et al.[27,85] and will be presented here.

Let the laboratory frame of reference be defined such that the x-axis points along the direction of illumination, the y-axis is horizontal, and the z-axis is vertical as seen in figure 4.1. A vector in the laboratory frame of reference can be defined by

$$\vec{p} = \begin{bmatrix} x, & y, & z \end{bmatrix}, \tag{4.46}$$

whereas a vector in the sample frame of reference can be described by

$$\vec{p}\,' = \begin{bmatrix} x', & y', & z' \end{bmatrix}. \tag{4.47}$$

At a rotation of $\alpha = 0°$, the sample and laboratory frames of reference coincides as can be seen from figure 4.1. Since the sample is only rotated around the $z = z'$ axis (fig. 4.1 and 4.2), the Euler rotation matrix[89]

$$\mathbf{R}(\alpha) = \begin{bmatrix} \cos\alpha & \sin\alpha & 0 \\ -\sin\alpha & \cos\alpha & 0 \\ 0 & 0 & 1 \end{bmatrix}, \tag{4.48}$$

can be used to transform between the reference and the laboratory frame.

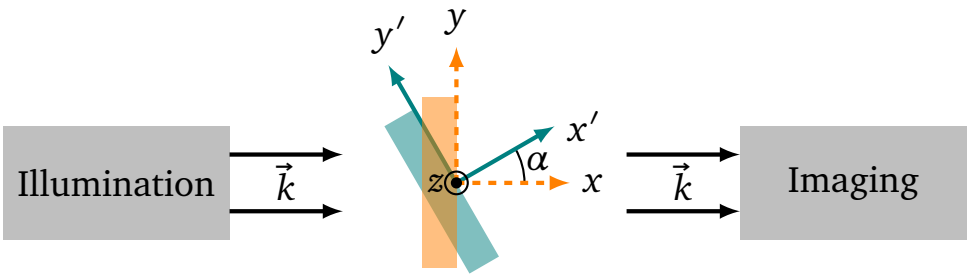

Figure 4.1: Rotation α of the sample as seen from above.

By using the aforementioned transformation, it is possible to transform the sample frame of reference $\vec{p}\,'$ into the laboratory frame of reference $\vec{p}$ by

$$\vec{p} = \mathbf{R}(-\alpha)\vec{p}\,'. \tag{4.49}$$

Applying this transformation gives the relations

$$x = x'\cos\alpha - y'\sin\alpha, \tag{4.50a}$$
$$y = x'\sin\alpha + y'\cos\alpha, \tag{4.50b}$$
$$z = z'. \tag{4.50c}$$

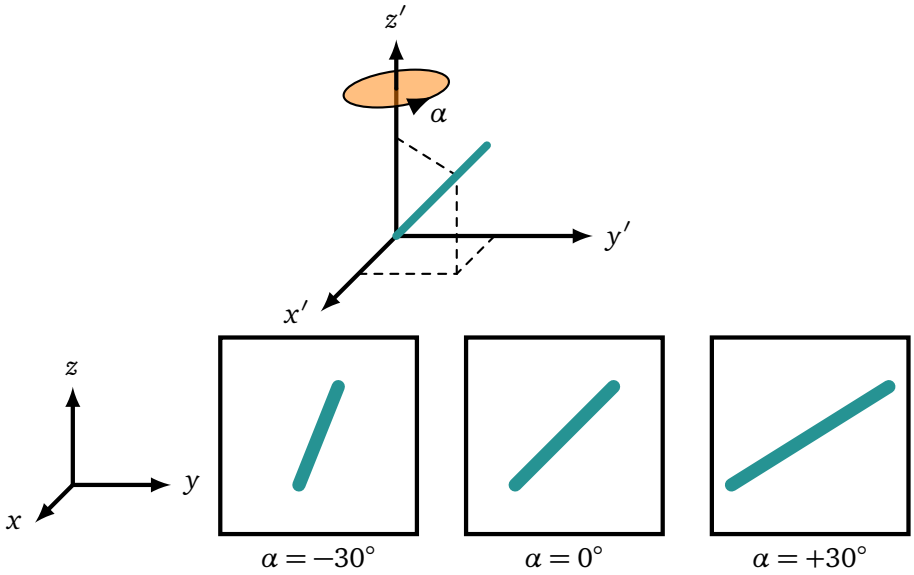

Figure 4.2: Coordinate systems used for the caluclation of the directions. The laboratory frame $[x, y, z]$ is coincident to the sample frame of reference $[x', y', z']$ at $\alpha = 0°$. The x-axis points along the path of illumination towards the image. The z-axis is vertical and the y-axis is horizontal. Since the rotation α is around the z-axis, $z' = z \quad \forall \alpha$. A projection of a three dimensional fibre onto the imaging plane is illustrated for different angles α in the lower row of figures. Figure reproduced from original paper.[85]

By measuring the Mueller matrix at two different rotations, α_1 and α_2, it is possible to determine $\vec{p}\,'$ by using the measured (y_1, z_1) and (y_2, z_2) in the laboratory frame. By choosing $\alpha_2 = -\alpha_1 = \alpha$ ($\alpha_2 < 0$ due to the direction of rotation in the presented configuration), and solving equation (4.50), the resulting components of $\vec{p}\,'$ are[85]

$$x' = \frac{y_2 - y_1}{2\sin\alpha}, \qquad y' = \frac{y_1 + y_2}{2\cos\alpha}, \qquad z' = z_1 = z_2. \tag{4.51}$$

Since the MMI measurements can only yield the direction of the slow axis θ, and not the length projected onto the image (yz-plane), it is not possible to find the absolute length of the vector. By defining the projected length as

$$\begin{aligned} l &= \sqrt{y^2 + z^2} \\ &= \sqrt{(x'\sin\alpha)^2 + (y'\cos\alpha)^2 + 2x'y'\sin\alpha\cos\alpha + (z')^2}, \end{aligned}$$

it is possible to define the coordinates with respect to the measured angles

$$\begin{aligned} y_1 &= l_1\cos\theta_1, & z_1 &= l_1\sin\theta_1, \\ y_2 &= l_2\cos\theta_2, & z_2 &= l_2\sin\theta_2. \end{aligned}$$

Exploiting the fact that $z_1 = z_2 = z$, we now find that

$$y_1 = z\cot\theta_1, \qquad y_2 = z\cot\theta,$$

which can be inserted into equation (4.51), yielding

$$x' = \frac{z(\cot\theta_2 - \cot\theta_2)}{2\sin\alpha}, \qquad y' = \frac{z(\cot\theta_1 + \cot\theta_2)}{2\cos\alpha}, \qquad z' = z. \tag{4.52}$$

Since we are only interested in the direction, z can be chosen arbitrarily. This solution is limited to only include positive values for z, which is not a concern since all solutions with negative z can be represented by the opposite vector located in the positive z space.[85] It will also not be possible to get a solution purely in the xy plane ($z = 0$). In addition, the rotation around z means that it is not possible to see the difference between different vectors in the xy plane as long as $z = 0$. Choosing $z = 1$, the final equations become

$$x' = \frac{\cot\theta_2 - \cot\theta_2}{2\sin\alpha}, \qquad y' = \frac{\cot\theta_1 + \cot\theta_2}{2\cos\alpha}, \qquad z' = 1. \tag{4.53}$$

A consideration to take into account is that the angle of incidence is not the same as the rotation angle of the sample, due to the difference in refractive index. This change in refractive index yields a correction for α which is

$$\alpha = \arcsin\left(\frac{n_0 \sin\alpha_r}{n_m}\right), \tag{4.54}$$

where α_r is the angle of rotation, n_0 is the refractive index of the surrounding medium and n_m is the refractive index of the medium being imaged.

Part II.

Mueller Matrix Measurements and Analysis of the Results

Chapter 5

Performing Mueller matrix measurements

A Mueller Matrix Imaging Ellipsometer (MMI) developed by J. Ladstein[52,90,91] and F. Stabo-Eeg,[26,66,92] with improvements done by H. O. Skjerping,[93] L. M. S. Aas[94–96] and P. G. Ellingsen,[27,85,97] among others, was used to perform the ellipsometric measurements presented in chapter 6.

The computer running the MMI-instrument was upgraded from a 32-bit machine to a 64-bit machine, which resulted in multiple issues with hardware drivers. In order to correct these issues the entire LabVIEW backend including most sub-routines controlling the MMI was rewritten. The new program is based on the old one, although many of the subVIs had to be completely rewritten in order to effectively resolve the driver problems. In section 5.2 the front panel of the new program is described.

As a programming exercise, the ECM-routine described in 3.2.1 was implemented in MATLAB based on an older implementation. The new routine, listed in appendix E, was found to work approximately 40 % faster than the old one, while yielding numerical similar results. The reworked algorithm was therefore implemented in the LabVIEW program.

5.1. Hardware

The basic design of the MMI is presented in Jarle Ladsteins Master's thesis[90] and expanded on in the Master's theses by Hallvard Olsen Skjerping,[93] Pål Ellingsen,[27] and Lars Martin Sandvik Aas[94] among others. The design and components will be outlined in this thesis. The PSA and PSG each consist of two true zero order waveplates from *CASIX*, and two FLCs from *Citizen Finetech Miyota*,[‡] as well as a polariser. The components of the PSG are ordered as

[‡]Formerly known as *Displaytech*.

1 – Polariser,
2 – QWP $\lambda/4$ @ 465 nm,
3 – FLC1 $\lambda/2$ @ 510 nm,
4 – HWP $\lambda/2$ @ 1008 nm,
5 – FLC2 $\lambda/2$ @ 1020 nm,
with the PSA components ordered in reverse as illustrated in figure 5.1. The FLCs are driven by *Displaytech* DR-95 FLC drivers[§] which are controlled by a *National Instruments* NI SCB-68 I/O connector.

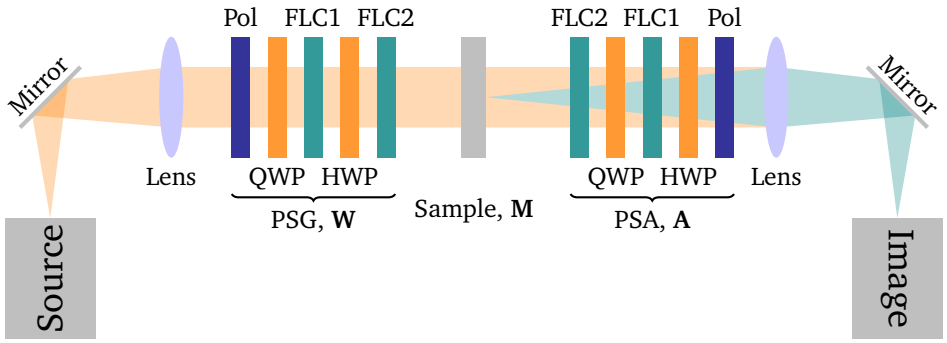

Figure 5.1: Schematic of the MMI used for measurements in this thesis.

The configuration has two interchangeable light sources, a 940 nm LED from *Thorlabs* designated M940L2-C2 and a custom 1300 nm LED. At the receiving end a *Lumenera* Lw11059M Si-based CCD camera, or a *Xenics* Xeva XC137 InGaAs NIR camera can be used. Since the detectors operate using different drivers, separate programs controlling them in conjunction with the rest of the MMI has been written.

A motorised xy- and rotational stage is part of the set-up. The stage consist of a *Thorlabs* LTS300 stepper motor with dedicated driver in the x-direction, a *Standa* 8MT175 motor in the y direction, and a *Standa* 8MR191 stepper motor for rotation. Both Standa stages are driven by *Standa* 8SMC1-USBhF drivers.

For calibrating the system, air, a waveplate, and two polarisers are used. The calibration samples are automatically changed during calibration using a *Thorlabs* filterwheel.

The instrument is controlled using *National Instruments* LabVIEW 2012, with subroutines written in MATLAB-code. The machine running the software is a 64-bit PC with a Windows 7 operating software.

5.2. LabVIEW operation

Before starting the program, the FLC-drivers, camera and stepper-motors should all be connected and powered up. At start-up, the program will try to connect with this

[§]New FLC drivers based on the Displaytech drivers are currently in prototype development in-house at *Elektronikkverkstedet*. This is done so that the old MMI and the new μMMI can be operated simultaneously.

equipment. If it is unable to connect to any of the equipment, an error message will display and the program is terminated. After the start-up procedure, the user will be presented with the graphical user interface (GUI) shown in figure 5.2.

5.2.1. GUI

The GUI is divided into three main parts, a control panel, a camera feed, and an intensity histogram, as shown in figure 5.2. Buttons for starting measurements and terminating the program are located below the control panel. A progress bar based on the number of images to be taken is displayed below these buttons.

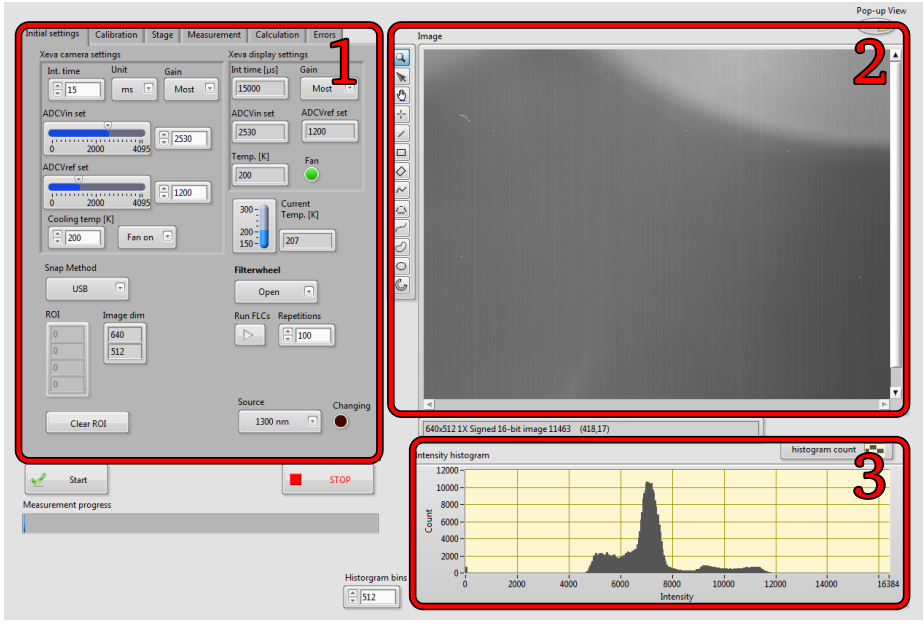

Figure 5.2: Layout of the graphical user interface for the LabVIEW program created as part of this thesis. **1)** Control-panel **2)** Camera feed. **3)** Intensity histogram.

1) Control panel

The control panel is ordered into tabs for easy access to the different setting. The control panel is explained in greater detail in the following sections.

2) Camera feed

A live camera feed is shown in this window. An optional pop-up view of the image can be opened by pressing the *Pop-up View* button located in the top-right corner. Tools for selecting a region of interest (ROI) is located to the left. The ROI can be marked in both *Snap modes,* but will only take effect when the *Framegrabber-method* is selected. Note that the program automatically switches to the Framegrabber-method

when measuring. The ROI reset button and Snap method selector is located under the *initial settings* tab in the control panel.

2) Intensity histogram

The intensity histogram spans values from 0 to $2^{14}-1$ corresponding to the Xeva camera bit-depth. The camera expresses non-linear behaviour at low and high intensities, the user should therefore try to avoid these regimes by adjusting the camera settings and/or back lightning. In order to get a good dynamic range in the measurements, the intensity difference between dark and light areas should be as high as possible. This can be achieved by adjusting the camera settings while opening and closing the filterwheel.

5.2.2. Initial settings

The initial setting tab is broken down into five main sections (see fig.5.3), these include changing and reading camera settings, selecting snap method and ROI information, filterwheel control and FLC jolting, and source selection.

1) Change camera settings

The settings for the Xeva camera is adjusted in this part of the settings tab. A low integration time (around 10 ms) is preferable as the FLCs have been found to drift over time.

2) Display current camera settings

Check that the settings read from the camera corresponds to the one set by the user. If the settings differ this could indicate communication failure with the camera. It is advisable to wait until the temperature has reached the set point before taking measurements, as a change in temperature will affect the camera response.

3) Snap method and ROI control

The snap method can either be *USB* or *Framegrabber*. The ROI can be set under both methods, but will only take effect under the Framegrabber method. Only square regions are supported. The ROI indicator display the position of the lower left corner and upper right corner of this rectangle. By pressing *Clear ROI* the ROI will be reset.

4) Filterwheel and FLC jolting

Using the *Filterhweel* drop-down menu the different inserted components can be selected. Some of the crystals in the FLCs may be stuck if the FLCs have been inactive for prolonged periods of time, they therefore may need a small jolt to get unstuck.

This can be done by clicking the *Run FLCs* button, a few hundred repetitions is usually enough.

5) Source selection

The two available sources can be changed between using the *Source* drop-down menu. The *Changing* indicator will light up when the source is changing.

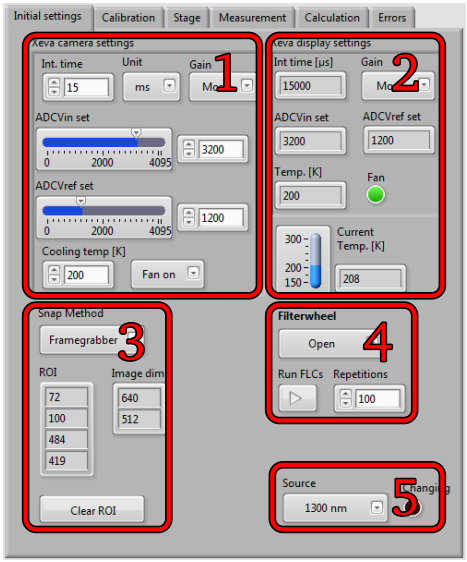

Figure 5.3: Initial settings. **1)** Change Xeva camera settings. **2)** Read current camera settings. **3)** Snap method and region of interest (ROI) information. **4)** Filterwheel and FLC jolting. **5)** Source picker.

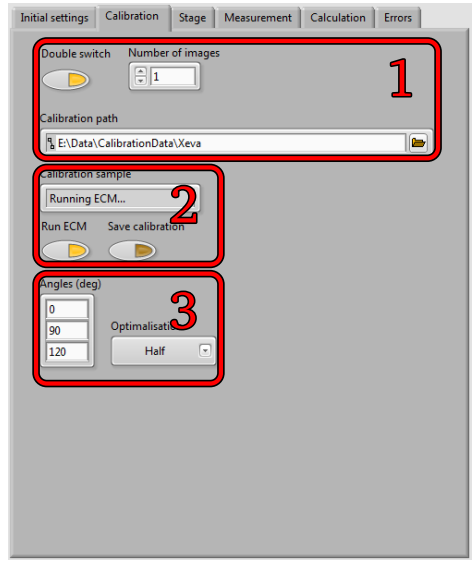

Figure 5.4: Calibration panel. **1)** FLC inversion, number of images and save location. **2)** Sample indicator and checkboxes for running ECM and saving the results. **3)** Sample orientation and optimisation.

5.2.3. Calibration pane

The calibration pane is presented in figure 5.4, where the basic calibration controls are found.

1) FLC inversion, number of images, and save path

The FLCS have been found to deteriorate with age, which means that they start drifting after they've been switched. Under normal operation, as not all FLCs are switched at a time. A workaround was found by switching all the FLCs to the inverse position before switching them back to their intended position. This FLC inversion is carried out if the *Double switch* button is active. The *Number of images* determines how many images each measurement is averaged over, a higher number may decrease the amount of

random noise. The files generated under the calibration is stored in the *Calibration path* location.

2) Sample indicator and ECM control

Which calibration sample is measured is displayed in the *Calibration sample* indicator. When all samples have been measured and the *Run ECM* button is activated, the indicator will show *Running ECM...* and a window will pop up showing the progress of the ECM algorithm. If *Save calibration* is activated, the results from the ECM will be saved in the calibration folder. The MATLAB ECM routine called on is listed in appendix E.

3) Calibration sample azimuthal angle

As explained in section 3.2.1 the azimuthal angles of the calibration samples must be known in order to fully calibrate the system. Approximate azimuthal angles is provided using the *Angles (deg)* input node. The user can then choose to optimise the angles using equation (3.34) for either all image pixels, or only some of them. An option to perform no optimisation is also provided for quick calibration checks. It is encouraged to optimise over all pixels for the final calibration.

5.2.4. Stage control

The connections and operation of the stepper motors are displayed under the *Stage* tab shown in figure 5.5.

1) µSMC profiles and connection

In order to properly control the Standa stages correct profiles must be loaded. If a stages is replaced with a different model, the profile should also be exchanged. Profiles can be made using the *SMCVieW* program. The stages must also be identified using a device number, if one of the stages appear to function improperly, try changing the device number first.

2) µSMC handles

Handle indication for the stages used for troubleshooting.

3) ActiveX MG17 Motor controller

The Thorlabs MG17 motor may be controlled directly using the provided ActiveX controller.

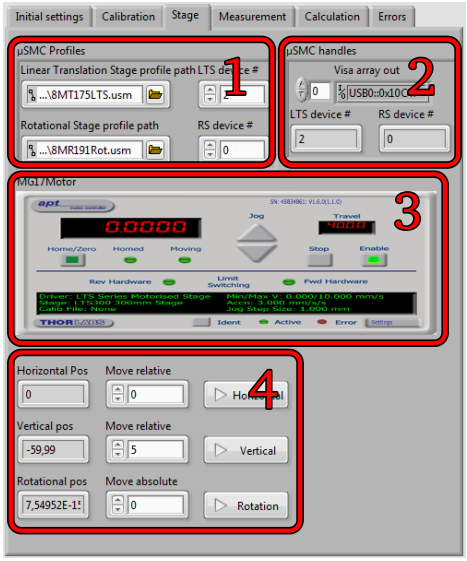

Figure 5.5: Stage control. **1)** Stage profiles and number. **2)** Device handles. **3)** ActiveX controller. **4)** Position indicators and movement controls.

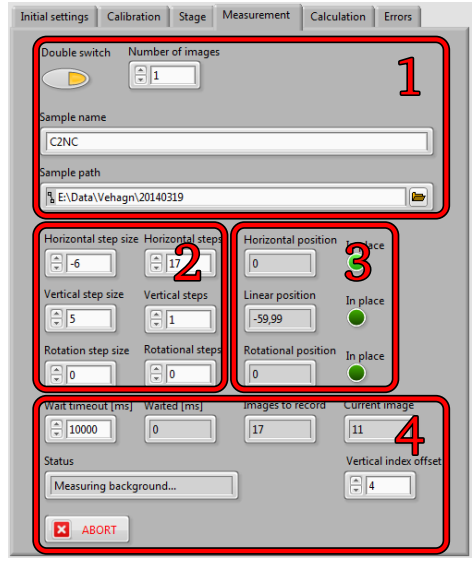

Figure 5.6: Measurement tab. **1)** FLC inversion, images, sample name, and save location. **2)** Stage scanning controls. **3)** Position indicators. **4)** Misc. controls

4) Position indicators and movement control

Current position indicators are placed to the left. The stages may be moved by inputting the desired value in one of the boxes before clicking the corresponding button for horizontal, vertical or rotational movement.

5.2.5. Measurement tab

Measurement and scan settings are found under the *Measurement* tab as displayed in figure 5.6.

1) Sample name and save location

The *Double switch* button should be checked in order to avoid FLC drift. To average over more images for each measurement, the *Number of images* setting can be increased. The sample name and save location should be input in their respective text-box. All measurements will be saved in the sample path location with a date-stamp, sample name and scan position.

2) Stage scanning controls

Larger samples must be scanned in order to image the full sample. This is done by moving the stage appropriately between each image. The amount of movement

between each image and the number of steps are selected with these controls. A rotational step size of 1 means the stage will go to ± the degree set. The scan will complete a horizontal sweep before moving a step in the vertical direction and return the horizontal stage to its starting position.

3) Position indicators

Current position of the stages can be read in this pane. When the stages are in place the *In place* indicator will light up. The vertical stage sometimes struggle get to the absolute correct position, in this case the measurement will continue once the time-out has been reached.

4) Miscellaneous measurement controls and indicators

The wait time-out can be set using the *Wait timeout* control. The time-out is used as a back-up in case one of the stages fails to accurately reach its designated position. When the time-out has been reached the measurement will continue regardless if the stages are in place or not. The time-out should not be set too low as the horizontal stage may take some seconds to travel large distances. If a scan is resumed, the *Vertical index offset* may be used in order to get a correct numbering of the output files. Indicators of the number of images to be recorded, current image and status can also be found in this area. A measurement may be aborted at any time by pressing the *ABORT* button. Please be patient after pressing this button as certain steps must be completed in order to terminate a measurement.

5.2.6. Calculation tab

The calculation tab seen in figure 5.7 gives access to the calculation tool. Controls for analysing measurements directly in LabVIEW are yet to be implemented.

1) Path indicators

Sample and calibration location indicators. The sample path may be set under the *Measurement* tab, while the calibration path can be set under the *Calibration* tab.

2) ECM control

These controls give quick access to running the ECM-routine, see section 5.2.3 for more details. The latest calibration can also be loaded and inspected using the respective buttons.

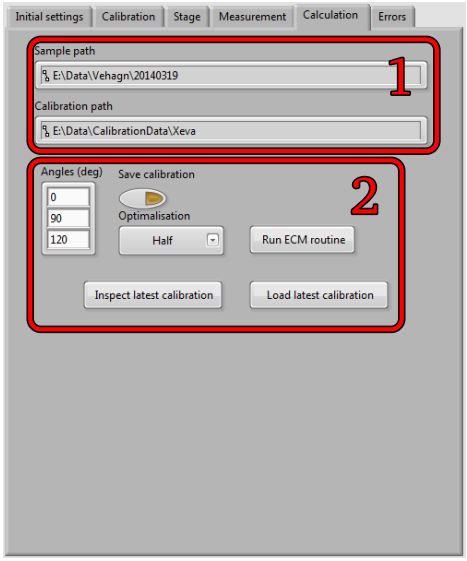

Figure 5.7: Calculation pane. **1)** Path indicators. **2)** ECM tools.

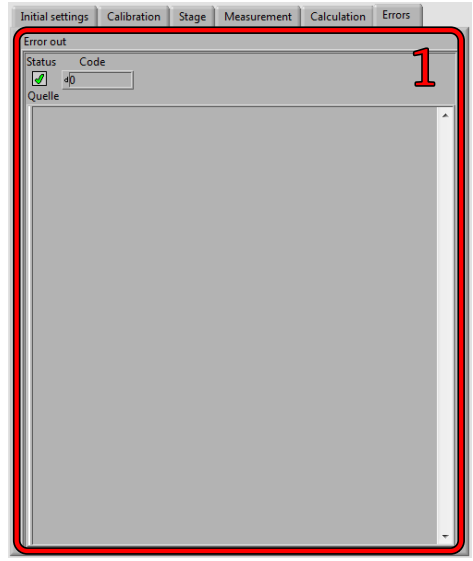

Figure 5.8: Error indication. **1)** Errors are output here.

5.2.7. Error messages

Any errors that might happen during program operation will be displayed in the error window shown in figure 5.8. Most errors will also halt the program and give a pop-up message containing the error.

5.3. Remarks on the code

When scanning large samples, the time used for each picture grows exponentially, it is therefore advised to measure bigger samples in smaller chunks and resetting the program after each chunk. This unwanted behaviour was also present in the old program and effort has been put into diagnosing the problem in both version. The troubleshooting has regrettably been unsuccessful. A workaround is proposed where the camera is disconnected and reconnected every n-th picture in order to resolve the issue.

Linearisation of the Xenics Xeva camera should be carried out in order to get a better dynamic range in the measurements. The current solution of only using the middle regime which is approximately linear was found to be adequate for the study carried out in this thesis.

Currently only the software controlling the Xeva detector has been rewritten. The program controlling the Lumenera does function on the new machine, albeit somewhat unstable. It is advisable to create a suite controlling both cameras to increase compatibility. The reader is strongly encouraged to improve on the existing code.

5.4. Calibration results

Two different configurations of the MMI were used during this thesis. The Xenics camera was used together with the 1300 nm source to image inorganic samples, while the Lumenera camera was used in conjuction with the 940 nm source to measure an organic sample. Since the configurations differ, calibration results from each configuration together with a resolution image is presented in this section.

The highest, i.e. best theoretical inverse condition number of a matrix constructed from four Stokes vectors is $1/\sqrt{3}$.[67] A low inverse condition number for the analyser or modulation matrices correspond to a bad calibration. In order to attain a high inverse condition number, the system must be well designed and suitable calibration samples must be used. Histograms of the inverse condition number for the **W** and **A** matrices resulting from the calibration of the two configurations are presented in figure 5.9. The design maximum inverse condition number is labelled at the top of the histogram for 1300 nm and 940 nm.[90]

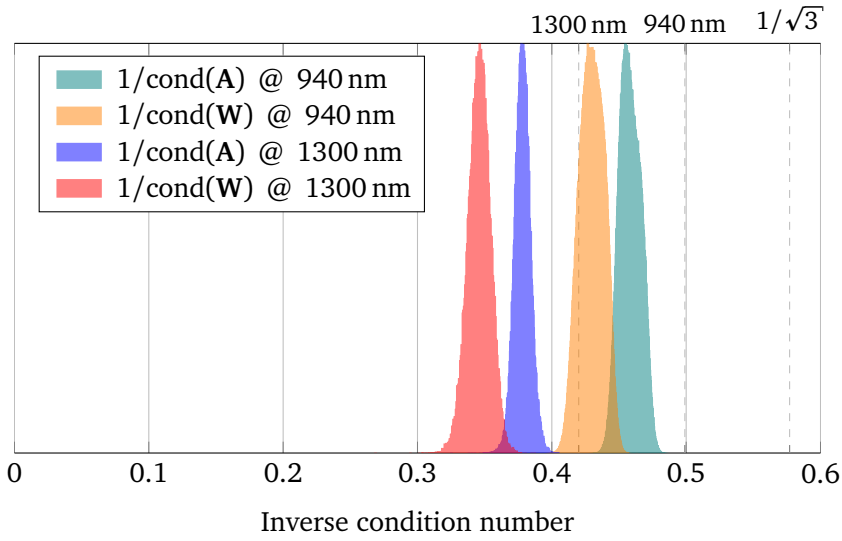

Figure 5.9: Normalised inverse condition number histograms for the PSG (**W**) and PSA (**A**) matrices in two configurations. Design maximum inverse condition numbers for select wavelengths are indicated at the top.

A second calibration check is looking at the reconstructed Mueller matrix of the calibration samples, especially the air measurement, which will give an estimate of the measurement error. Figures of the reconstructed Mueller matrices can be seen in figure 5.10 and 5.11. $\mathbf{M}_0$ is an air measurement. $\mathbf{M}_1$ and $\mathbf{M}_2$ are polarisers oriented at approximately 0° and 90° respectively. $\mathbf{M}_3$ is a retarder with fast-axis oriented at approximately 120°.

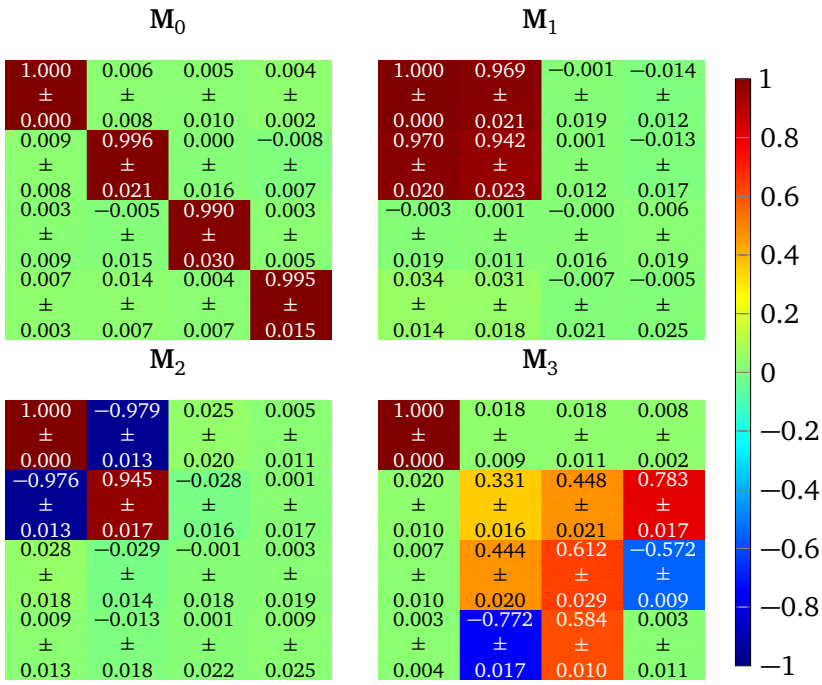

Figure 5.10: Calibration results from the Xeva camera and a 1300 nm source.

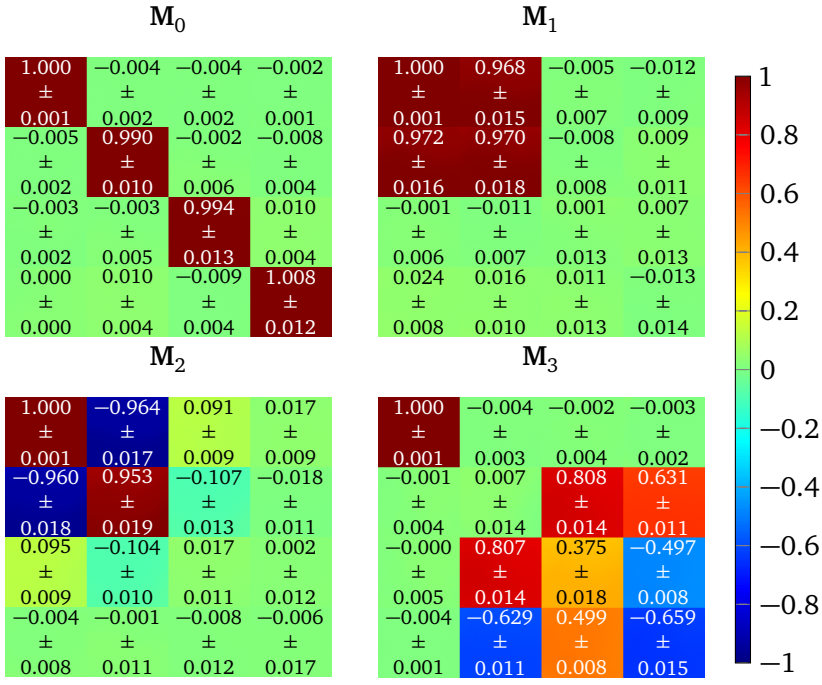

Figure 5.11: Calibration results from the Lumenera camera and a 940 nm source.

5.4.1. Image resolution

Image resolution and pixel size is important for determining the feature size and comparing images. In order to determine the resolution and pixel size of the images, a *Resolution Test Target* from *Newport*[‡] was imaged. The results are summarised in table 5.1 with the images presented in figure 5.12 and 5.13.

Table 5.1: Image resolution and pixel size for the Xeva and Lumenera cameras.

	Resolution	Pixel size
Xeva	27.8 µm	24.5 µm × 24.5 µm
Lumenera	15.6 µm	11.4 µm × 11.4 µm

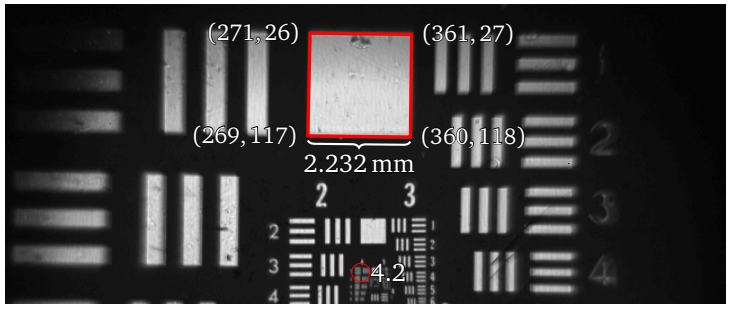

Figure 5.12: *Resolution Test Target* image taken using the Xeva camera. Approximately 91 pixels constitute each side of the 0.2 element.

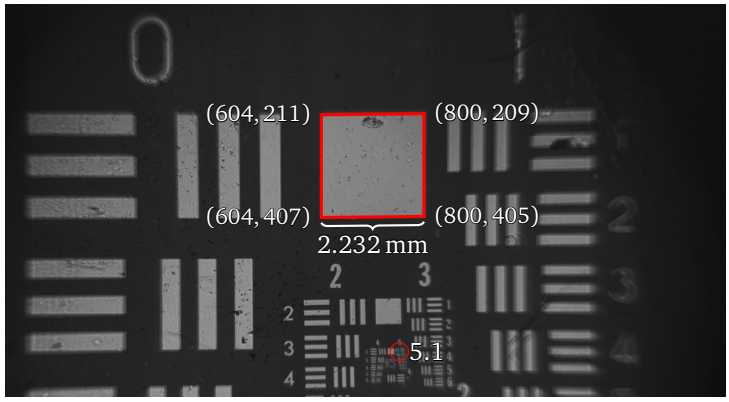

Figure 5.13: *Resolution Test Target* image taken using the Lumenera camera. Approximately 196 pixels constitute each side of the 0.2 element.

[‡]http://www.newport.com/Resolution-Test-Targets/141210/1033/info.aspx accessed 13th June 2014.

Chapter 6

Results and discussion

In this chapter, results obtained using the MMI instrument presented in chapter 5 will be discussed. Measurements of both inorganic (sec. 6.1) and organic (sec. 6.2) samples are presented to highlight different uses of the MMI.

6.1. Strain induced birefringence in two bi-crystal silicon ingots

Multicrystalline silicon (mc-Si) has a tendency to contain a wide range of structural defects which deterioates the material quality. Dislocations are linear structural defects, and have been identified as a major obstacle in manufacturing high performance mc-Si based solar cells. A dislocation density higher than $10^4\,\mathrm{cm}^{-2}$ has been observed to contribute to a drastic decrease of solar cell efficiency.[98,99] Average dislocation densities ranging from $10^4\,\mathrm{cm}^{-2}$ to $10^6\,\mathrm{cm}^{-2}$, with local dislocation densities up to $10^8\,\mathrm{cm}^{-2}$ have been measured in industrial mc-Si,[100] it is therefore important to lower dislocation emission during mc-Si growth in order to produce more efficient mc-Si solar cells at a lower cost.

Grain boundaries are interfaces or planar defects that separate regions of different crystallographic orientation, and have been found to be a major source of dislocations in mc-Si.[101,102] These dislocations are generated and multiplied in the silicon ingot at high temperatures during growth and cooling. In a strained multi-crystal, the grain boundary surfaces are found the be concentrating stresses in order to preserve the compatibility of the grains at the grain boundary interface region. It has been shown by Varin et al. that shear-stresses as low as $G/1000$ to $G/400$, where G is the shear modulus of the material in GPa, applied at grain boundaries can start local plastic deformation which is responsible for dislocation generation and emission.[103] The shear modulus for crystal silicon is found to be 51 GPa to 80 GPa,[104] which dictates that shear stresses as low as 51 MPa could be responsible for dislocation generation and emission in crystal silicon.

One type of grain boundary is high angle tilt boundaries in which the misorientation between two grains of silicon exceeds 10° to 15° (see fig. 6.2).[105] This leads to the dislocation cores overlapping due to the small dislocation spacing. The energies of the grain boundaries in this situation are largely independent of the misorientation. General high angle grain boundaries give areas of poor fit and a relatively open structure, however, there exist special high angle grain boundaries called coincident site lattice (CSL) boundaries with an ordered structure and lower energies than random high angle boundaries. These CSL boundaries are denoted by a Σ-value which represents the reciprocal density of coincident sites, e.g. in a Σ3 CSL the adjoining boundaries share every third atom. Studies have shown that in silicon, a very high fraction of grain boundaries are ⟨110⟩ tilt boundaries with Σ3, 9 or 27.[106]

Studies of silicon under applied strain have shown that stresses arise preferentially in certain grains,[101,107] caused by the the anisotropic mechanical properties of silicon.[108,109]

As mentioned in section 2.7.1, silicon is an optically isotropic crystal, but when subjected to mechanical stress it becomes optically anisotropic and will display birefringence, as described in section 2.7.2.

The presented results are up for publication in the Journal of Crystal Growth by A. Autruffe, V. S. Hagen, L. Arnberg and M. D. S. Lundberg.[110] The author contributed with MMI measurements and analysis.

6.1.1. Sample preparation

Small silicon bi-crystals measuring 55 mm in height and 32 mm in diameter, and weighing 100 g were grown in a small Bridgman furnace illustrated in figure 6.1, using a seeded growth process.[111,112] Silicon nitride coated alumina crucibles were used. The pulling rate was 3 μm/s. Half cylinders oriented in the ⟨110⟩ direction were drilled out from a Czochralski monocrystalline ingot solidified in the ⟨100⟩ direction and used as seeds. Controlled tilt misorientation was introduced between the seeds (see figure 6.2) in order to manufacture Σ9 and Σ27*a* coincident site lattice grain boundaries. The introduced tilt misorientation were 38.9° and 31.6° around the ⟨110⟩ direction for the Σ9 and Σ27*a* grain boundaries respectively.[113]

The seed grain boundary natures have been confirmed by electron back scattered diffraction mappings (EBSD) on vertical cross sections. For the Σ27*a* seed, the grain boundary planes have been identified to be mainly of the $\Sigma 27a\{511\}_1/\{511\}_2$ configuration.

The samples, provided by Antoine Autruffe as part of his PhD studies,[110] were cut into 2 mm thick vertical cross sections and polished with diamond slurry down to 1 μm in size.

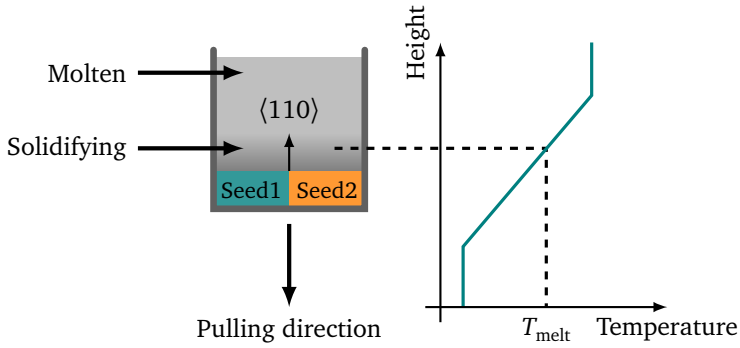

Figure 6.1: Vertical cross-section of a Bridgman furnace. The temperature profile is held constant while the crucible is slowly lowered down. T_{melt} is the melting temperature of silicon. Illustration reproduced from original paper.[110]

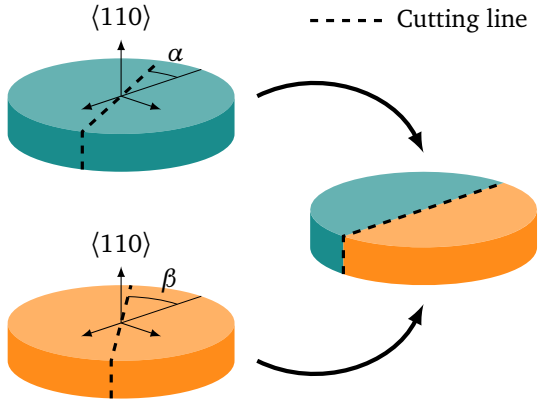

Figure 6.2: The seeds were prepared from a Czochralski monocrystalline ingot solidified in the ⟨100⟩-direction, where two half-cylinders oriented in the ⟨110⟩-direction have been drilled out. Controlled tilt misorientation around the ⟨110⟩ of 38.9° and 31.6° was introduced between the wafers to induce Σ9 and Σ27*a* grain boundaries respectively.[113] α and β represents the angles where the cuts were made. Illustration reproduced from original paper.[110]

6.1.2. Measurements

To check for stress-induced birefringence, the samples were measured using the MMI described in chapter 5 using the collimated 160 mW LED with centre wavelength 1300 nm and the Xenics Xeva InGaAs detector. The obtained Mueller matrices (fig. 6.3 and fig. 6.4) were decomposed using the forward polar product decomposition presented in section 4.1, after first being Cloude filtered as outlined in section 2.6.1. The most interesting results obtained from the decomposition is displayed in figures 6.5-6.10, namely the linear retardance, orientation of in-plane fast/slow axis, and degree of depolarisation.

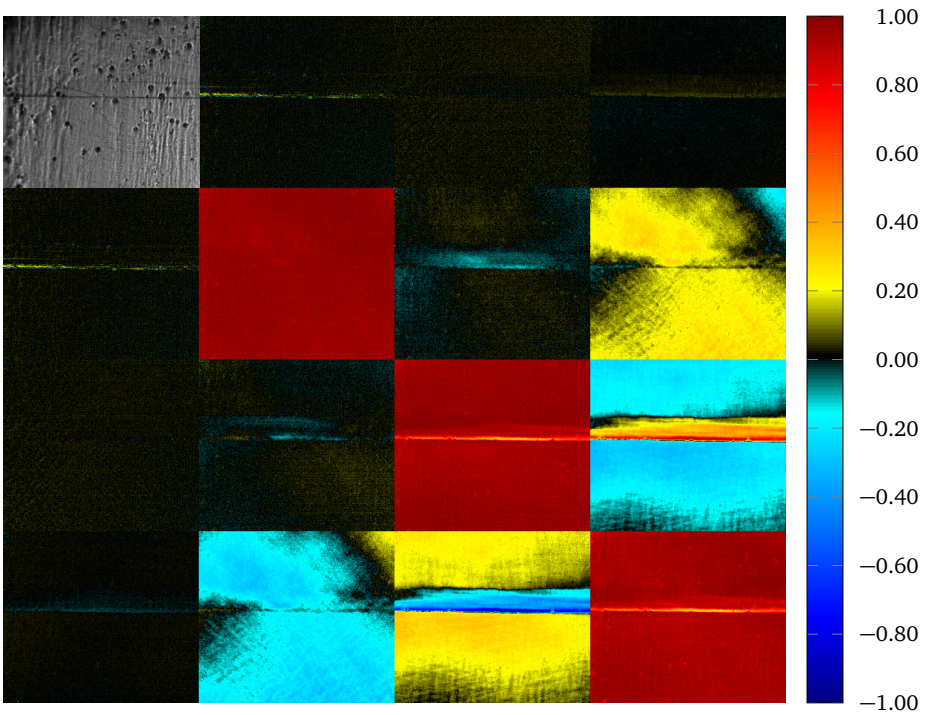

Figure 6.3: Calculated Mueller matrix **M** from intensity measurement **B** of the Σ27a-cut. The image is normalised with respect to the m_{11} element. The intensity image is overlaid the m_{11}-element as this would otherwise be unity. The colour scale is modified to enhance values around 0.

In both samples, the upper and lower part of the image are of different grains, the horizontal bisector of the image is the grain boundary interface which is of interest in these measurements. The image resolution was found to be 28 µm, and the size of each pixel to be 25 µm × 25 µm (cf. section 5.4.1).

The samples were also studied using light microscopy after being etched with Sopori etchant[114] to observe defect patterns as shown in figures 6.7 and 6.10.

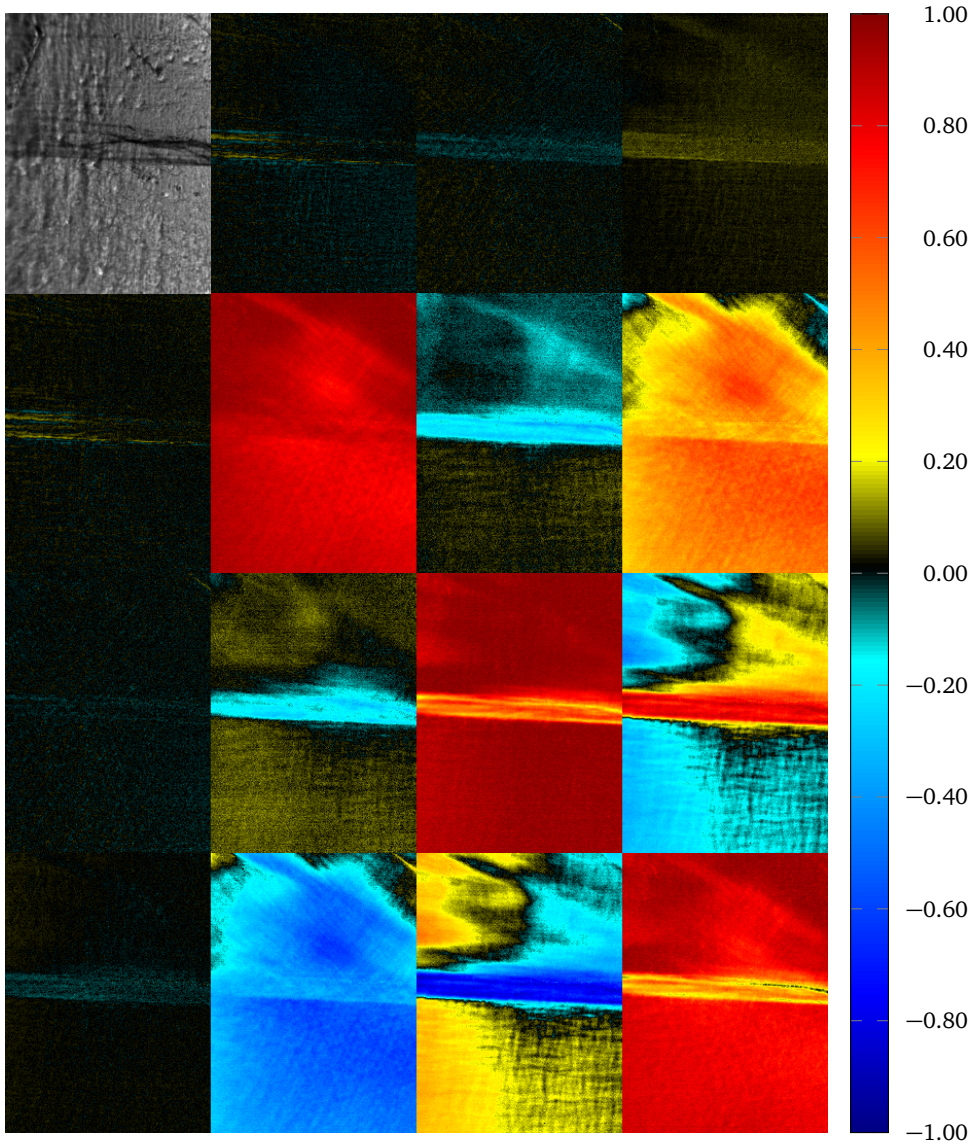

Figure 6.4: Calculated Mueller matrix **M** from intensity measurement **B** of the Σ9-cut. The image is normalised with respect to the m_{11} element. The intensity image is overlaid the m_{11}-element as this would otherwise be unity. The colour scale is modified to enhance values around 0.

6.1.3. Near-CSL grain boundary Σ9

Retardance and fast axis orientation

With the current configuration, retardance can only be measured projected in the $[0°, 180°\rangle$ interval. Judging by the lack of fringes, and assuming that the retardance varies continuously throughout the sample, it can be surmised that the actual retardance lies in the $[0°, 180°\rangle$ interval.

Looking at the linear retardance map of a small section of the grain boundary (fig. 6.5a), and assuming a proportional relationship between retardance and strain, it is evident that the highest stresses can be found in the grain boundary interface bisecting the image horizontally.

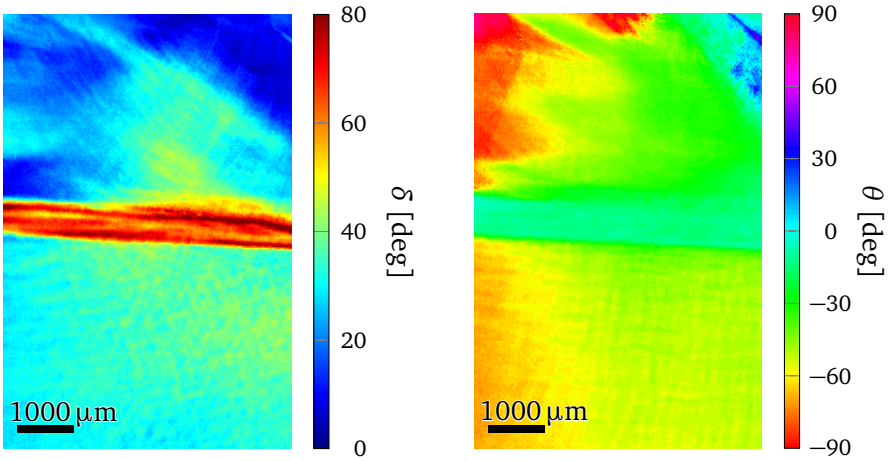

(a) Linear retardance δ. **(b)** Fast axis θ.

Figure 6.5: Maps of the linear retardance **(a)** and the corresponding fast axis orientation **(b)** for the Σ9-cut. The scales are given in degrees.

The orientation of the linear retardance gives indication as to the direction of the applied force. Tensional stresses will pull on the material, creating a lower density parallel to the direction of stress, which in turn leads to a lower refractive index in the same direction. The direction of tensile forces will therefore be indicated by the orientation of the fast axis as shown in figure 6.5b. Compressive stresses will on the other hand make the material denser in the direction of the forces, this means that the slow axis will be parallel to the stress-direction, i.e. orthogonal to the fast axis. This introduces an ambiguity as to the direction of the force.

Depolarisation

A high degree of depolarisation can suggest a rough surface. When light scatters back and forth multiple times from e.g. a rough surface, the degree of polarisation will diminish. Since the samples have been etched to reveal defect patterns, one would

assume that this will create a rough surface that depolarises the light. Looking at figure 6.6 and comparing it to the light microscopy image in figure 6.7, this appears to be the case.

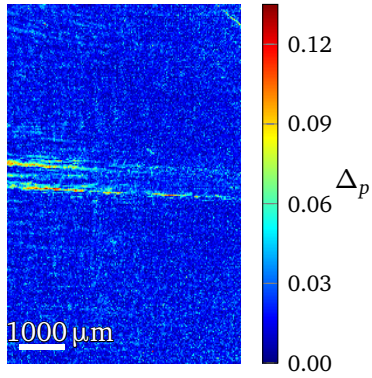

Figure 6.6: Map of the depolarisation recorded from the Σ9-cut. 0 corresponds to fully polarised light, whereas 1 correspond to fully depolarised (random) light.

Estimation of shear stress magnitude and orientation

The most interesting results are obtained when the retardance and slow axis maps are combined and compared to the light microscopy image as in figure 6.7. The retardance and slow axis map is a stitching of three different images. The images presented earlier is the middle portion of this patchwork.

Looking at figure 6.7, it is evident that both dislocation emission and strain develops preferentially in one grain. This is due to the anisotropical mechanical properties of crystalline silicon, and the fact that dislocations are generated in the grain where the shear stresses developing in the {111} planes are the highest, since these planes are the most densely packed planes in the Si diamond cubic lattice.[37] The orientation of the slow axis suggest either compressive forces between the two grains, or tensile stresses along the grain boundary.

The magnitude of these stresses can be estimated by using the linear relationship obtained between the birefringence and shear stress obtained in section 2.7.2. For a crystal silicon wafer of thickness $d = 2\,\text{mm}$, using light with a wavelength of $\lambda = 1300\,\text{nm}$ and finding the refractive index of crystal Si at this wavelength to be $n_0 = 3.50$,[115] the proportionality coefficient is found to be $\mathscr{H} \simeq 2.44\,\text{MPa rad}^{-1}$, which gives a rough estimate of the shear stress to be around 3 MPa to 5 MPa at the grain boundary interface. It should be noted that the model used is a simplification, but the answer should nevertheless give a ballpark estimate of the real shear stresses.

The obtained shear stress is a factor of 10 lower than what Varin et al.[103] reported to be enough shear stress to start plastic deformation. Dislocation emission is observed in the sample, it is therefore proposed that dislocation generation relieves tensile stress in the wafer.

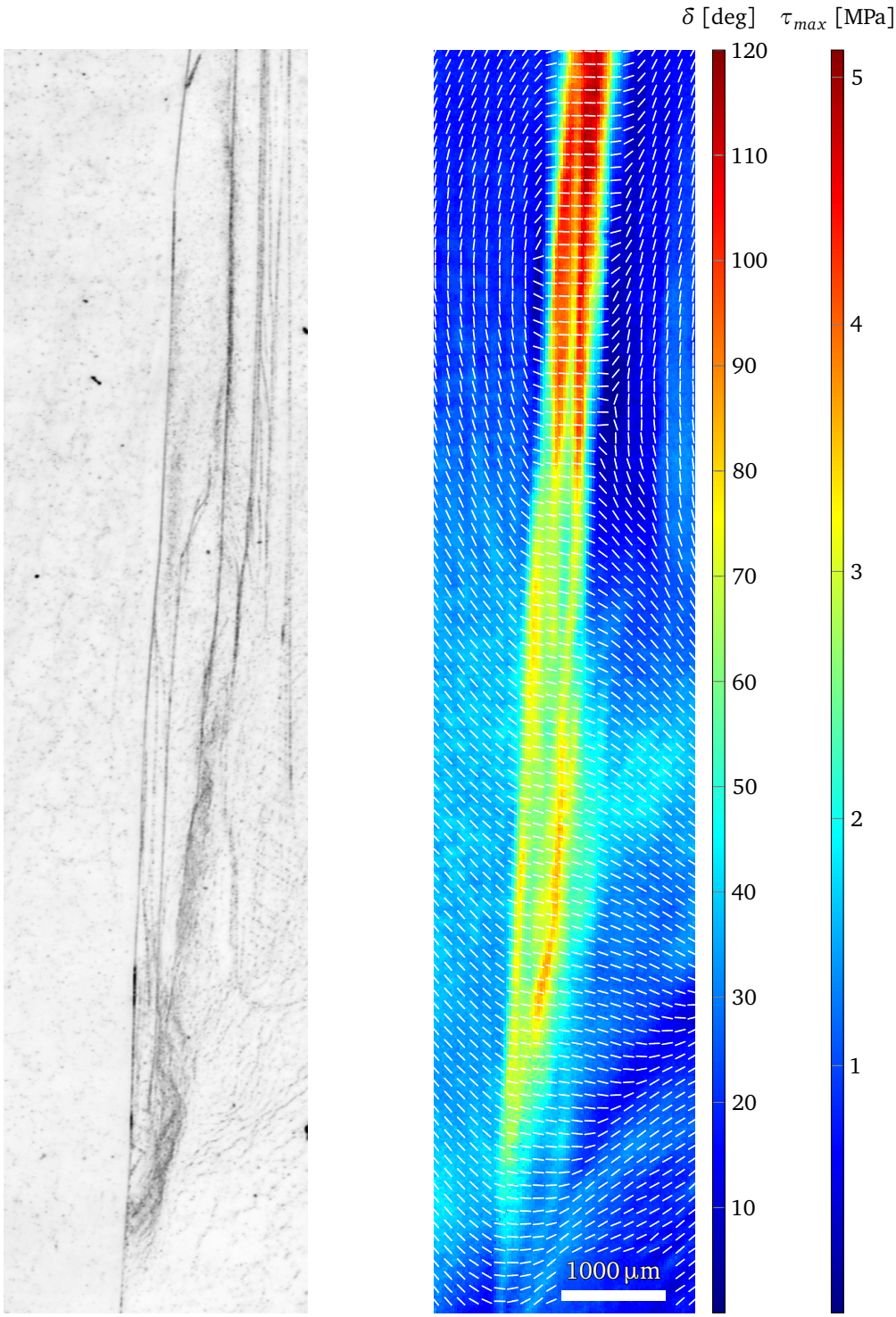

Figure 6.7: Dislocation development pattern revealed by Sopori etchant[110] (left) compared with the retardance map (right) of the Σ9-cut with the in-plane orientation of the slow axis overlaid as a quiver plot, also note that the plots are rotated such that the grain boundary is vertical.

6.1.4. Near-CSL grain boundary $\Sigma 27a$

Retardance and fast axis orientation

As in the $\Sigma 9$ cut, the highest phase shifts of the $\Sigma 27a$ cut are found in the grain boundary interface which bisects the image horizontally. More pronounced change in the fast axis is present in the $\Sigma 27a$ cut than in the $\Sigma 9$ cut as show in figure 6.8b. The most abrupt change in fast axis can be found going from the bottom seed into the grain boundary, this transition is also accompanied by the highest retardance. The fast axis undergoes a more gradual change in orientation going from the top grain into the grain boundary interface, which is believed to be due to plastic deformation taking place in the topmost grain.

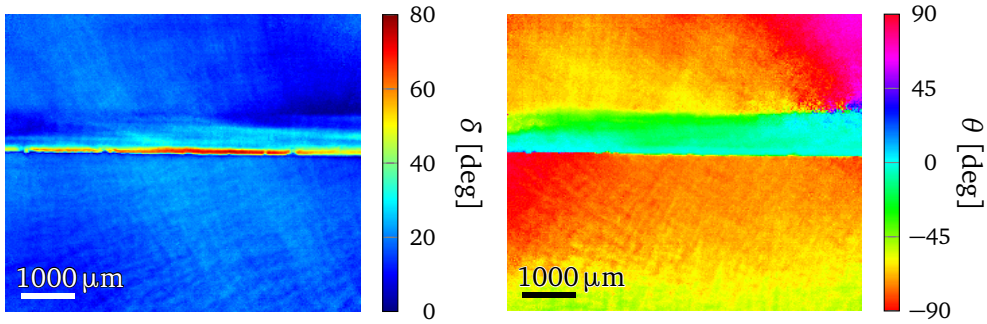

(a) Linear retardance δ. **(b)** Fast axis θ.

Figure 6.8: Maps of the linear retardance **(a)** and the corresponding fast axis orientation **(b)** for the $\Sigma 27a$-cut. The scales are given in degrees.

Depolarisation

A relatively high degree of depolarisation is observed at the grain boundary interface (fig. 6.9), which may come from the rough surface created by the Sopori etchant, indicating a high concentration of defects.

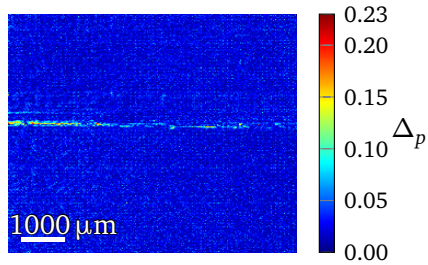

Figure 6.9: Map of the depolarisation recorded from the $\Sigma 27a$-cut. 0 corresponds to fully polarised light, whereas 1 correspond to fully depolarised (random) light.

Estimation of shear stress magnitude and orientation

By studying the light microscopy image in 6.10, it appears that the dislocation emission primarily takes place in only one of the grains, same as with the Σ9 cut. Comparing the light microscopy image to the map of the retardance with the slow axis overlaid, it is evident that most of the strain is concentrated at the side of the grain boundary which is prone to dislocation emission. As in the Σ9 cut, the slow axis suggest either compressive forces between the grains, or tensile forces along the grain boundary.

The thickness, refractive index and probing wavelength for the Σ9 sample is similar to the Σ27*a*, yielding the same proportionality coefficient of $\mathscr{H} \simeq 2.44\,\mathrm{MPa\,rad^{-1}}$. This results in the estimated maximum shear stress along the grain boundary to lie in the range 2.5 MPa to 3.5 MPa using equation (2.46).

6.1.5. Conclusion

MMI measurements of two silicon bi-crystals were carried out. Optical properties including birefringence, fast-axis orientation and depolarisation were extracted from the images using the forward polar decomposition. The analysis was mainly focused on Σ9 and Σ27*a* near-coincident site lattice grain boundaries.

Studying Sopori etched light microscopy images of the grain boundaries, it was found that dislocations preferentially develops in one of the grains, with little to no dislocation generation observed in the other grain, in correspondence with previous reports.[101,107] Comparing the Sopori etched images with the retardance (birefringence) maps of the samples revealed a high retardance coinciding with the dislocations. It is assumed that the expressed birefringence is induced by shear-stresses between the two grains, which indicate that the same grain that is prone to dislocations also experience the bulk of the stresses.

A crude 2-dimensional model was developed and employed in order to estimate the residual stresses in the samples. It is believed that the model is good enough to give an indication of the magnitude of the stresses, although more experiments are necessary in order to validate the accuracy and correctness of the model. A replication of the experiment conducted by He, et al.[38] is suggested for this purpose.

The developed model also suggest a way of using the slow-axis orientation of the birefringence to deduce the nature of the strain inducing forces. From the slow-axis orientation in both measurements it was inferred that there are either compressive forces between the grains, or tensile forces along the grain boundary.

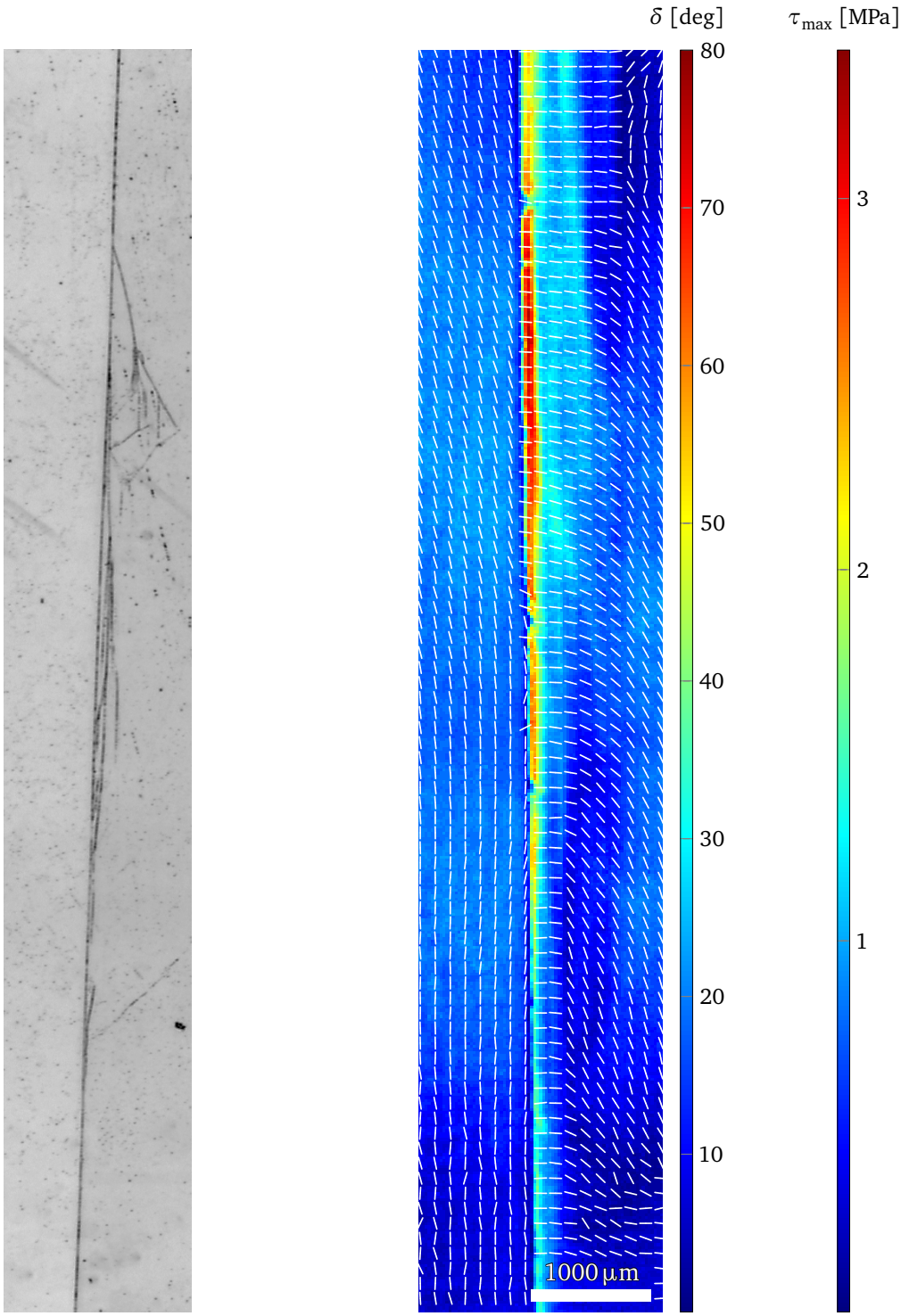

Figure 6.10: Dislocation development pattern revealed by Sopori etchant (left) compared with the retardance map (right) of the $\Sigma 27a$-cut with the in-plane orientation of the slow axis overlaid as a quiver plot, also note that the plots are rotated such that the grain boundary is vertical.

6.2. 3-D Visualisation of collagen fibres

By imaging the sample using different angles of incidence, it is possible calculate the 3-D direction of the fibres as outlined in section 4.5. This is done by comparing the slow axis found from the decomposition of the different Mueller images. The differential decomposition (see section 4.3) was chosen for this sample as the polarising and depolarising effects are assumed to happen simultaneously.

Directional analysis was done using incidence angles $\alpha_r = \pm 30°$. The full Mueller matrices are re-sampled using the incidence angle α_r to counteract stretching due to rotation such that the pixels represents a square on the actual sample (see figure 6.11).

The method is validated by comparing the results obtained from the 3-D direction calculation derived from the MMI measurements, with *Second Harmonic Generation* (SHG) images of the same sample. SHG imaging is known to be a good optical technique with diffraction limited resolution for imaging collagen fibres.[116,117]

The results presented in this section are published by P. G. Ellingsen, L. M. S. Aas, V. S. Hagen, R. Kumar, M. B. Lilledahl and M. Kildemo in the Journal of Biomedical Optics.[85] The author contributed with the MMI measurements.

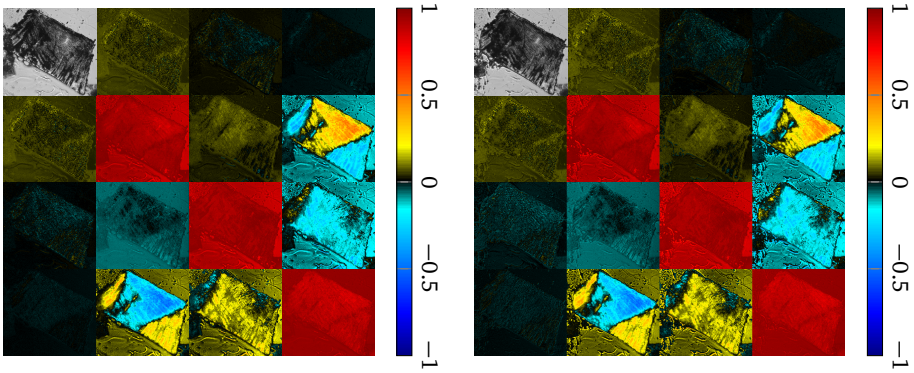

(a) −30°. **(b)** +30°.

Figure 6.11: Normalised, cropped, and resampled MMI for +30° **(a)** and −30° **(b)** angle of incidence. The intensity image is overlaid the 11 element of the Mueller matrix as this would otherwise be 1.

6.2.1. Sample preparation

Tendon tissue was taken from medial femoral condyle of a chicken's knee, bought fresh from the local supermarket. A small section of the tissue was embedded in a mounting medium for cryo-sectioning (O.C.T., Sakura, Alphen aan den Rijn, The Netherlands). The O.C.T. embedded tissue was rapidly frozen using liquid nitrogen. The frozen section was stored in a freezer at −60 °C until it was cut parallel to the collagen fibres into 50 µm thin tissue sections using a cryostat. The sections were

then placed on standard microscope glass-slides and stored in a freezer at −60 °C. Before being measured, the tissue samples were brought back to room temperature and covered with a standard cover slip. The edges of the cover slip were sealed using Vaseline to avoid dehydration. Between measurements the slides were stored at 4 °C.

6.2.2. Measurements

The presented SHG images were obtained with a *Zeiss* LSM 510 meta microscope using a Coherent Mire 900 for excitation at 790 nm. Imaging was done with a 40 × 1.2 NA objective. A custom-built polarisation set-up, which compensates for any birefringence in the optical path, was used to ensure circular polarisation.[85] The average power at the focal plane was approximately 8.

After imaging the samples using SHG, they were measured using the custom built MMI described in chapter 5 using the Lumenera camera and the 940 nm light source. The sample was imaged at incidence angles 0°, and ±30°.

6.2.3. Results

Linear retardance and depolarisation

Figure 6.12 shows the linear retardance and its uncertainty calculated from the $\mathbf{L}_m$ and $\mathbf{L}_u$ matrices. A high concentration of collagen will result in a significant retardance due to form birefringence, which is induced by the anisotropic characteristics of the fibres.[97]

As there is a high degree of order in the tendon samples it can be considered as only mono-layered, avoiding a more complex multi-layered model.[85] The uncertainty map of the linear retardance in figure 6.12b indicate uncertainty above the random noise level, as seen from the calibration of a few percent (cf. the $\mathbf{M}_0$ element in figure 5.11). The uncertainty depicted in figure 6.12b is a result of depolarisation effects, i.e. it gives a measure for the ambiguity induced by randomness of the sample. This randomness can be caused by e.g. fibre orientation or size, multiple scattering, or integration over several polarisation states in one pixel. This is further confirmed by comparing the uncertainty measurement to the depolarisation shown in figure 6.13a.

Directional imaging

From the decomposition of the measurements, it is possible to also calculate the direction of the fast axis of the birefringence. Together with the correct effective medium model, this property can be used to find the 3-dimensional direction of the collagen fibres as explained in section 4.5. The calculated 3-D directional image can be seen i figure 6.14, where the in-plane direction is illustrated with black lines and the out-of-plane direction is indicated by the colour with a key in the lower left corner.

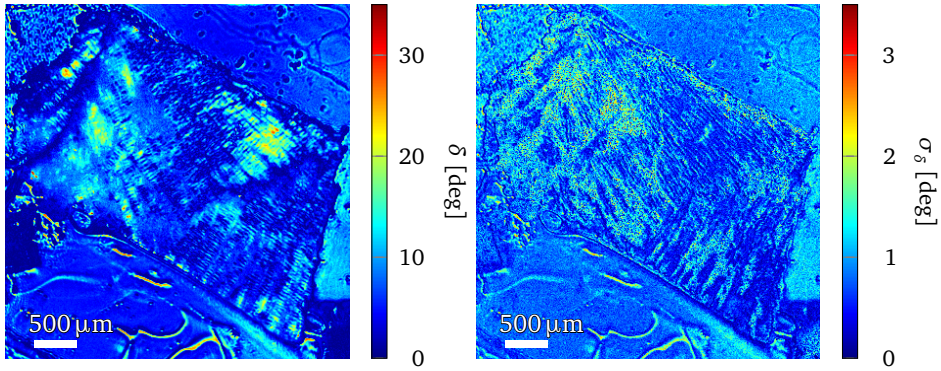

(a) Linear retardance δ. **(b)** Uncertainty σ_δ.

Figure 6.12: Images of the linear retardance **(a)** and the uncertainty **(b)** of the tendon sample at normal incidence. The colour scale is given in degrees.

The uncertainty of the fast-axis orientation is presented in figure 6.13b. This uncertainty is calculated using equation (4.42), at an incidence angle of 0°. The reason for choosing to study the uncertainty at an incidence angle of 0°, instead of ±30°, is due to the approximations used to derive the propagation of uncertainty.[85] Since propagation of uncertainties only make use of the first derivatives, and not higher orders, this might be an incorrect approximation for equation (4.53), which is used to derive the out of plane orientation. The uncertainty at 0° and ±30° is expected to be similar, although an exact relation is hard to predict. This relation is hard to predict since an increase in the number of data points could reduce the uncertainty, while on the other hand, and increase in apparent thickness may increase the uncertainty.

Comparing the directional image in figure 6.14, and the SHG image shown in figure 6.15a, shows that the fibres are mostly in-plane, as expected due to the direction of the cryostat cut. The calculated in-plane directions (black lines in figure 6.14 and 6.16b) appear to correspond well with the apparent directions in the SHG image viewed in figure 6.15 and 6.16a. Some fibres are clearly out-of-plane, indicated by red areas in the 3-D directional image (fig. 6.14), which in the SHG image (fig. 6.15a) show up as dark spots, or show some weak structure. The absence of signal in the SHG image can be explained by considering SHG signal generation, in which fibre orientation is important. An in-plane fibre will have a much larger cross-section for generating SHG signals, as compared to an out-of-plane fibre. This means that the darker parts of figure 6.15a are most probably due to out-of-plane oriented fibres, in accordance to the 3-D directional image. Figure 6.15b shows the SHG image overlaid the out-of-plane calculated direction, where blue represent towards the reader and green away from the reader.

As mentioned, the out-of-plane directions in 6.14 are seen to correspond well with the same areas in the SHG image. Additionally, by studying close-ups of the SHG and directional image as shown in figure 6.16, it is possible to see that the oscillating

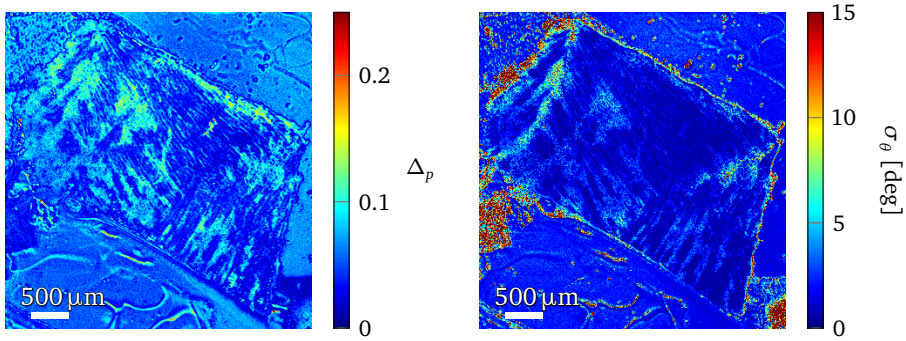

(a) Depolarisation Δ_p. **(b)** Slow axis uncertainty σ_θ.

Figure 6.13: Depolarisation at normal incidence for the sample (a). The scale goes from 0 for fully polarised to 1 for fully depolarised. The uncertainty in the direction of the slow axis for normal incidence is show in (b). This calculation is based on equation (4.42). The colour scale is in degrees.

structure along the fibres is visible in both the SHG image (fig. 6.16a) and the out-of plane direction image (fig. 6.16b, blue-green oscillations). These results give a strong indication that the 3-D directional imaging delivers the correct directions.

6.2.4. Conclusion

A method for determining the 3-D direction of collagen fibres embedded in biological tissue, specifically tendon, using Mueller matrix ellipsometry imaging was presented. The results are shown to good be in agreement when compared to the second harmonic generation images of the same sample. In particular, the presented method is capable of depicting oscillating structures in the collagen orientation, as well as the out-of-plane direction of the fibres.

The possibility of imaging effects from collagen fibres below the diffraction limit could be important input to understanding the collagen framework. Additionally, the implementation and use of the differential decomposition instead of the, until now, most common polar decomposition has provided extra insight into the uncertainties of the calculated physical properties.

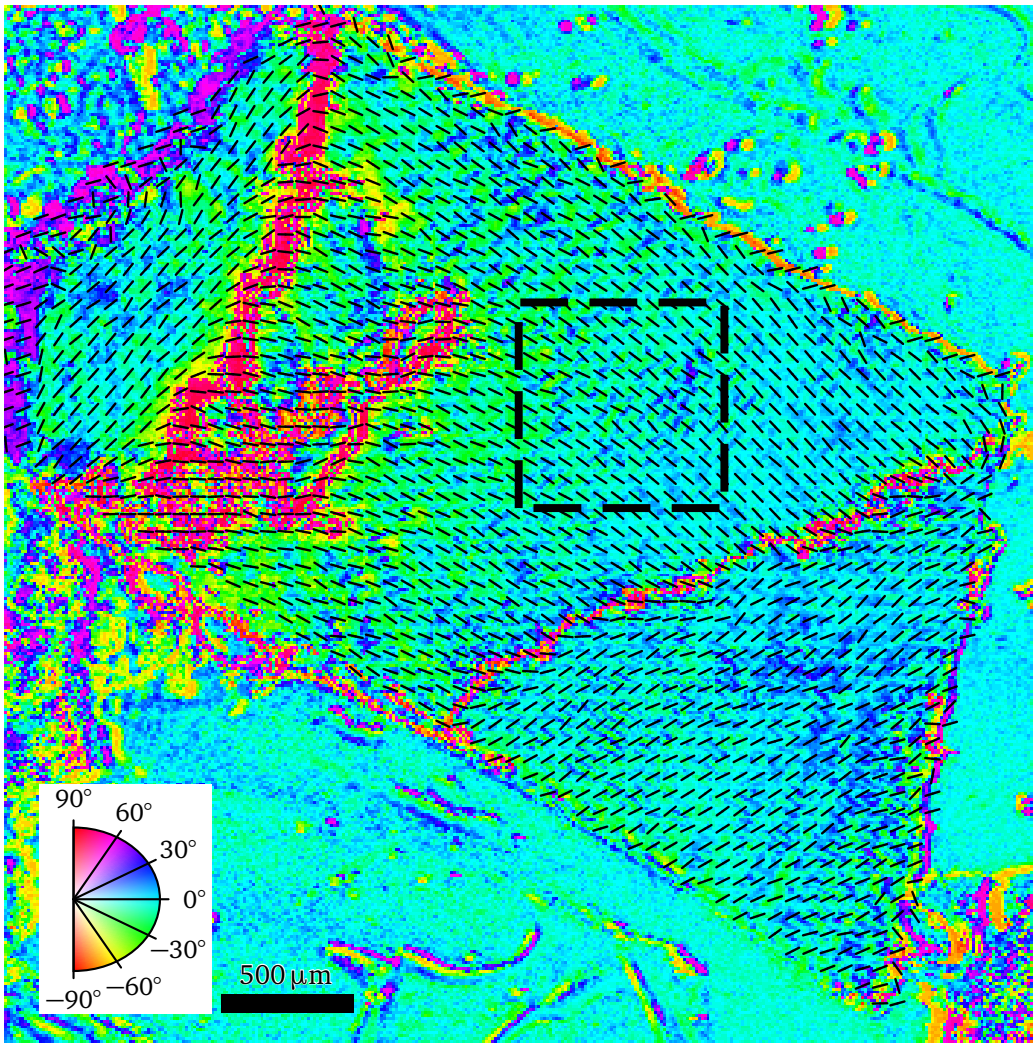

Figure 6.14: 3-D directional image of the tendon sample. The out-of-plane direction is indicated by the colours as indicated by the half-wheel in the lower left corner. The image plane is indicated by 0°, while 90° is directly towards the reader, and −90° away from the reader. The in-plane direction is shown by the quiver plot overlaid the sample. The dashed square is magnified in figure 6.16b. Image replicated from article.[85]

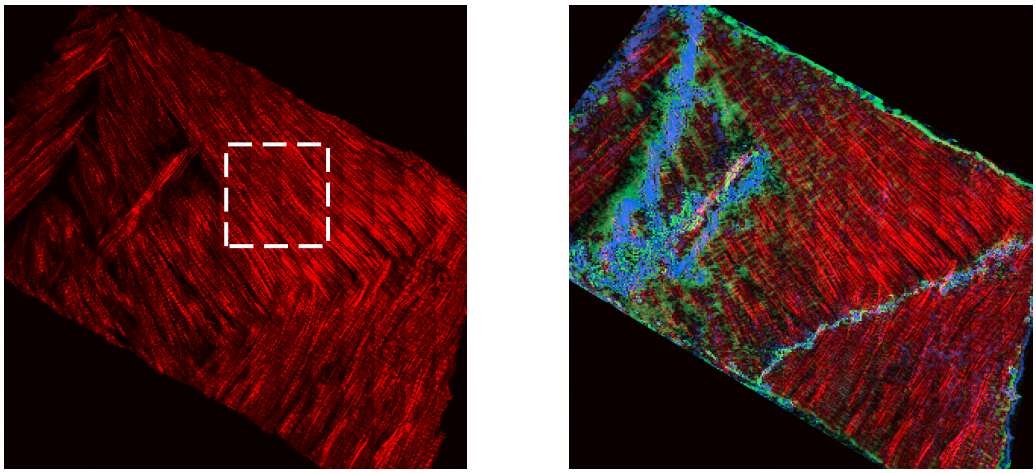

(a) SHG image **(b)** Out-of-plane

Figure 6.15: (a) A Second Harmonic Generation (SHG) image of the sample. The white dashed square indicates the location of the magnified view in 6.16a.
(b) The out-of-plane direction is overlaid the SHG image. The blue colour represents positive out-of-plane direction, while the green colour represents negative direction. The opacity of the blue and green colours represents the amount of out-of-plane direction; no colour being in plane, and full colour being perpendicular to the image plane. Images replicated from article.[85]

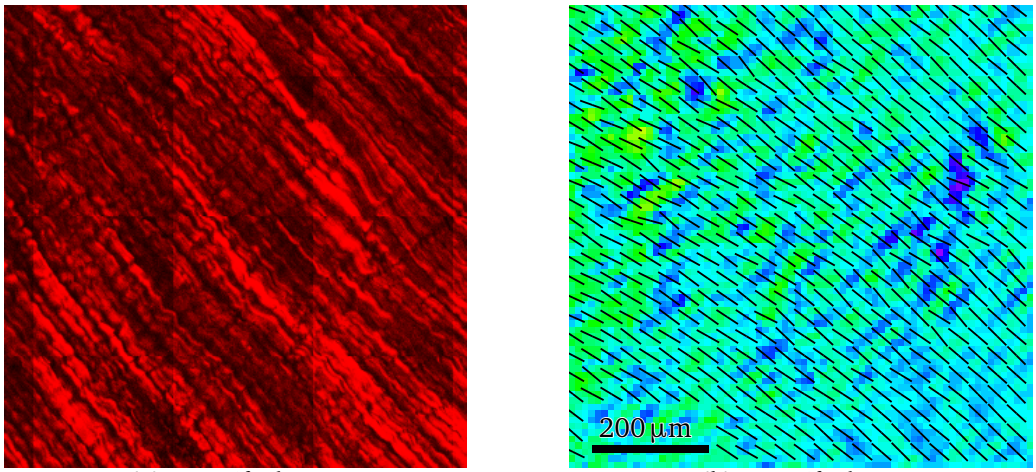

(a) Magnified SHG **(b)** Magnified 3-D

Figure 6.16: Magnified view of the SHG image (a) (from fig. 6.15), and the 3-D directional image (a) (from fig. 6.14). Refer to figure 6.14 for the colour scale. Images replicated from article.[85]

Part III.

Development of a Spectroscopic Mueller Matrix Imaging Microscope

CHAPTER 7

Development

A compact Mueller matrix microscopy imaging system was designed and built as a part of this thesis. The basic design borrows from the Mueller matrix ellipsometer (MME) proposed by Gandorfer[49] using ferroelectric retarders. The MME built by Ladstein et al.[52] using ferroelectric liquid crystals (FLCs) was used as a starting point. In Ladstein's design the PSG consists of a polariser followed by a fixed waveplate (WP), an FLC, a second fixed waveplate and lastly by another FLC. The PSA consists of the same components as the PSG, but in reverse order as can be seen in figure 7.1.

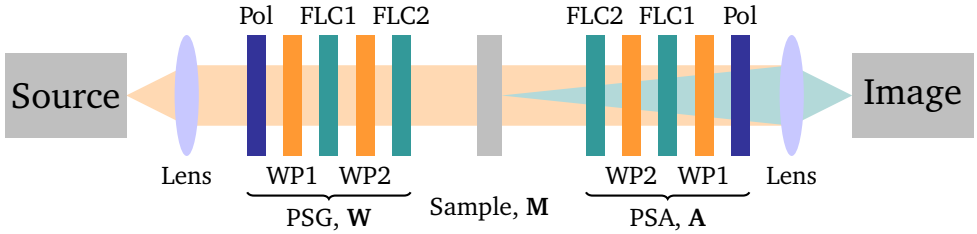

Figure 7.1: A Mueller Matrix imaging ellipsometer design proposed by Ladstein et al.[52] The polarisation state generator (PSG) consists of a polariser (Pol) followed by two fixed waveplates (WP1, WP2) and two ferroeletric liquid crystals (FLC1, FLC2). The polarisation state analyser (PSA) consists of the same components as the PSG, only in reverse.

7.1. Preliminary design

There is no clear cut approach to designing an optimal spectroscopic MMI device, and many different designs have been reported in literature.[43–56] The design proposed in this thesis is based on the PSG consisting of two fixed quartz waveplates (WPs) and two FLCs with the ability to switch between two orientations by use of electricity. Experimental data obtained by Ladstein[90] for his Master's thesis (table 7.1), where retardance measurements for an FLC and a WP was fitted to the Sellmeier equation[91]

to model the components. A genetic algorithm developed by Letnes et al.[59] was utilised to breed forth an optimal design for a spectroscopic MMI in the range 550 nm to 1150 nm. This range was chosen since the transmission ratio of biological tissue is relatively high in this region.[118] The thickness and orientation of the components were used as genes in the genetic algorithm, with the thickness assumed to give the retardance of the components by the Sellmeier equations,

$$\delta_{FLC}(\lambda, L) = \frac{2\pi A_{\mathrm{UV}}}{\sqrt{\lambda^2 - \lambda_{\mathrm{UV}}^2}} \cdot L, \tag{7.1a}$$

and

$$\delta_{WP}(\lambda, L) = \left[\frac{2\pi A_{\mathrm{UV}}}{\sqrt{\lambda^2 - \lambda_{\mathrm{UV}}^2}} - \frac{2\pi A_{\mathrm{IR}}}{\sqrt{\lambda_{\mathrm{IR}}^2 - \lambda^2}} \right] \cdot L, \tag{7.1b}$$

where δ_{FLC} and δ_{WP} is the retardance of the FLCs and WPs respectively. The constants A_{UV}, A_{IR}, λ_{UV} and λ_{IR} are fit parameters to the Sellmeier equation with values given in table 7.1. The variable λ is the wavelength in nm, whereas the variable L is seen as the thickness of the component acting as a scaling of the retardance.

Table 7.1: Fit values for a ferroelectric liquid crystal (FLC) and a quartz waveplate (WP) obtained by Ladstein[90] for the Sellmeier equation.

Component	A_{UV} [nm]	λ_{UV} [nm]	A_{IR} [nm]	λ_{UV} [µm]
FLC	202	280	N/A	N/A
WP	110	134	50	11.16

As a goodness-of-fit parameter, the condition number of the modulation matrix $\kappa_W = \mathrm{cond}(\mathbf{W})$, which has a theoretical minimum of $\sqrt{3}$,[67] was used. Not all the offspring generated by the genetic algorithm were realisable as manufacturers could not produce the components needed to build the design (see appendix F). The most promising and physically realisable child of the genetic algorithm was selected for further study (fig. 7.2). The component parameters needed to complete the design is listed in table 7.2, with the resulting retardance of each component graphed in figure 7.3.

After having decided on components for the PSG and PSA, suitable calibration samples had to be found. Compain et al.[63] proposes that the calibration is most accurate when the ratio of the eigenvalues

$$\epsilon = \frac{\lambda_{15}}{\lambda_1} \tag{7.2}$$

of the **K** matrix is maximum (cf. section 3.2.1). It has earlier been reported[119] that for a set of reference samples consisting of two polarisers and a linear retarder, the optimum values are 0° and 90° for the polarisers, and 30.5° or 59.5° orientation for a

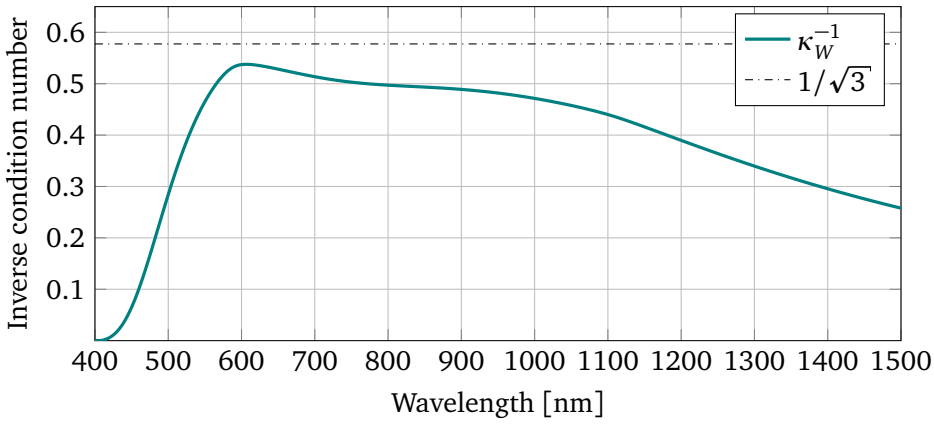

Figure 7.2: Inverse condition number of the modulation matrix $\kappa_W^{-1} = \text{cond}(\mathbf{W})$ of the most promising and physically realisable child of the genetic algorithm. The inverse condition number of the analyser matrix (κ_A^{-1}) is the same as the modulation matrix. The theoretical maximum for the inverse condition number of the modulation matrix is $1/\sqrt{3}$.[67]

Table 7.2: Values for the thickness and angle for the best child of the genetic algorithm. The note is at what wavelength the component acts as either a half waveplate ($\lambda/2$) or a quarter waveplate ($\lambda/4$). The calculated retardance for the components using eq. (7.1) is plotted in fig. 7.3.

Component	Thickness	Angle [°]	Note
FLC1	1.348	142.3	$\lambda/2$ @ 610 nm
FLC2	1.459	72.7	$\lambda/2$ @ 650 nm
WP1	1.439	73.7	$\lambda/4$ @ 630 nm
WP2	1.585	8.6	$\lambda/4$ @ 690 nm

linear retarder with a constant phase change of 109° with respect to the first polariser. A linear retarder with constant retardance over a broad wavelength-range is hard and expensive to manufacture, it was therefore chosen to use a quarter waveplate which have proven to work satisfactory in other setups.[90]

Simulations using two polarisers with one oriented at 0° by definition and the other at 90°, and a slew of different waveplates with different orientations using equation (7.1a) with constants from table 7.1 as a model, was done in order to determine a WP to adequately act as a calibration sample over the design-range. It was found that the optimal choice of a WP depended heavily on wavelength, which made selecting an optimal WP in the range 550 nm to 1150 nm difficult. A quartz crystal acting as a quarter-waveplate at 910 nm rotated to 55° was found to be a good candidate as a calibration sample.

7.2. Realisation

Looking at the results obtained in the preliminary design, the items listed in table 7.3 was procured from different manufacturers. In order to easily align the components, a special holder had to be designed. The schematics for the PSG and PSA was created using SolidWorks 2013, and can be found in appendix G. After the holders were built in-house at *Finmekanisk Verksted*, *Glassblåserverkstedet* helped glue the waveplates and polarisers in place using a silicone adhesive.

Table 7.3: List of equipment procured in order to complete the new Mueller matrix imaging microscope.

Units	Component	Manufacturer	Manufacturer description
2	Ferroeletric liquid crystal	CITIZEN FINETECH MIYOTA	FLC Polar Rotator @610nm+/-50nm with housing Model Number: LV2500-OEM
2	Ferroeletric liquid crystal	CITIZEN FINETECH MIYOTA	FLC Polar Rotator @650nm+/-50nm with housing Model Number: LV2500-OEM
2	Quarter waveplate	CASIX	L/4 Cemented zero order WP dia 25.4mm, with AR/AR@630nm, Unmounted
2	Quarter waveplate	CASIX	L/4 Cemented zero order WP dia 25.4mm, with AR/AR@690nm, Unmounted
1	Quarter waveplate	CASIX	L/4 Cemented zero order WP dia 25.4mm, with AR/AR@910nm, Unmounted
4	Linear polariser	CODIXX	Unmounted colorPol® VISIR, diameter 25.0 mm, laminated, ground and polished

7.2.1. Characterisation and design optimisation

The retardance of the WPs and FLCs were characterised using the commercially available RC2 ellipsometer from *J.A. Woollam Co., Inc.* The measured retardance is graphed over the theoretical in figure 7.3. Note that each component come in a pair. All measurements were done in transmission using a high-pass filter with a cut-off wavelength at 450 nm in front of the source to avoid possible UV damage to the components, especially the FLCs. The change in azimuthal angle for the FLCs when applying voltage were measured to be 45.8° and 46.3° for FLC1 (HWP @ 610 nm) and FLC2 (HWP @ 650 nm), respectively. Using the mean measured retardance for each component, the system angles were optimised by searching for a local minima of the condition

number as a function of the azimuthal angle of the components. The `fminunc` function in the Optimization Toolbox for MATLAB 2014a was used for this purpose. As can be seen from figure 7.4, the new design has a better inverse condition number in the 650 nm to 950 nm range, while a slightly worse inverse condition number above 950 nm compared to the initial design.

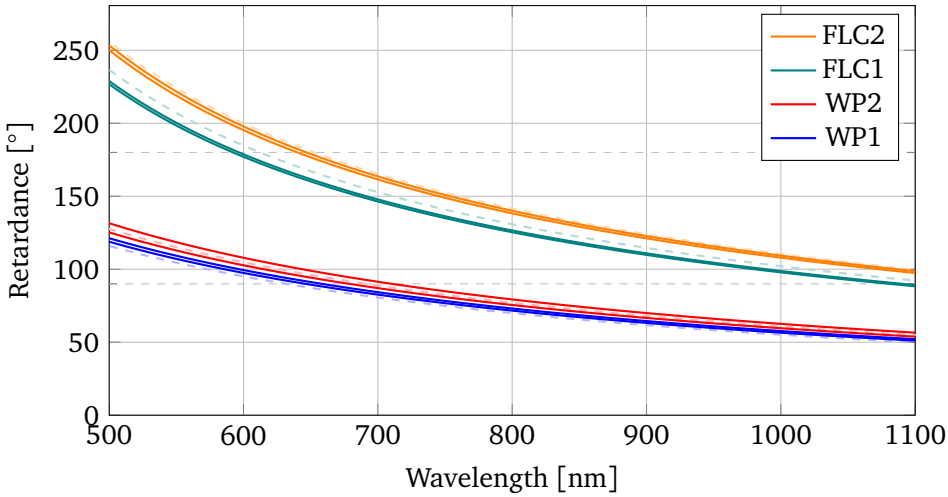

Figure 7.3: Measured retardance of the components (solid line) compared to the retardance given by the initial design (dashed line). Note that each component come in a pair.

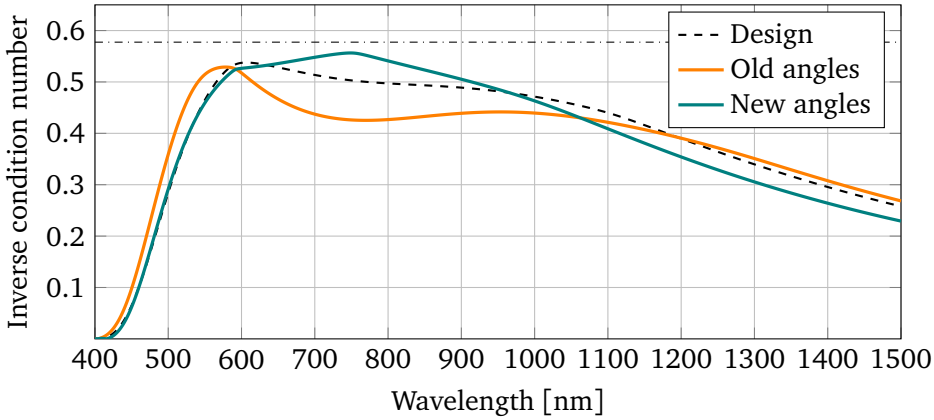

Figure 7.4: The inverse condition number for the initial design, the original angles with the measured components, and the new angles.

Sensitivity to azimuthal rotation misalignment was studied by letting each component, except the polariser, be misaligned by 1° in discrete steps. The results for an allowed misalignment of each component by ±1° (fig. 7.5) and ±2° (fig. 7.6) show that the system is acceptable to within ±1° misalignment.

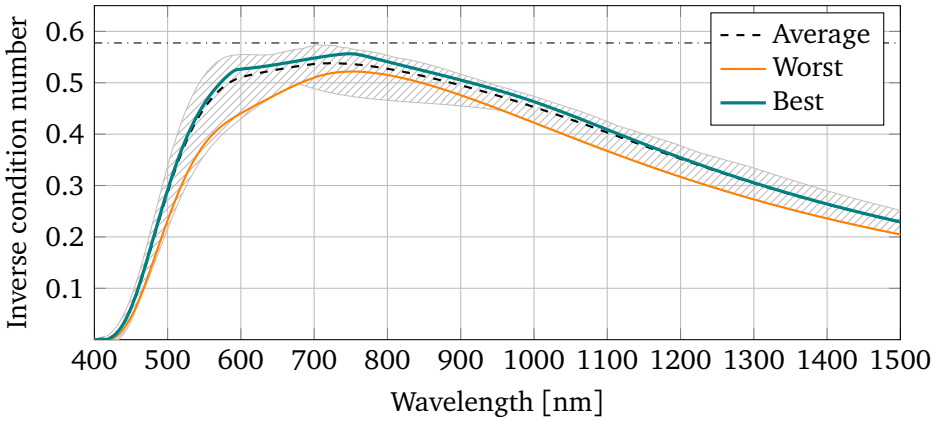

Figure 7.5: Misalignment of the WPs and FLCs up to ±1° in discrete 1° steps. The hatched area contain the maximum and minimum inverse condition number, while the orange line represents the worst possible combination. The dashed line gives the average inverse condition number for the $3^4 = 81$ possible combinations. The best combination is indicated by the teal line.

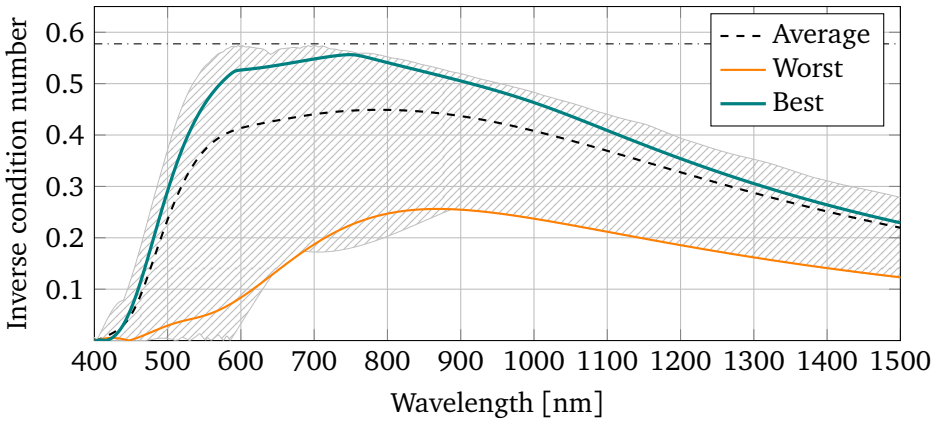

Figure 7.6: Misalignment of the WPs and FLCs up to ±2° in discrete 1° steps. The hatched area contain the maximum and minimum inverse condition number, while the orange line represents the worst possible combination. The dashed line gives the average inverse condition number for the $5^4 = 625$ possible combinations. The best combination is indicated by the teal line.

7.2.2. Assembly

The components were aligned using the same set-up as when characterising them. The azimuthal orientation of each component was determined by first extracting the component Mueller matrix ($\mathbf{M}_{\text{component}}$) from the measured Mueller matrix ($\mathbf{M}_{\text{measured}}$). To do this the Mueller matrix of the system excluding the component being aligned $\mathbf{M}_{\text{placed}}$, has to be invertible (in practise this means that the polariser must be aligned last). The Mueller matrix of the component is calculated as

$$\begin{aligned} \mathbf{M}_{\text{measured}} &= \mathbf{M}_{\text{component}} \cdot \mathbf{M}_{\text{placed}}, \\ \mathbf{M}_{\text{component}} &= \mathbf{M}_{\text{measured}} \cdot \mathbf{M}_{\text{placed}}^{-1}. \end{aligned} \tag{7.3}$$

A model based on a rotated perfect linear retarder (eq. (2.21)) with wavelength dependent retardance δ given by the appropriate Sellmeier function (eq. (7.1a or b))

$$\mathbf{M}_{\text{model}}(\theta, \delta(\lambda, L)) = \mathbf{R}(-\theta) \begin{bmatrix} 1 & 0 & 0 & 0 \\ 0 & 1 & 0 & 0 \\ 0 & 0 & \cos\delta(\lambda, L) & \sin\delta(\lambda, L) \\ 0 & 0 & -\sin\delta(\lambda, L) & \cos\delta(\lambda, L) \end{bmatrix} \mathbf{R}(\theta), \tag{7.4}$$

was fitted with respect to θ and L to the component Mueller matrix extracted from equation (7.3) by minimising the sum

$$\sum_{\lambda} \left| \mathbf{M}_{\text{component}} - \mathbf{M}_{\text{model}} \right|,$$

using MATLABs `fminunc` function.

Since it proved difficult to position each component with the wanted precision, the azimuthal angles of the remaining components were locally optimised after each component was put in place. The built in MATLAB function `fminunc` was used for the optimisation. The final azimuthal angles can be found in table 7.4 together with the initial angles for comparison.

Table 7.4: Initial design, optimised, and final azimuthal angles for the PSG and PSA.

	Polariser	WP1	WP2	FLC1	FLC2
Initial design	0°	73.7°	8.6°	142.3°	72.7°
New design	0°	74.0°	5.5°	137.4°	71.6°
PSG	0.15°	74.2°	0.6°	136.3°	70.3°
PSA	0.07°	73.7°	3.0°	135.8°	71.4°

After the PSG and PSA had been fully assembled, the Mueller matrix of each state was measured in order to construct the modulation matrix **W** and analyser matrix **A** as described in section 3.1. The obtained inverse condition number is plotted together with the transmission ratio in figure 7.7. The design and actual inverse condition number are in good agreement which indicate a successfully alignment of the components.

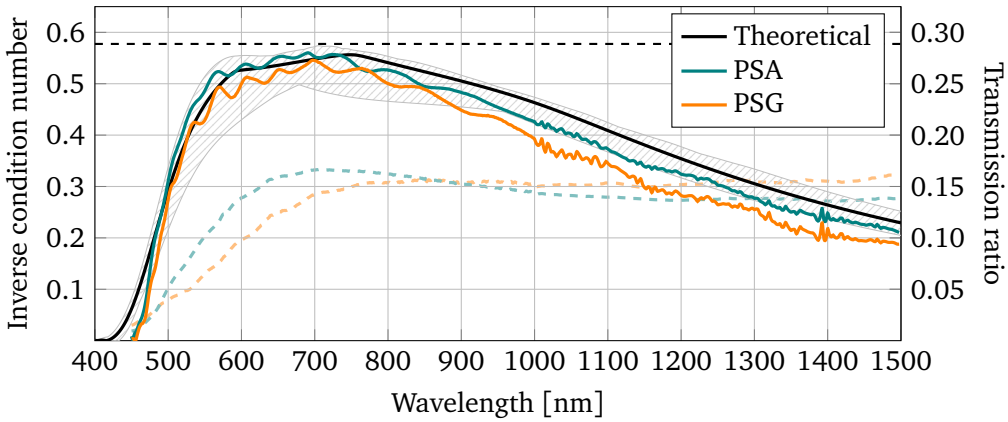

Figure 7.7: Measured inverse condition number (solid line) and transmission ratio (dashed line) for the fully assembled PSG and PSA.

The lower inverse condition number of the PSG compared to the PSA is believed to be mainly due to the slightly worse alignment of the polariser. Using current techniques a more precise alignment is tedious and the measured inverse condition numbers are deemed satisfactory. The drop in transmission at lower wavelengths is attributed to the transmission ratio of the polariser, see appendix H.

7.3. Verification

In order to verify the system, the components were installed in an old *Zeiss* Axiovert 100M microscope, as shown schematically in figure 7.8. A photograph of the assembled instrument can be found in figure 7.9. For imaging, a *Zeiss* Neofluar 10/0,30 160/- objective lens was used together with a *ThorLabs* 940 nm LED source for illumination, and a *Lumenera* Lw11059M camera for detection.

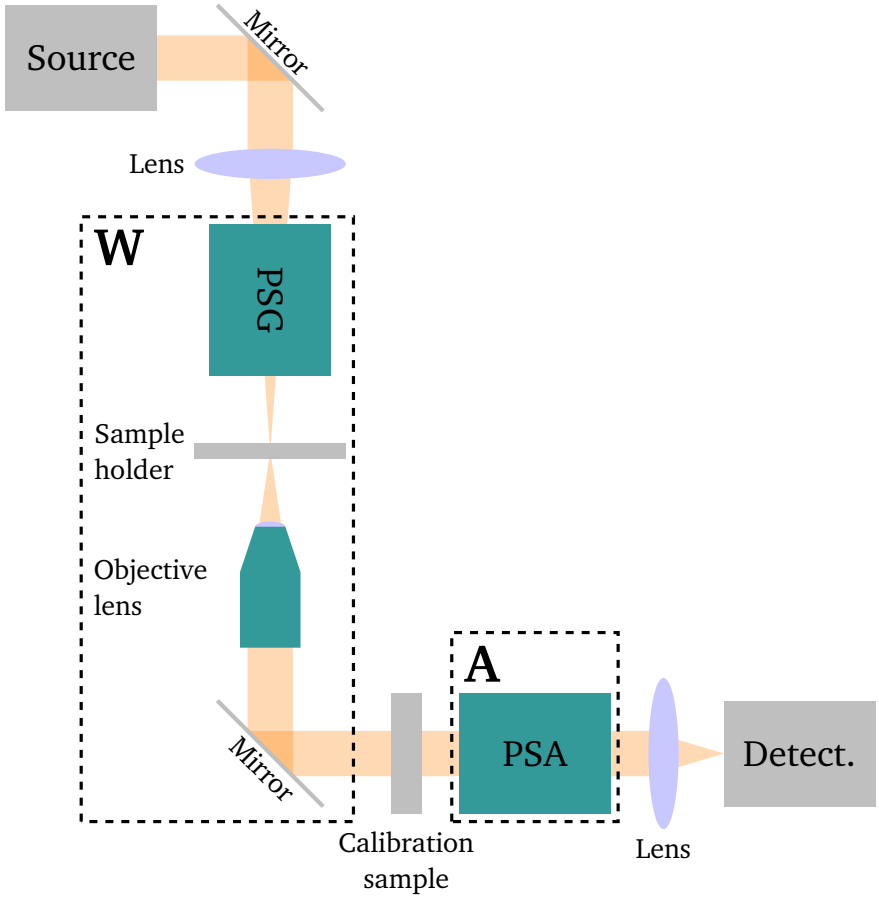

Figure 7.8: Sketch of the Mueller matrix imaging microscope (μMMI) configuration. The dashed boxes encapsulate the system matrices **W** and **A** in the case where no sample is present.

After installing the components, the system was calibrated using the ECM-algorithm (cf. sec 3.2.1) as a benchmark. Air, two *CODIXX* colorPol VISIR polarisers, one oriented at 0° and the other at approximately 90°, together with a *CASIX* cemented zero order QWP @ 910 nm oriented at approximately 55° was used as calibration samples. A histogram of the resulting inverse condition numbers for the **W** and **A** matrices can be seen in figure 7.10. The obtained results indicate that the instrument is working

Figure 7.9: Photograph of the prototype Mueller matrix imaging microscope with some parts indicated.

as intended. The relatively wider spread in the condition number of the modulation matrix **W** can be attributed to the fact that it contains the condenser lens and a mirror as well as the PSG, as illustrated in fig 7.8. Another reason for the wider spread in the condition number is contributed to the fact that the beam is less collimated when travelling through the PSG when compared to the PSA, since the lens focusing the beam is currently before the PSG. Simply moving the condenser lens, or adding additional optics to achieve Köhler illumination[120] may resolve this issue.

A second benchmark from the calibration is the ability to reconstruct the calibration samples successfully, as this will give an indication of the system's ability to correctly represent samples. The easiest calibration sample to compare with its reconstructed Mueller matrix counterpart is air, as this is represented by the identity matrix. In the used implementation of the ECM-algorithm, the first polariser is also readily compared to its reconstructed counterpart as this is modelled as a horizontal polariser, i.e. no rotational dependency. The $\mathbf{M}_0$ reconstructed sample in figure 7.11 is in good correspondence with the Mueller matrix of air within a few percent, with the exception

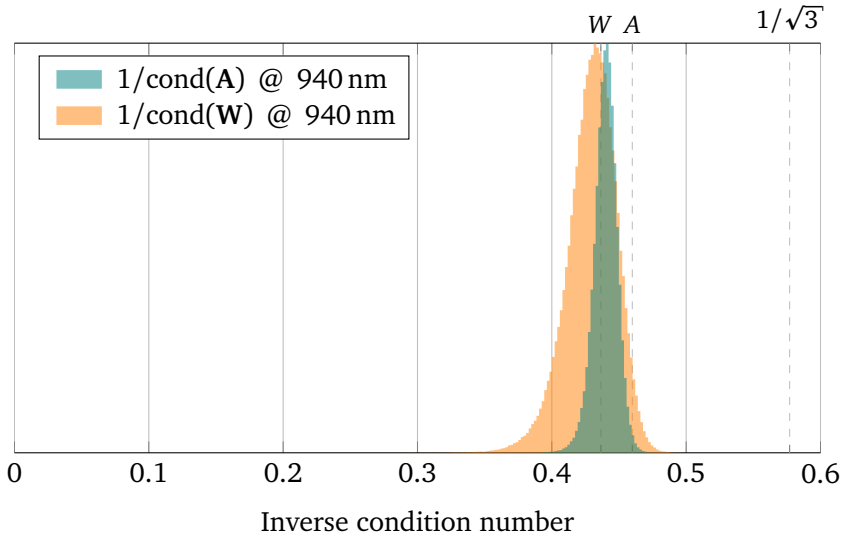

Figure 7.10: Normalised inverse condition number histograms for the PSG (**W**) and PSA (**A**) for a 640 px × 640 px crop. The dashed lines denoted W and A indicate the maximal theoretical inverse condition number for the **W** and **A** matrices at 940 nm respectively.

of the $(3,3)$ element. There is also good agreement between the $\mathbf{M}_1$ sample and the Mueller matrix of a horizontal retarder.

Interesting results can be observed in the $(3,1)$, $(3,2)$, $(1,3)$ and $(2,3)$ elements of $\mathbf{M}_2$. The values appear to fluctuate between adjacent pixels, causing a high standard deviation. These fluctuations are believed to be due to a slightly bad alignment of the calibration sample, or possibly in the angle optimisation part of the ECM-algorithm. A third explanation is random noise, a factor which may be improved by averaging over multiple images.

Lenses may alter the polarisation of the light which is believed to emerge as a radial dependency in the image. A larger crop of 1128 px × 1128 px covering most of the image revealed no apparent radial dependency in the condition number (figure 7.12), thus this concern was not further explored. The LED light source used for the measurement has a rectangular footprint which can be observed in 7.12, indicating a strong dependency on light intensity.

System resolution was also investigated by imaging a *Resolution Test Target* from *Newport* shown in figure 7.13. The pixel size was found to be 1.5 µm × 1.5 µm, while the resolution was determined to be around 2.5 µm. The Abbe resolution limit[15,121] ($d = \lambda/2NA$) with the current equipment ($NA = 0.3$, $\lambda = 940$ nm) is found to be 1.57 µm.

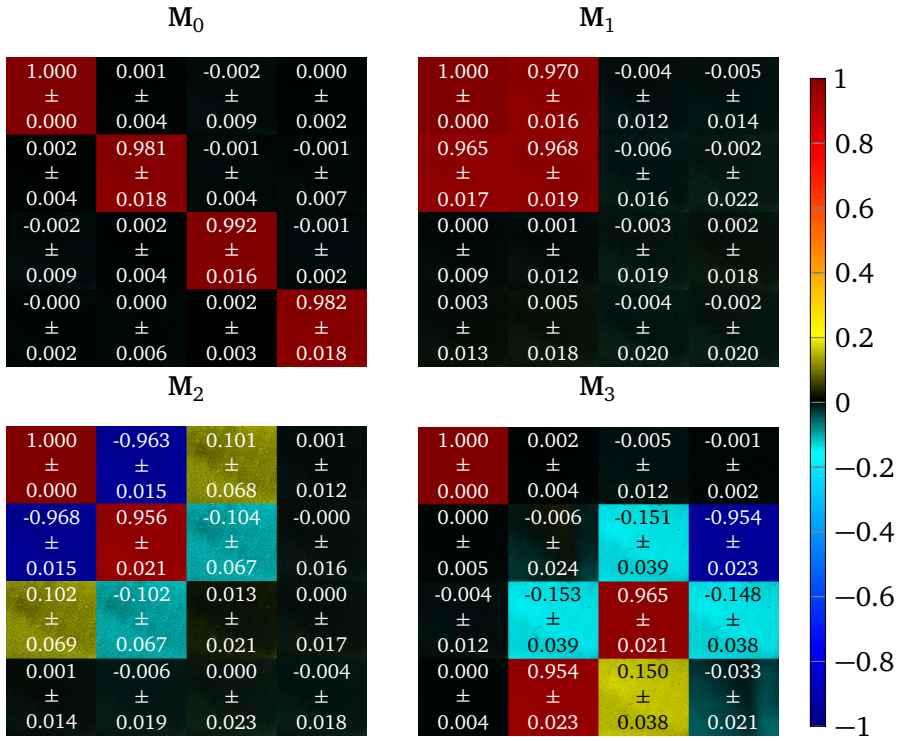

Figure 7.11: Reconstructed and Cloude filtered (cf. section 2.6.1) calibration samples for a 640 px × 640 px crop. $\mathbf{M}_0$ is air. $\mathbf{M}_1$ and $\mathbf{M}_2$ are polarisers oriented at approximately 0° and 90° respectively. $\mathbf{M}_3$ is a retarder with fast-axis oriented at approximately 55°. The printed values are the mean average and standard deviation of the respective element.

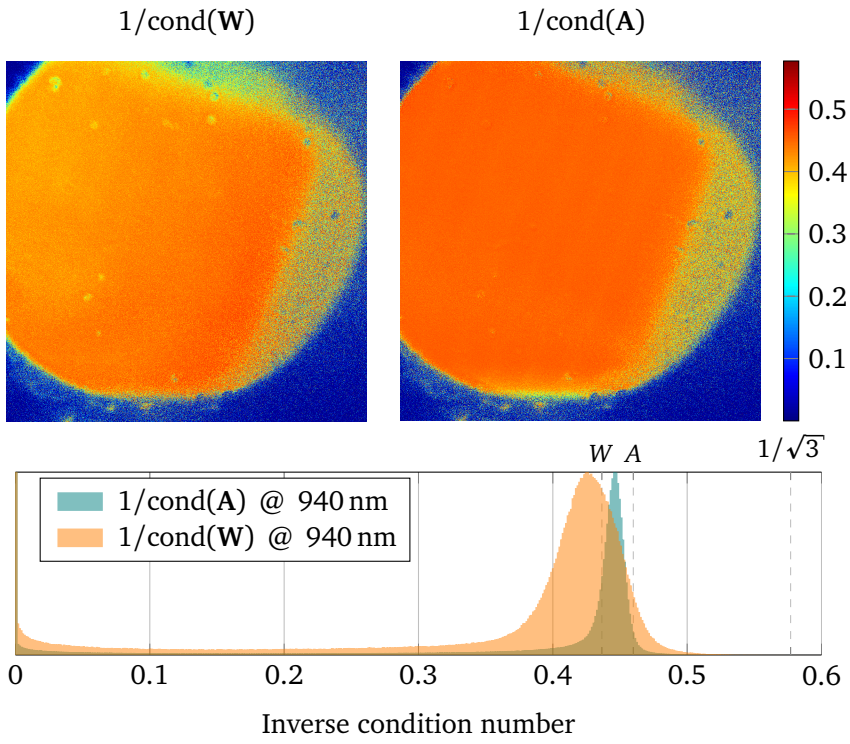

Figure 7.12: Normalised inverse condition number maps and histogram for the **W** and **A** matrices for a 1128 px × 1128 px crop covering most of the image.

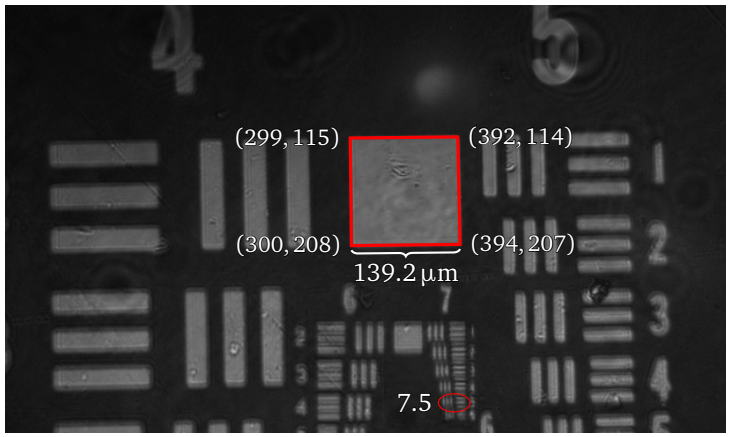

Figure 7.13: *Resolution Test Target* image taken using the µMMI configuration. Each side of the 4.2 element is 139.2 µm long and was found to constitute approximately 93 pixels, each pixel is therefore approximately 1.5 µm × 1.5 µm. The smallest resolved line in this image is the 7.5 element which has a line width of 2.46 µm.

7.4. Conclusion

A spectroscopic (550 nm to 1150 nm) Mueller matrix imaging microscopy ellipsometer (μMMI) based on ferroelectric liquid crystals (FLCs) and waveplates (WPs) was designed and built. The polarisation state generator (PSG) and analyser (PSA) both show promising results with a measured inverse condition number of above 0.4 in the range 550 nm to 1000 nm. A calibration benchmark using the eigenvalue calibration method using a light source at 940 nm indicate that the instrument is working as intended. Some problems with noise appear to be present, and countermeasures are proposed.

The current placement of the calibration samples introduce an error when specimens are measured in the sample position indicated in figure 7.8, it is therefore proposed to move the calibration samples closer to the sample holder. This will result in moving the objective lens and mirror from the modulation matrix **W** to the analyser matrix **A**. This is though to also give an overall better inverse condition number for the system, as it is predicted that the lenses will have less impact together with the higher inverse condition number component. A second alteration to the design which may improve 1/cond(**W**), is moving the condenser lens after the PSG, allowing a more collimated beam through the PSG. Further experimentation with the configuration of the components is encouraged to obtain a better calibration.

In conclusion, the developed μMMI-system show good potential for applications in spectroscopic Mueller matrix imaging.

Part IV.

Afterword

Chapter 8

Final thoughts and outlook

8.1. Instrumentation

At the time of writing, both MMI-instruments used in this thesis operate using software written in LabView and MATLAB. This suite of programs allows for quick and easy prototyping, but has limitations when it comes to speed.

One of the more computationally intensive tasks is the eigenvalue calibration algorithm (ECM) currently implemented in MATLAB, which takes slightly over 1 hour to complete for a 1128 px × 1128 px image on an i7-3770K CPU @ 4.5 GHz. Since the ECM algorithm and decomposition methods are highly parallelisable as each pixel is independent from the others, the improvement in computation-time is in theory only limited by the number of available threads, and the time needed to compute one pixel. By writing the algorithms for use with commercially available graphics cards using e.g. CUDA,[122] it is estimated that the computation time can be decreased drastically to a few minutes, or even seconds if enough computer power is present.

With due diligence it is entirely possible to create a user-friendly suite with tolerable computation times for a commercial product.

8.2. Silicon strain imaging

The solar cell industry showed interest when the strain images in section 6 were presented at the Norwegian Solar Cell Conference 2014 at Son. Academic interest has also been expressed in these results. It may therefore be desirable to pursue further development and verification of the theories and techniques presented in this thesis. A replication of the experiment performed by He et al.[38] using the MMI is proposed to this end.

The model presented in section 2.7.3 for explaining the significance of the fast axis in determining the in-plane stress direction should be revised and expanded. It may also be possible to incorporate the techniques used to determine the 3-D orientation

of collagen fibres to give a 3-D visualisation of the strain field.

8.3. Visualisation of 3-D structures

As mentioned by Ellingsen,[27] the current equipment can be reconfigured to work in reflection. Such a modification will make it easier to implement the equipment for clinical use to characterise cartilage. The techniques used to determine the 3-D structure of collagen fibres may also be applicable in other studies.

8.4. Mueller matrix imaging microscopy

Preliminary tests on the Mueller matrix imaging microscopy ellipsometer (μMMI) built as part of this thesis show promise, but further verification should be carried out. A monochromator may be fitted to the instrument in order to verify the spectroscopic design. Different configurations of the components should also be explored as remarked in section 7.4. Few Mueller matrix imaging microscopes have been reported in literature,[47,123] and as such there is a good opportunity to discover novel applications for the instrument.

The robust and compact design of the polarisation state analyser (PSA) and generator (PSG) make them versatile. They can easily be reconfigured to work in reflection, opening up new possibilities for performing measurements.

Given a higher magnification than the previous Mueller matrix imaging ellipsometer at the Applied Optics Group, it may be of interest to repeat the measurements presented in section 6.2 to obtain higher resolution images which may reveal more structural details.

Possible applications for the μMMI include investigation of both biological samples and nanostructures, e.g. amyloid protein structures, ateriosclerotic plaques, or nanoparticles in sol-gel glasses.

References

[1] D. GOLDSTEIN *Polarized Light* 2nd ed. Marcel Dekker, 2003 (see pp. 3, 6)

[2] P. DRUDE 'Ueber Oberflächenschichten. I. Theil' in: *Annalen der Physik* 272.2 (1889), pp. 532–560 DOI: 10.1002/andp.18892720214 (see p. 3)

[3] P. DRUDE 'Ueber Oberflächenschichten. II. Theil' in: *Annalen der Physik* 272.4 (1889), pp. 865–897 DOI: 10.1002/andp.18892720409 (see p. 3)

[4] J. HOVENIER and C. VAN DER MEE 'Fundamental relationships relevant to the transfer of polarized light in a scattering atmosphere' in: *Astronomy and Astrophysics* 128 (1983), pp. 1–16 (see p. 3)

[5] M. SCHADT and W. HELFRICH 'Voltage-dependent Optical Activity of a Twisted Nematic Liquid Crystal' in: *Applied Physics Letters* 18.4 (1971), pp. 127–128 DOI: 10.1063/1.1653593 (see p. 3)

[6] D. J. GRIFFITHS *Introduction to electrodynamics* 3rd ed. San Francisco, California: Pearson Benjamin Cummings, 2008 (see p. 5)

[7] H. WANG, L. SHI, B. LUKYANCHUK, C. SHEPPARD and C. T. CHONG 'Creation of a needle of longitudinally polarized light in vacuum using binary optics' in: *Nat Photon* 2.8 (2008), pp. 501–505 DOI: 10.1038/nphoton.2008.127 (see p. 5)

[8] Q. ZHAN 'Cylindrical vector beams: from mathematical concepts to applications' in: *Adv. Opt. Photon.* 1.1 (Jan. 2009), pp. 1–57 DOI: 10.1364/AOP.1.000001 (see p. 5)

[9] M. ZHU, Q. CAO and H. GAO 'Creation of a 50,000λ long needle-like field with 0.36λ width' in: *J. Opt. Soc. Am. A* 31.3 (Mar. 2014), pp. 500–504 DOI: 10.1364/JOSAA.31.000500 (see p. 5)

[10] R. A. CHIPMAN 'Handbook of Optics' in: *Devices, Measurements, and Properties* ed. by M. BASS, E. W. V. STRYLAND and W. L. WOLFE 2nd ed. vol. II IV vols. USA: McGraw-Hill, 1995 chap. 22 (see pp. 5, 8, 12, 16, 21, 141)

[11] P. HAUGE, R. MULLER and C. SMITH 'Conventions and formulas for using the Mueller-Stokes calculus in ellipsometry' in: *Surface Science* 96.1–3 (1980), pp. 81 –107 DOI: 10.1016/0039-6028(80)90296-4 (see pp. 6, 7, 9, 11)

[12] H. ANTON and C. RORRES *Elementary Linear Algebra* 9th ed. Wiley, 2005 (see pp. 6, 14, 29)

[13] P. THEOCARIS and E. GDOUTOS *Matrix Theory of Photoelasticity* Springer-Verlag Berlin Heidelberg, 1979 (see p. 7)

[14] R. C. JONES 'New calculus for the treatment of optical systems' in: *Journal of the Optical Society of America* 31 (1941), pp. 488–493 (see p. 7)

[15] F. L. PEDROTTI, L. M. PEDROTTI and L. S. PEDROTTI *Introduction to Optics* 3rd ed. San Francisco: Pearson Addison Wesley, 2007 (see pp. 7, 16, 25, 91)

[16] T. VOIPIO, T. SETÄLÄ and A. T. FRIBERG 'Partial polarization theory of pulsed optical beams' in: *J. Opt. Soc. Am. A* 30.1 (Jan. 2013), pp. 71–81 DOI: 10.1364/JOSAA.30.000071 (see p. 7)

[17] B. E. A. SALEH and M. C. TEICH *Fundamentals of Photonics* 2nd ed. Wiley-Interscience, 2007 (see pp. 8, 15, 16, 25)

[18] F. JONSSON 'The nonlinear optics of magneto-optic media' PhD thesis KTH, Physics, 2000, pp. xii, 84 (see p. 9)

[19] H. TOMPKINS and E. A. IRENE *Handbook of ellipsometry* William Andrew, 2005 (see p. 10)

[20] H. EVES *Elementary Matrix Theory* Dover Publications, 1980 (see p. 10)

[21] J. J. GIL 'Characteristic properties of Mueller matrices' in: *Journal of the Optical Society of America A* 17.2 (Feb. 2000), pp. 328–334 DOI: 10.1364/JOSAA.17.000328 (see p. 13)

[22] C. V. M. VAN DER MEE 'An eigenvalue criterion for matrices transforming Stokes parameters' in: *Journal of Mathematical Physics* 34.11 (1993), pp. 5072–5088 DOI: 10.1063/1.530343 (see p. 13)

[23] R. SIMON 'The connection between Mueller and Jones matrices of polarization optics' in: *Optics Communications* 42.5 (1982), pp. 293 –297 DOI: 10.1016/0030-4018(82)90234-6 (see p. 13)

[24] S. R. CLOUDE 'Conditions For The Physical Realisability Of Matrix Operators In Polarimetry' in: *Proc. SPIE* 1166 (1990), pp. 177–187 DOI: 10.1117/12.962889 (see p. 13)

[25] D. G. M. ANDERSON and R. BARAKAT 'Necessary and sufficient conditions for a Mueller matrix to be derivable from a Jones matrix' in: *Journal of the Optical Society of America A* 11.8 (Aug. 1994), pp. 2305–2319 DOI: 10.1364/JOSAA.11.002305 (see p. 13)

[26] F. STABO-EEG, M. KILDEMO, I. S. NERBØ and M. LINDGREN 'Well-conditioned multiple laser Mueller matrix ellipsometer' in: *Optical Engineering* 47.7 (2008), pp. 073604–073604–9 DOI: 10.1117/1.2957047 (see pp. 13, 31, 47)

[27] P. G. ELLINGSEN 'Development of Mueller matrix imaging technique for characterising collagen spatial orientation in cartilage: comparison to multiphoton microscopy' Master's thesis NTNU, 2010 (see pp. 13, 42, 47, 98)

[28] S. R. CLOUDE 'Group theory and polarisation algebra' in: *Optik (Stuttgart)* 75.1 (1986) ed. by ELSEVIER, pp. 26–36 (see pp. 13, 111)

[29] S. R. CLOUDE and E. POTTIER 'Concept of polarization entropy in optical scattering' in: *Optical Engineering* 34.6 (1995), pp. 1599–1610 DOI: 10.1117/12.202062 (see pp. 13, 14)

[30] S. H. FRIEDBERG, A. J. INSEL and L. E. SPENCE *Linear Algebra* 4th ed. Illinois State University: Prentice Hall, 2003 (see pp. 14, 29, 32)

[31] T. S. NARASIMHAMURTY *Photoelastic and electro-optic properties of crystals* New York: Plenum Press, 1981 (see pp. 15, 17)

[32] S. R. LEDERHANDLER 'Infrared Studies of Birefringence in Silicon' in: *Journal of Applied Physics* 30.11 (1959), pp. 1631–1638 DOI: 10.1063/1.1735026 (see p. 16)

[33] K. RAMESH *Digital Photoelasticity* 1st ed. Springer, 2000 (see pp. 16, 114)

[34] V. GANAPATI, S. SCHOENFELDER, S. CASTELLANOS, S. OENER, R. KOEPGE, A. SAMPSON, M. A. MARCUS, B. LAI, H. MORHENN, G. HAHN, J. BAGDAHN and T. BUONASSISI 'Infrared birefringence imaging of residual stress and bulk defects in multicrystalline silicon' in: *Journal of Applied Physics* 108.6 (2010) DOI: 10.1063/1.3468404 (see p. 16)

[35] D. F. NELSON and M. LAX 'Theory of the Photoelastic Interaction' in: *Physical Review B* 3 (8 Apr. 1971), pp. 2778–2794 DOI: 10.1103/PhysRevB.3.2778 (see p. 17)

[36] J. NYE *Physical Properties of Crystals* Clarendon Press, 1957 (see p. 17)

[37] C. KITTEL *Introduction to Solid State Physics* 8th ed. John Wiley & Sons, Inc., 2005 (see pp. 17, 67)

[38] S. HE, T. ZHENG and S. DANYLUK 'Analysis and determination of the stress-optic coefficients of thin single crystal silicon samples' in: *Journal of Applied Physics* 96.6 (2004), pp. 3103–3109 DOI: 10.1063/1.1774259 (see pp. 17, 18, 20, 70, 97, 113–115)

[39] F. LI 'Study of stress measurement using polariscope' PhD thesis 2010 (see p. 20)

[40] A. GIARDINI 'Piezobirefringence in silicon' in: *American Mineralogist* 43 (1958), p. 249 (see p. 20)

[41] T. IWAKI and T. KOIZUMI 'Stress-optic law in a single crystal and its application to photo-anisotropic elasticity' English in: *Experimental Mechanics* 29.3 (1989), pp. 295–299 DOI: 10.1007/BF02321411 (see p. 20)

[42] R. M. A. AZZAM 'Arrangement of four photodetectors for measuring the state of polarization of light' in: *Optical Letters* 10.7 (July 1985), pp. 309–311 DOI: 10.1364/OL.10.000309 (see p. 21)

[43] R. C. THOMPSON, J. R. BOTTIGER and E. S. FRY 'Measurement of polarized light interactions via the Mueller matrix' in: *Applied Optics* 19.8 (Apr. 1980), pp. 1323–1332 DOI: 10.1364/AO.19.001323 (see pp. 21, 81)

[44] E. COMPAIN and B. DREVILLON 'High-frequency modulation of the four states of polarization of light with a single phase modulator' in: *Review of Scientific Instruments* 69.4 (1998), pp. 1574–1580 DOI: 10.1063/1.1148811 (see pp. 21, 81)

[45] F. DELPLANCKE 'Automated high-speed Mueller matrix scatterometer' in: *Applied Optics* 36.22 (Aug. 1997), pp. 5388–5395 DOI: 10.1364/AO.36.005388 (see pp. 21, 81)

[46] B. C. E. PELZ, C. WESCHENMOSER, S. GOELZ, J. P. FISCHER, R. O. W. BURK and J. F. BILLE 'In-vivo measurement of the retinal birefringence with regard to corneal effects using an electro-optical ellipsometer' in: vol. 2930 1996, pp. 92–101 DOI: 10.1117/12.260860 (see pp. 21, 81)

[47] D. LARA and C. DAINTY 'Axially resolved complete Mueller matrix confocal microscopy' in: *Applied Optics* 45.9 (Mar. 2006), pp. 1917–1930 DOI: 10.1364/AO.45.001917 (see pp. 21, 81, 98)

[48] J. M. BUENO and P. ARTAL 'Double-pass imaging polarimetry in the human eye' in: *Optical Letters* 24.1 (Jan. 1999), pp. 64–66 DOI: 10.1364/OL.24.000064 (see pp. 21, 81)

[49] A. M. GANDORFER 'Ferroelectric retarders as an alternative to piezoelastic modulators for use in solar Stokes vector polarimetry' in: *Optical Engineering* 38.8 (1999), pp. 1402–1408 DOI: 10.1117/1.602183 (see pp. 21, 81)

[50] E. GARCIA-CAUREL, A. D. MARTINO and B. DRÉVILLON 'Spectroscopic Mueller polarimeter based on liquid crystal devices' in: *Thin Solid Films* 455–456.0 (2004) The 3rd International Conference on Spectroscopic Ellipsometry, pp. 120–123 DOI: 10.1016/j.tsf.2003.12.056 (see pp. 21, 81)

[51] B. LAUDE-BOULESTEIX, A. D. MARTINO, B. DRÉVILLON and L. SCHWARTZ 'Mueller polarimetric imaging system with liquid crystals' in: *Applied Optics* 43.14 (May 2004), pp. 2824–2832 DOI: 10.1364/AO.43.002824 (see pp. 21, 81)

[52] J. LADSTEIN, F. STABO-EEG, E. GARCIA-CAUREL and M. KILDEMO 'Fast near-infrared spectroscopic Mueller matrix ellipsometer based on ferroelectric liquid crystal retarders' in: *Physica Status Solidi (c)* 5.5 (2008), pp. 1097–1100 DOI: 10.1002/pssc.200777902 (see pp. 21, 47, 81)

[53] L. M. S. Aas, P. G. Ellingsen, B. E. Fladmark, P. A. Letnes and M. Kildemo 'Overdetermined broadband spectroscopic Mueller matrix polarimeter designed by genetic algorithms' in: *Optical Express* 21.7 (Apr. 2013), pp. 8753–8762 DOI: 10.1364/OE.21.008753 (see pp. 21, 29, 81)

[54] R. M. A. Azzam 'Photopolarimetric measurement of the Mueller matrix by Fourier analysis of a single detected signal' in: *Optical Letters* 2.6 (June 1978), pp. 148–150 DOI: 10.1364/OL.2.000148 (see pp. 21, 81)

[55] J. L. Pezzaniti and R. A. Chipman 'Mueller matrix imaging polarimetry' in: *Optical Engineering* 34.6 (1995), pp. 1558–1568 DOI: 10.1117/12.206161 (see pp. 21, 81)

[56] R. W. Collins and J. Koh 'Dual rotating-compensator multichannel ellipsometer: Instrument design for real-time Mueller matrix spectroscopy of surfaces and films' in: *J. Optical Society of America A* 16.8 (Aug. 1999), pp. 1997–2006 DOI: 10.1364/JOSAA.16.001997 (see pp. 21, 81)

[57] D. S. Sabatke, M. R. Descour, E. L. Dereniak, W. C. Sweatt, S. A. Kemme and G. S. Phipps 'Optimization of retardance for a complete Stokes polarimeter' in: *Optical Letters* 25.11 (June 2000), pp. 802–804 DOI: 10.1364/OL.25.000802 (see pp. 21, 32)

[58] J. H. Holland 'Genetic algorithms' in: *Scientific American* 267.1 (1992), pp. 66–72 (see p. 22)

[59] P. A. Letnes, I. S. Nerbø, L. M. S. Aas, P. G. Ellingsen and M. Kildemo 'Fast and optimal broad-band Stokes/Mueller polarimeter design by the use of a genetic algorithm' in: *Optical Express* 18.22 (Oct. 2010), pp. 23095–23103 DOI: 10.1364/OE.18.023095 (see pp. 22, 82)

[60] D. Floreano and C. Mattiussi *Bio-inspired artificial intelligence: theories, methods, and technologies* MIT press, 2008 (see p. 22)

[61] R. M. Azzam and N. M. Bashara *Ellipsometry and polarized light* North-Holland. sole distributors for the USA and Canada, Elsevier Science Publishing Co., Inc., 1987 (see p. 26)

[62] M. Kildemo, O. Hunderi and B. Drévillon 'Approximation of reflection coefficients for rapid real-time calculation of inhomogeneous films' in: *J. Opt. Soc. Am. A* 14.4 (Apr. 1997), pp. 931–939 DOI: 10.1364/JOSAA.14.000931 (see p. 26)

[63] E. Compain, S. Poirier and B. Drevillon 'General and Self-Consistent Method for the Calibration of Polarization Modulators, Polarimeters, and Mueller-Matrix Ellipsometers' in: *Applied Optics* 38.16 (June 1999), pp. 3490–3502 DOI: 10.1364/AO.38.003490 (see pp. 27–29, 82)

[64] R. Hagen, S. Roch and B. Silbermann *C*-algebras and numerical analysis* vol. 236 CRC Press, 2000 (see p. 28)

[65] L. M. S. Aas 'Mueller Matrix Ellipsometric Imaging and Spectroscopy' Doctoral thesis NTNU, 2013 (see p. 29)

[66] F. Stabo-Eeg 'Development of instrumentation for Mueller matrix ellipsometry' PhD thesis Norwegian University of Science and Technology, Department of Physics, 2009 (see pp. 31, 47)

[67] J. S. Tyo 'Noise equalization in Stokes parameter images obtained by use of variable-retardance polarimeters' in: *Optical Letters* 25.16 (Aug. 2000), pp. 1198–1200 DOI: 10.1364/OL.25.001198 (see pp. 32, 57, 82, 83)

[68] J. A. Woollam, B. Johs, C. M. Herzinger, J. Hilfiker, R. Synowicki and C. L. Bungay 'Overview of variable angle spectroscopic ellipsometry (VASE), part I: basic theory and typical applications' in: *SPIE, CR72* (1999), pp. 3–28 (see p. 33)

[69] J. N. Hilfiker, N. Singh, T. Tiwald, D. Convey, S. M. Smith, J. H. Baker and H. G. Tompkins 'Survey of methods to characterize thin absorbing films with Spectroscopic Ellipsometry' in: *Thin Solid Films* 516.22 (2008) Proceedings of the {EMRS} 2007 Fall Meeting Symposium H: Current trends in optical and x-ray metrology of advanced materials and devices {II} Warsaw, Poland, pp. 7979 –7989 DOI: 10.1016/j.tsf.2008.04.060 (see p. 33)

[70] S.-Y. Lu and R. A. Chipman 'Homogeneous and inhomogeneous Jones matrices' in: *Journal of the Optical Society of America* 11.2 (Feb. 1994), pp. 766–773 DOI: 10.1364/JOSAA.11.000766 (see p. 33)

[71] S.-Y. Lu and R. A. Chipman 'Interpretation of Mueller matrices based on polar decomposition.' in: *Journal of the Optical Society of America* 13 (5 1996), pp. 1106–1113 DOI: 10.1364/JOSAA.13.001106 (see pp. 33–35, 37)

[72] J. J. Gil and E. Bernabeu 'Depolarization and Polarization Indices of an Optical System' in: *Optica Acta: International Journal of Optics* 33.2 (1986), pp. 185–189 DOI: 10.1080/713821924 (see p. 34)

[73] S. Manhas, M. K. Swami, P. Buddhiwant, N. Ghosh, P. K. Gupta and K. Singh. 'Mueller matrix approach for determination of optical rotation in chiral turbid media in backscattering geometry' in: *Optical Express* 14 (1 2006), pp. 190–202 (see p. 34)

[74] R. M. A. Azzam 'Propagation of partially polarized light through anisotropic media with or without depolarization: A differential 4x4 matrix calculus' in: *Journal of the Optical Society of America* 68.12 (Dec. 1978), pp. 1756–1767 DOI: 10.1364/JOSA.68.001756 (see pp. 34, 38)

[75] R. Ossikovski 'Differential matrix formalism for depolarizing anisotropic media' in: *Optics Letters* 36.12 (June 2011), pp. 2330–2332 DOI: 10.1364/OL.36.002330 (see pp. 34, 38)

[76] S. KUMAR, H. PURWAR, R. OSSIKOVSKI, I. A. VITKIN and N. GHOSH 'Comparative study of differential matrix and extended polar decomposition formalisms for polarimetric characterization of complex tissue-like turbid media' in: *Journal of Biomedical Optics* 17.10 (2012), p. 105006 DOI: 10.1117/1.jbo.17.10.105006 (see pp. 34, 38–40)

[77] H. D. NOBLE and R. A. CHIPMAN 'Mueller matrix roots algorithm and computational considerations' in: *Optical Express* 20.1 (Jan. 2012), pp. 17–31 DOI: 10.1364/OE.20.000017 (see pp. 34, 41)

[78] R. OSSIKOVSKI 'Differential and product Mueller matrix decompositions: a formal comparison' in: *Optical Letters* 37.2 (Jan. 2012), pp. 220–222 DOI: 10.1364/OL.37.000220 (see pp. 34, 41)

[79] J. MORIO and F. GOUDAIL 'Influence of the order of diattenuator, retarder, and polarizer inpolar decomposition of Mueller matrices' in: *Optical Letters* 29.19 (Oct. 2004), pp. 2234–2236 DOI: 10.1364/OL.29.002234 (see p. 37)

[80] R. OSSIKOVSKI, A. D. MARTINO and S. GUYOT 'Forward and reverse product decompositions of depolarizing Mueller matrices' in: *Optical Letters* 32.6 (Mar. 2007), pp. 689–691 DOI: 10.1364/OL.32.000689 (see p. 37)

[81] R. OSSIKOVSKI 'Analysis of depolarizing Mueller matrices through a symmetric decomposition' in: *Journal of the Optical Society of America* 26.5 (May 2009), pp. 1109–1118 DOI: 10.1364/JOSAA.26.001109 (see p. 38)

[82] R. SRIDHAR and R. SIMON 'Normal form for Mueller Matrices in Polarization Optics' in: *Journal of Modern Optics* 41.10 (1994), pp. 1903–1915 DOI: 10.1080/09500349414551811 (see p. 38)

[83] R. C. JONES 'A New Calculus for the Treatment of Optical Systems. VII. Properties of the N-Matrices' in: *Journal of the Optical Society of America* 38.8 (Aug. 1948), pp. 671–683 DOI: 10.1364/JOSA.38.000671 (see p. 38)

[84] N. ORTEGA-QUIJANO and J. L. ARCE-DIEGO 'Depolarizing differential Mueller matrices' in: *Opt. Lett.* 36.13 (July 2011), pp. 2429–2431 DOI: 10.1364/OL.36.002429 (see p. 38)

[85] P. G. ELLINGSEN, L. M. S. AAS, V. S. HAGEN, R. KUMAR, M. B. LILLEDAHL and M. KILDEMO 'Mueller matrix three-dimensional directional imaging of collagen fibers' in: *Journal of Biomedical Optics* 19.2 (2014), p. 026002 DOI: 10.1117/1.JBO.19.2.026002 (see pp. 40, 42–44, 47, 72–74, 76, 77)

[86] H. KU 'Notes on the use of propagation of error formulas' in: *Journal of Research of the National Bureau of Standards* 70.4 (1966) (see p. 40)

[87] M. KILDEMO, J. MARIA, P. G. ELLINGSEN and L. M. S. AAS 'Parametric model of the Mueller matrix of a Spectralon white reflectance standard deduced by polar decomposition techniques' in: *Optical Express* 21.15 (July 2013), pp. 18509–18524 DOI: 10.1364/OE.21.018509 (see p. 40)

[88] H. D. NOBLE, S. C. MCCLAIN and R. A. CHIPMAN 'Mueller matrix roots depolarization parameters' in: *Applied Optics* 51.6 (Feb. 2012), pp. 735–744 DOI: 10.1364/AO.51.000735 (see p. 41)

[89] H. GOLDSTEIN, C. POOLE and J. SAFKO *Classical Mechanics* 3rd ed. Addison Wesley, 2002 (see p. 42)

[90] J. LADSTEIN 'Realization of spectroscopic Mueller Matrix Ellipsometer based on Ferroelectric Liquid Crystal Retarders' Master's thesis NTNU, 2007 (see pp. 47, 57, 81–83)

[91] J. LADSTEIN, M. KILDEMO, G. K. SVENDSEN, I. S. NERBØ and F. STABO-EEG 'Characterisation of liquid crystals for broadband optimal design of Mueller matrix ellipsometers' in: vol. 6587 2007, pp. 65870D–65870D–10 DOI: 10.1117/12.722590 (see pp. 47, 81)

[92] F. STABO-EEG, M. KILDEMO, I. S. NERBØ and M. LINDGREN 'Well-conditioned multiple laser Mueller matrix ellipsometer' in: *Optical Engineering* 47.7 (2008), pp. 073604–073604 (see p. 47)

[93] H. O. SKJERPING 'Concept design and prototyping of near-infra-red Mueller Matrix imaging system, for application in biomedicine and related topics.' Master's thesis NTNU, 2008 (see p. 47)

[94] L. M. S. AAS 'Mueller Matrix Ellipsometric Imaging; Instrumentation and Applications' Master's thesis NTNU, 2009 (see p. 47)

[95] L. M. AAS, P. G. ELLINGSEN, M. KILDEMO and M. LINDGREN 'Dynamic response of a fast near infra-red Mueller matrix ellipsometer' in: *Journal of Modern Optics* 57.17 (2010), pp. 1603–1610 DOI: 10.1080/09500340.2010.515750 (see p. 47)

[96] L. M. S. AAS, P. G. ELLINGSEN and M. KILDEMO 'Near infra-red Mueller matrix imaging system and application to retardance imaging of strain' in: *Thin Solid Films* 519.9 (2011) 5th International Conference on Spectroscopic Ellipsometry (ICSE-V), pp. 2737 –2741 DOI: 10.1016/j.tsf.2010.12.093 (see p. 47)

[97] P. G. ELLINGSEN, M. B. LILLEDAHL, L. M. S. AAS, C. D. L. DAVIES and M. KILDEMO 'Quantitative characterization of articular cartilage using Mueller matrix imaging and multiphoton microscopy' in: *Journal of Biomedical Optics* 16.11 (2011), pp. 116002–116002–6 DOI: 10.1117/1.3643721 (see pp. 47, 73)

[98] C. DONOLATO 'Modeling the effect of dislocations on the minority carrier diffusion length of a semiconductor' in: *Journal of Applied Physics* 84.5 (1998), pp. 2656–2664 DOI: 10.1063/1.368378 (see p. 61)

[99] G. STOKKAN, S. RIEPE, O. LOHNE and W. WARTA 'Spatially resolved modeling of the combined effect of dislocations and grain boundaries on minority carrier lifetime in multicrystalline silicon' in: *Journal of Applied Physics* 101.5 (2007) DOI: 10.1063/1.2435815 (see p. 61)

[100] H. MÖLLER, C. FUNKE, M. RINIO and S. SCHOLZ 'Multicrystalline silicon for solar cells' in: *Thin Solid Films* 487.1–2 (2005), pp. 179 –187 DOI: 10.1016/j.tsf.2005.01.061 (see p. 61)

[101] I. TAKAHASHI, N. USAMI, K. KUTSUKAKE, G. STOKKAN, K. MORISHITA and K. NAKAJIMA 'Generation mechanism of dislocations during directional solidification of multicrystalline silicon using artificially designed seed' in: *Journal of Crystal Growth* 312.7 (2010), pp. 897 –901 DOI: 10.1016/j.jcrysgro.2010.01.011 (see pp. 61, 62, 70)

[102] B. RYNINGEN, G. STOKKAN, M. KIVAMBE, T. ERVIK and O. LOHNE 'Growth of dislocation clusters during directional solidification of multicrystalline silicon ingots' in: *Acta Materialia* 59.20 (2011), pp. 7703 –7710 DOI: 10.1016/j.actamat.2011.09.002 (see p. 61)

[103] R. VARIN, K. KURZYDLOWSKI and K. TANGRI 'Analytical treatment of grain boundary sources for dislocations' in: *Materials Science and Engineering* 85.0 (1987), pp. 115 –126 DOI: 10.1016/0025-5416(87)90473-3 (see pp. 61, 67)

[104] M. HOPCROFT, W. NIX and T. KENNY in: *Journal of Microelectromechanical Systems* () (see p. 61)

[105] T. K. ERVIK 'Dislocations in directionally solidified crystalline silicon' PhD thesis NTNU, Dec. 2013 (see p. 62)

[106] A VOIGT, E WOLF and H. STRUNK 'Grain orientation and grain boundaries in cast multicrystalline silicon' in: *Materials Science and Engineering B* 54.3 (1998), pp. 202–206 (see p. 62)

[107] I. TAKAHASHI, N. USAMI, K. KUTSUKAKE, K. MORISHITA and K. NAKAJIMA 'Computational Investigation of Relationship between Shear Stress and Multicrystalline Structure in Silicon' in: *Japanese Journal of Applied Physics* 49.4S (2010), 04DP01 (see pp. 62, 70)

[108] J. J. WORTMAN and R. A. EVANS 'Young's Modulus, Shear Modulus, and Poisson's Ratio in Silicon and Germanium' in: *Journal of Applied Physics* 36.1 (1965), pp. 153–156 DOI: 10.1063/1.1713863 (see p. 62)

[109] J TURLEY and G SINES 'The anisotropy of Young's modulus, shear modulus and Poisson's ratio in cubic materials' in: *Journal of Physics D: Applied Physics* 4.2 (1971), p. 264 (see p. 62)

[110] A. AUTRUFFE, V. S. HAGEN, L. ARNBERG and M. D. S. LUNDBERG 'Coincidence site lattice bi-crystals growth: Defect generation' in: *Journal of Crystal Growth* to be submitted for publication (2014) to be submitted for publication (see pp. 62, 63, 68)

[111] 'Nucleation in small scale multicrystalline silicon ingots' in: *Journal of Crystal Growth* 361.0 (2012), pp. 206 –211 DOI: 10.1016/j.jcrysgro.2012.09.045 (see p. 62)

[112] 'Impact of growth rate on impurities segregation at grain boundaries in silicon during Bridgman growth' in: *Journal of Crystal Growth* 372.0 (2013), pp. 180 –188 DOI: 10.1016/j.jcrysgro.2013.03.037 (see p. 62)

[113] B. CUNNINGHAM and D. AST 'High Resolution Electron Microscopy of Grain Boundaries in Silicon' in: *MRS Online Proceedings Library* 5 (Jan. 1981) DOI: 10.1557/PROC-5-21 (see pp. 62, 63)

[114] B. SOPORI 'A new defect etch for polycrystalline silicon' in: *Journal of the Electrochemical Society* 131.3 (1984), pp. 667–672 DOI: 10.1149/1.2115670 (see p. 64)

[115] M. POLYANSKIY *Refractive index database* 2014 URL: http://refractiveindex.info (visited on 21/04/2014) (see p. 67)

[116] P. STOLLER, P. M. CELLIERS, K. M. REISER and A. M. RUBENCHIK 'Quantitative Second-Harmonic Generation Microscopy in Collagen' in: *Applied Optics* 42.25 (Sept. 2003), pp. 5209–5219 DOI: 10.1364/AO.42.005209 (see p. 72)

[117] G. COX, E. KABLE, A. JONES, I. FRASER, F. MANCONI and M. D. GORRELL '3-Dimensional imaging of collagen using second harmonic generation' in: *Journal of Structural Biology* 141.1 (2003), pp. 53 –62 DOI: 10.1016/S1047-8477(02)00576-2 (see p. 72)

[118] V. TUCHIN *Tissue Optics Light Scattering Methods and Instruments for Medical Diagnosis* 2nd ed. SPIE Press, 2007 (see p. 82)

[119] B. LAUDE-BOULESTEIX 'Développements instrumentaux en imagerie tomographique et polarimétrique' PhD thesis Ecole polytechnique, 2004 (see p. 82)

[120] A. K "O HLER 'A new method of illumination f "u r photomicrograph purposes' in: *Journal f "u r scientific microscopy and f ü r microscopic technique* 10.4 (1893), pp. 433–440 (see p. 90)

[121] E. ABBE 'Beiträge zur Theorie des Mikroskops und der mikroskopischen Wahrnehmung' German in: *Archiv für mikroskopische Anatomie* 9.1 (1873), pp. 413–418 DOI: 10.1007/BF02956173 (see p. 91)

[122] N. CORPORATION *NVIDIA CUDA C Programming Guide* July 2011 (see p. 97)

[123] M. MUJAT, R. D. FERGUSON and N. IFTIMIA 'Mueller matrix microscopy' in: vol. 8873 2013, 88730E–88730E–9 DOI: 10.1117/12.2024962 (see p. 98)

[124] N. E. DOWLING *Mechanical Behavior of Materials* 2nd ed. Prentice-Hall, 1998, p. 208 (see p. 114)

Appendix A

Selected Jones matrices

$$\begin{bmatrix} 1 & 0 \\ 0 & 1 \end{bmatrix}$$
Air

$$\begin{bmatrix} 1 & 0 \\ 0 & 0 \end{bmatrix}$$
Horizontal polariser

$$\frac{1}{2}\begin{bmatrix} 1 & 1 \\ 1 & 1 \end{bmatrix}$$
45°-polariser

$$\begin{bmatrix} 0 & 0 \\ 0 & 1 \end{bmatrix}$$
Vertical polariser

$$\begin{bmatrix} e^{i\delta_x} & 0 \\ 0 & e^{i\delta_y} \end{bmatrix}$$
General waveplate

$$e^{-i\pi/4}\begin{bmatrix} 1 & 0 \\ 0 & i \end{bmatrix}$$
QWP, Fast axis horizontal

$$e^{i\pi/4}\begin{bmatrix} 1 & 0 \\ 0 & -i \end{bmatrix}$$
QWP, Fast axis vertical

$$e^{-i\pi/2}\begin{bmatrix} 1 & 0 \\ 0 & -1 \end{bmatrix}$$
HWP, Fast axis horizontal

$$e^{i\pi/2}\begin{bmatrix} 1 & 0 \\ 0 & -1 \end{bmatrix}$$
HWP, Fast axis vertical

$$\begin{bmatrix} \cos\psi & -\sin\psi \\ \sin\psi & \cos\psi \end{bmatrix}$$
Rotator

Appendix B

Modified Dirac matrices of $SU(4)$

Modified Dirac matrices by Cloude.[28] Note that $\mathbf{\Omega}_{11} = \mathbf{I}_{4\times4}$.

$$
\mathbf{\Omega}_{12} = \begin{bmatrix} 0 & 1 & 0 & 0 \\ 1 & 0 & 0 & 0 \\ 0 & 0 & 0 & i \\ 0 & 0 & -i & 0 \end{bmatrix}, \quad
\mathbf{\Omega}_{13} = \begin{bmatrix} 0 & 0 & 1 & 0 \\ 0 & 0 & 0 & -i \\ 1 & 0 & 0 & 0 \\ 0 & i & 0 & 0 \end{bmatrix}, \quad
\mathbf{\Omega}_{14} = \begin{bmatrix} 0 & 0 & 0 & 1 \\ 0 & 0 & i & 0 \\ 0 & -i & 0 & 0 \\ 1 & 0 & 0 & 0 \end{bmatrix},
$$

$$
\mathbf{\Omega}_{21} = \begin{bmatrix} 0 & 1 & 0 & 0 \\ 1 & 0 & 0 & 0 \\ 0 & 0 & 0 & -i \\ 0 & 0 & i & 0 \end{bmatrix}, \quad
\mathbf{\Omega}_{22} = \begin{bmatrix} 1 & 0 & 0 & 0 \\ 0 & 1 & 0 & 0 \\ 0 & 0 & -1 & 0 \\ 0 & 0 & 0 & -1 \end{bmatrix}, \quad
\mathbf{\Omega}_{23} = \begin{bmatrix} 0 & 0 & 0 & -i \\ 0 & 0 & 1 & 0 \\ 0 & 1 & 0 & 0 \\ i & 0 & 0 & 0 \end{bmatrix},
$$

$$
\mathbf{\Omega}_{24} = \begin{bmatrix} 0 & 0 & i & 0 \\ 0 & 0 & 0 & 1 \\ -i & 0 & 0 & 0 \\ 0 & 1 & 0 & 0 \end{bmatrix}, \quad
\mathbf{\Omega}_{31} = \begin{bmatrix} 0 & 0 & 1 & 0 \\ 0 & 0 & 0 & i \\ 1 & 0 & 0 & 0 \\ 0 & -i & 0 & 0 \end{bmatrix}, \quad
\mathbf{\Omega}_{32} = \begin{bmatrix} 0 & 0 & 0 & i \\ 0 & 0 & 1 & 0 \\ 0 & 1 & 0 & 0 \\ -i & 0 & 0 & 0 \end{bmatrix},
$$

$$
\mathbf{\Omega}_{33} = \begin{bmatrix} 1 & 0 & 0 & 0 \\ 0 & -1 & 0 & 0 \\ 0 & 0 & 1 & 0 \\ 0 & 0 & 0 & -1 \end{bmatrix}, \quad
\mathbf{\Omega}_{34} = \begin{bmatrix} 0 & -i & 0 & 0 \\ i & 0 & 0 & 0 \\ 0 & 0 & 0 & 1 \\ 0 & 0 & 1 & 0 \end{bmatrix}, \quad
\mathbf{\Omega}_{41} = \begin{bmatrix} 0 & 0 & 0 & 1 \\ 0 & 0 & -i & 0 \\ 0 & i & 0 & 0 \\ 1 & 0 & 0 & 0 \end{bmatrix},
$$

$$
\mathbf{\Omega}_{42} = \begin{bmatrix} 0 & 0 & -i & 0 \\ 0 & 0 & 0 & 1 \\ i & 0 & 0 & 0 \\ 0 & 1 & 0 & 0 \end{bmatrix}, \quad
\mathbf{\Omega}_{43} = \begin{bmatrix} 0 & i & 0 & 0 \\ -i & 0 & 0 & 0 \\ 0 & 0 & 0 & 1 \\ 0 & 0 & 1 & 0 \end{bmatrix}, \quad
\mathbf{\Omega}_{44} = \begin{bmatrix} 1 & 0 & 0 & 0 \\ 0 & -1 & 0 & 0 \\ 0 & 0 & -1 & 0 \\ 0 & 0 & 0 & 1 \end{bmatrix}. \tag{B.1}
$$

Appendix C

Derivation of the crystal orientation dependent stress-optic coefficient

The following is heavily based on work done by He, et al.[38]

Starting with the transformation of the relation between the stress tensor and the dielectric impermeability tensor (eq. (2.37)) to coincide with the principal direction of the impermeability tensor (cf. section 2.7.2),

$$\begin{bmatrix} \Delta\zeta_1 \\ \Delta\zeta_2 \\ \Delta\zeta_3 \\ 0 \\ 0 \\ 0 \end{bmatrix} = \begin{bmatrix} \pi'_{11} & \pi'_{12} & \pi_{12} & 0 & 0 & \pi'_{16} \\ \pi'_{12} & \pi'_{11} & \pi_{12} & 0 & 0 & -\pi'_{16} \\ \pi_{12} & \pi_{12} & \pi_{11} & 0 & 0 & 0 \\ 0 & 0 & 0 & \pi_{44} & 0 & 0 \\ 0 & 0 & 0 & 0 & \pi_{44} & 0 \\ \frac{\pi'_{16}}{2} & \frac{-\pi'_{16}}{2} & 0 & 0 & 0 & \pi'_{66} \end{bmatrix} \begin{bmatrix} \sigma'_x \\ \sigma'_y \\ 0 \\ 0 \\ 0 \\ \tau'_{xy} \end{bmatrix}, \tag{C.1}$$

where σ'_x, σ'_y and τ'_{xy} are the stress components in the principal axes of the impermeability tensor. Generally, the piezo-optical coefficients π'_{ij} are functions of the fast axis orientation angle θ. For the (110) plane observed along the [001] direction, the coefficients are[38]

$$\begin{aligned} \pi'_{11} &= \pi_{11} - \frac{1}{2}\left(\pi_{11} - \pi_{12} - \pi_{44}\right)\sin^2(2\theta), \\ \pi'_{12} &= \pi_{12} + \frac{1}{2}\left(\pi_{11} - \pi_{12} - \pi_{44}\right)\sin^2(2\theta), \\ \pi'_{16} &= -\frac{1}{2}\left(\pi_{11} - \pi_{12} - \pi_{44}\right)\sin(4\theta), \\ \pi'_{66} &= \pi_{44} + \frac{1}{2}\left(\pi_{11} - \pi_{12} - \pi_{44}\right)\sin^2(2\theta). \end{aligned} \tag{C.2}$$

Using the fact that $\Delta\eta'_6 = 0$ (cf. section 2.7) in this principal axis, the relation between τ'_{xy} and $(\sigma'_x - \sigma'_y)$ can be derived, yielding

$$\tau'_{xy} = \frac{\pi'_{16}}{2\pi'_{66}}\left(\sigma'_x - \sigma'_y\right). \tag{C.3}$$

This relation can then be used to determine the principal directions of the residual stresses and their deviation from the principal axes of the impermeability. Starting with equation (2.35) and substituting for Δn with equation (2.43) gives a relation between the phase retardation and impermeability as

$$\delta = \frac{\pi n_0^3 d}{\lambda}\left(\Delta\zeta_1 - \Delta\zeta_2\right), \tag{C.4}$$

where n_0 is the refractive index of the relaxed material. Substituting equations (C.1), (C.2) and (C.4) into the stress-optic law[33]

$$\delta = \frac{2\pi d}{\lambda} C(\sigma_1 - \sigma_2), \tag{C.5}$$

yields the stress-optic coefficient $C(\theta)$ for the (100) orientation observed along the normal direction as[38]

$$C_{(001)}(\theta) = \frac{n_0^3}{2}\left(\frac{\sin^2(2\theta)}{\pi_{44}^2} + \frac{\cos^2(2\theta)}{(\pi_{11} - \pi_{12})^2}\right)^{-1/2}. \tag{C.6}$$

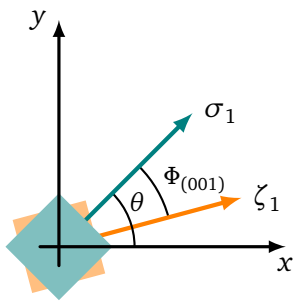

Figure C.1: Physical meaning of the deviation between the principal directions of the dielectric impermeability and the stress tensor. Illustration recreated from original paper.[38]

The angle of deviation between the principal directions of the dielectric impermeability and the stress tensor (fig. C.1) is derived from equation (C.3) as[38,124]

$$\Phi_{(001)} = -\frac{1}{2}\arctan\left(\frac{(\pi_{11} - \pi_{12} - \pi_{44})\sin(4\theta)}{(\pi_{11} - \pi_{12})\sin^2(2\theta) + \pi_{44}(1 + \cos^2(2\theta))}\right). \tag{C.7}$$

The effective stress-optical coefficient of the (111) orientation can be obtained in a similar manner. This is done by first transforming the piezo-optical tensor to

a local coordinate $(11\bar{2}, \bar{1}10, 111)$ before transforming to the principal axes of the impermeability. The resulting stress-optic coefficient can then be expressed as[38]

$$C_{(111)} = \frac{n_0^3}{2} \frac{\pi_{11} - \pi_{12} + 2\pi_{44}}{3}, \tag{C.8}$$

which is independent of the fast axis angle, i.e. (111) silicon behaves as it were mechanically isotropic. The reader is encouraged to read the article by He et al.[38] for more details on the derivation.

Appendix D

Coordinate transfer matrices $\mathbf{H}_{M_i}^{W}$ and $\mathbf{H}_{M_i}^{A}$

See next page.

$$\mathbf{H}^{W}_{M_i} = \tag{D.1}$$

$$\begin{bmatrix}
m_{11}-c_{11} & -c_{21} & -c_{31} & -c_{41} & m_{12} & 0 & 0 & 0 & m_{13} & 0 & 0 & 0 & m_{14} & 0 & 0 & 0 \\
-c_{12} & m_{11}-c_{22} & -c_{32} & -c_{42} & 0 & m_{12} & 0 & 0 & 0 & m_{13} & 0 & 0 & 0 & m_{14} & 0 & 0 \\
-c_{13} & -c_{23} & m_{11}-c_{33} & -c_{43} & 0 & 0 & m_{12} & 0 & 0 & 0 & m_{13} & 0 & 0 & 0 & m_{14} & 0 \\
-c_{14} & -c_{24} & -c_{34} & m_{11}-c_{44} & 0 & 0 & 0 & m_{12} & 0 & 0 & 0 & m_{13} & 0 & 0 & 0 & m_{14} \\
m_{21} & 0 & 0 & 0 & m_{22}-c_{11} & -c_{21} & -c_{31} & -c_{41} & m_{23} & 0 & 0 & 0 & m_{24} & 0 & 0 & 0 \\
0 & m_{21} & 0 & 0 & -c_{12} & m_{22}-c_{22} & -c_{32} & -c_{42} & 0 & m_{23} & 0 & 0 & 0 & m_{24} & 0 & 0 \\
0 & 0 & m_{21} & 0 & -c_{13} & -c_{23} & m_{22}-c_{33} & -c_{43} & 0 & 0 & m_{23} & 0 & 0 & 0 & m_{24} & 0 \\
0 & 0 & 0 & m_{21} & -c_{14} & -c_{24} & -c_{34} & m_{22}-c_{44} & 0 & 0 & 0 & m_{23} & 0 & 0 & 0 & m_{24} \\
m_{31} & 0 & 0 & 0 & m_{32} & 0 & 0 & 0 & m_{33}-c_{11} & -c_{21} & -c_{31} & -c_{41} & m_{34} & 0 & 0 & 0 \\
0 & m_{31} & 0 & 0 & 0 & m_{32} & 0 & 0 & -c_{12} & m_{33}-c_{22} & -c_{32} & -c_{42} & 0 & m_{34} & 0 & 0 \\
0 & 0 & m_{31} & 0 & 0 & 0 & m_{32} & 0 & -c_{13} & -c_{23} & m_{33}-c_{33} & -c_{43} & 0 & 0 & m_{34} & 0 \\
0 & 0 & 0 & m_{31} & 0 & 0 & 0 & m_{32} & -c_{14} & -c_{24} & -c_{34} & m_{33}-c_{44} & 0 & 0 & 0 & m_{34} \\
m_{41} & 0 & 0 & 0 & m_{42} & 0 & 0 & 0 & m_{43} & 0 & 0 & 0 & m_{44}-c_{11} & -c_{21} & -c_{31} & -c_{41} \\
0 & m_{41} & 0 & 0 & 0 & m_{42} & 0 & 0 & 0 & m_{43} & 0 & 0 & -c_{12} & m_{44}-c_{22} & -c_{32} & -c_{42} \\
0 & 0 & m_{41} & 0 & 0 & 0 & m_{42} & 0 & 0 & 0 & m_{43} & 0 & -c_{13} & -c_{23} & m_{44}-c_{33} & -c_{43} \\
0 & 0 & 0 & m_{41} & 0 & 0 & 0 & m_{42} & 0 & 0 & 0 & m_{43} & -c_{14} & -c_{24} & -c_{34} & m_{44}-c_{44}
\end{bmatrix},$$

and

$$\mathbf{H}^{A}_{M_i} = \tag{D.2}$$

$$\begin{bmatrix}
m_{11}-c_{11} & m_{21} & m_{31} & m_{41} & -c_{12} & 0 & 0 & 0 & -c_{13} & 0 & 0 & 0 & -c_{14} & 0 & 0 & 0 \\
m_{12} & m_{22}-c_{11} & m_{32} & m_{42} & 0 & -c_{12} & 0 & 0 & 0 & -c_{13} & 0 & 0 & 0 & -c_{14} & 0 & 0 \\
m_{13} & m_{23} & m_{33}-c_{11} & m_{43} & 0 & 0 & -c_{12} & 0 & 0 & 0 & -c_{13} & 0 & 0 & 0 & -c_{14} & 0 \\
m_{14} & m_{24} & m_{34} & m_{44}-c_{11} & 0 & 0 & 0 & -c_{12} & 0 & 0 & 0 & -c_{13} & 0 & 0 & 0 & -c_{14} \\
-c_{21} & 0 & 0 & 0 & m_{11}-c_{22} & m_{21} & m_{31} & m_{41} & -c_{23} & 0 & 0 & 0 & -c_{24} & 0 & 0 & 0 \\
0 & -c_{21} & 0 & 0 & m_{12} & m_{22}-c_{22} & m_{32} & m_{42} & 0 & -c_{23} & 0 & 0 & 0 & -c_{24} & 0 & 0 \\
0 & 0 & -c_{21} & 0 & m_{13} & m_{23} & m_{33}-c_{22} & m_{43} & 0 & 0 & -c_{23} & 0 & 0 & 0 & -c_{24} & 0 \\
0 & 0 & 0 & -c_{21} & m_{14} & m_{24} & m_{34} & m_{44}-c_{33} & 0 & 0 & 0 & -c_{23} & 0 & 0 & 0 & -c_{24} \\
-c_{31} & 0 & 0 & 0 & -c_{32} & 0 & 0 & 0 & m_{11}-c_{33} & m_{21} & m_{31} & m_{41} & -c_{34} & 0 & 0 & 0 \\
0 & -c_{31} & 0 & 0 & 0 & -c_{32} & 0 & 0 & m_{12} & m_{22}-c_{33} & m_{32} & m_{42} & 0 & -c_{34} & 0 & 0 \\
0 & 0 & -c_{31} & 0 & 0 & 0 & -c_{32} & 0 & m_{13} & m_{23} & m_{33}-c_{33} & m_{43} & 0 & 0 & -c_{34} & 0 \\
0 & 0 & 0 & -c_{31} & 0 & 0 & 0 & -c_{32} & m_{14} & m_{24} & m_{34} & m_{44}-c_{33} & 0 & 0 & 0 & -c_{34} \\
-c_{41} & 0 & 0 & 0 & -c_{42} & 0 & 0 & 0 & -c_{43} & 0 & 0 & 0 & m_{11}-c_{44} & m_{21} & m_{31} & m_{41} \\
0 & -c_{41} & 0 & 0 & 0 & -c_{42} & 0 & 0 & 0 & -c_{43} & 0 & 0 & m_{12} & m_{22}-c_{44} & m_{32} & m_{42} \\
0 & 0 & -c_{41} & 0 & 0 & 0 & -c_{42} & 0 & 0 & 0 & -c_{43} & 0 & m_{13} & m_{23} & m_{33}-c_{44} & m_{43} \\
0 & 0 & 0 & -c_{41} & 0 & 0 & 0 & -c_{42} & 0 & 0 & 0 & -c_{43} & m_{14} & m_{24} & m_{34} & m_{44}-c_{44}
\end{bmatrix}.$$

Appendix E

Implementation of the ECM-routine in MATLAB

Implementation of the ECM algorithm described in section 3.2.1 for the case $n = m = 4$ in MATLAB.

```
function [W,A,condW,condA,errAW,eigRatioAW] = ...
    ECM(B0,B1,B2,B3,theta,optimise,output)
%Calculates the system W and A matrices using the Eigenvalue ...
    Calibration
%Method by optimising the angles of the second polariser and ...
    the waveplate
%using theta as a seed. Self contained.
%optimise ≤ 0 performs optimalisation for only centre pixel.
%optimise == 1 performs this optimalisation for every pixel.
%optimise ≥ 2 performs this optimalisation for every nth pixel.
%output = 'm' outputs A and W as a 4D matrix, while
%output = 'c' outputs A and W as a cell containing 4x4 matrices
%————————————————————
%Vegard Stenhjem Hagen
%          02. mar 2014

    if nargin < 7
        output = 'm';
    end

    if ¬iscell(B0)
    %Convert matrices to cell
        B0 = matrix2cell(B0);
        B1 = matrix2cell(B1);
        B2 = matrix2cell(B2);
        B3 = matrix2cell(B3);
    end

    %Allocate memory
```

```
27      [m,n] = size(B0);
28
29      W = cell(m,n); W(:) = {zeros(4)};
30      A = cell(m,n); A(:) = {zeros(4)};
31
32      C1W = cell(m,n); C1W(:) = {zeros(4)};
33      C2W = cell(m,n); C2W(:) = {zeros(4)};
34      C3W = cell(m,n); C3W(:) = {zeros(4)};
35
36      C1A = cell(m,n); C1A(:) = {zeros(4)};
37      C2A = cell(m,n); C2A(:) = {zeros(4)};
38      C3A = cell(m,n); C3A(:) = {zeros(4)};
39
40      MC1 = cell(m,n); MC1(:) = {zeros(4)};
41      MC2 = cell(m,n); MC2(:) = {zeros(4)};
42      MC3 = cell(m,n); MC3(:) = {zeros(4)};
43
44      %Create CiWs and CiAs
45      parfor i = 1:m*n
46          C1W{i} = B0{i}\B1{i};
47          C2W{i} = B0{i}\B2{i};
48          C3W{i} = B0{i}\B3{i};
49
50          C1A{i} = B1{i}/B0{i};
51          C2A{i} = B2{i}/B0{i};
52          C3A{i} = B3{i}/B0{i};
53      end
54      clear B1 B2 B3
55
56      %Create Ms (calibration samples)
57      thetapol = theta(1);
58      parfor i = 1:m*n
59          MC1{i} = 0.5*trace(C1W{i})*...
60              [1,1,0,0;
61              1,1,0,0;
62              0,0,0,0;
63              0,0,0,0];
64          MC1{i} = rotate(MC1{i},thetapol);
65          MC2{i} = 0.5*trace(C2W{i})*...
66              [1,1,0,0;
67              1,1,0,0;
68              0,0,0,0;
69              0,0,0,0];
70
71          eigList = eigSort(C3W{i});
72          tau = 0.5*(eigList(1) + eigList(2));
73          psi = ...
                atan2(real(sqrt(eigList(2))),real(sqrt(eigList(1))));
74          Δ = 0.5*angle(eigList(4)/eigList(3));
75          Δ = mod(Δ,pi);
76
77          MC3{i}=tau*[1,  cos(2*psi), 0,  0;
78                      cos(2*psi), 1,  0,  0;
```

```
79                      0,  0,  sin(2*psi)*cos(Δ),  sin(2*psi)*sin(Δ);
80                      0,  0,  -sin(2*psi)*sin(Δ), ...
                            sin(2*psi)*cos(Δ)];
81      end
82
83      %Try to refine the seed for the solver
84      y0 = theta(2:3);
85      ys = cell(m,n); ys(:) = {zeros(2,1)};
86      options = ...
87          optimset('Display','off','LargeScale','off','MaxFunEvals',8000,'To
88      i = floor(m*n/2);
89      mc1 = MC1{i}; mc2 = MC2{i}; mc3 = MC3{i};
90      c1w = C1W{i}; c2w = C2W{i}; c3w = C3W{i};
91      c1a = C1A{i}; c2a = C2A{i}; c3a = C3A{i};
92      [y,¬] = fminunc(@(y)...
93          eigenRatios(mc1,mc2,mc3,c1w,c2w,c3w,c1a,c2a,c3a,y),y0,options);
94      y0 = y;
95
96      %Initialize Java progress bar
97      stepS=round(m*n/100);
98      pctRunOnAll ...
            javaaddpath({fullfile(fileparts(which('ParforProgMon')),'java')})
            ;
99      ppm = ParforProgMon('Progress of ECM: ', m*n, stepS, 300, 80);
100 %     tic
101     if (optimise ≤ 0)
102     %Optimise angle for only centre pixel.
103         ys(:) = {y};
104     elseif (optimise == 1)
105     %Optimize angle for every pixel.
106         parfor i = 1:m*n
107             %This trick keeps the overhead down somehow.
108             mc1 = MC1{i}; mc2 = MC2{i}; mc3 = MC3{i};
109             c1w = C1W{i}; c2w = C2W{i}; c3w = C3W{i};
110             c1a = C1A{i}; c2a = C2A{i}; c3a = C3A{i};
111             [y,¬] = fminunc(@(y)...
112                 eigenRatios(mc1,mc2,mc3,c1w,c2w,c3w,c1a,c2a,c3a,y),...
113                     y0,options);
114             ys{i} = y;
115             if mod(i,stepS)==0
116                 ppm.increment();
117             end
118         end
119     elseif (optimise ≥ 2)
120     %Optimize angle for every nth pixel.
121         parfor i = 1:m*n
122             if mod(i,optimise)==1
123                 mc1 = MC1{i}; mc2 = MC2{i}; mc3 = MC3{i};
124                 c1w = C1W{i}; c2w = C2W{i}; c3w = C3W{i};
125                 c1a = C1A{i}; c2a = C2A{i}; c3a = C3A{i};
126                 [y,¬] = fminunc(@(y)...
127                     eigenRatios(mc1,mc2,mc3,c1w,c2w,c3w,c1a,c2a,c3a,y),...
128                         y0,options);
```

```
129                 ys{i} = y;
130             end
131             if mod(i,stepS)==0
132                 ppm.increment();
133             end
134         end
135         for i = 1:optimise:m*n
136             for j = 1:optimise
137                 ys{i+j-1} = ys{i};
138             end
139         end
140     end
141 %     toc
142     ppm.delete()
143     clear mc1 mc2 mc3 c1w c2w c3w c1a c2a c3a
144 
145     %Rotate the calibration samples by optimised angles
146     parfor i = 1:m*n
147         MC2{i} = rotate(MC2{i},ys{i}(1));
148         MC3{i} = rotate(MC3{i},ys{i}(2));
149     end
150 
151     errAW = zeros(m,n);
152     condW = zeros(m,n);
153     condA = zeros(m,n);
154     eigRatioAW = zeros(m,n);
155     R= zeros(m,n);
156 
157     %Calculate W and A and their error estimates errKW, errKA ...
        and err AW
158     parfor i = 1:m*n
159         K = HW(MC1{i},C1W{i}).'*HW(MC1{i},C1W{i}) +...
160             HW(MC2{i},C2W{i}).'*HW(MC2{i},C2W{i}) + ...
                HW(MC3{i},C3W{i}).'*HW(MC3{i},C3W{i});
161         [eigVec,~] = eig(K);
162         eigKW = eig(K);
163         [~,posW] = min(eigKW);
164         W{i} = coordvec2matrix(eigVec(:,posW));
165         condW(i) = cond(W{i});
166         eigKW = sort(eigKW);
167         eigRatioW = eigKW(1)/sum(eigKW(2:end)); %Ladstein
168         errKW = sqrt(eigKW(1)/eigKW(2));
169         if condW(i) < 1000
170             W{i}=real(W{i}./W{i}(1,1));
171         end
172 
173         K = HA(MC1{i},C1A{i}).'*HA(MC1{i},C1A{i}) +...
174             HA(MC2{i},C2A{i}).'*HA(MC2{i},C2A{i}) + ...
                HA(MC3{i},C3A{i}).'*HA(MC3{i},C3A{i});
175         [eigVec,~] = eig(K);
176         eigKA = eig(K);
177         [~,posA] = min(eigKA);
178         A{i} = coordvec2matrix(eigVec(:,posA));
```

```
179         condA(i) = cond(A{i});
180         eigKA = sort(eigKA);
181         eigRatioA = eigKA(1)/sum(eigKA(2:end)); %Ladstein
182         errKA = sqrt(eigKA(1)/eigKA(2));
183         if condA(i) < 1000
184             A{i}=real(A{i}./A{i}(1,1));
185         end
186         eigRatioAW(i) = (eigRatioW + eigRatioA)/2;
187         errAW(i) = 0.5*(errKW+errKA);
188 
189         scaling=norm(B0{i})/norm(A{i}*W{i}); % Ny skalering FSE
190         A{i}=A{i}*sqrt(scaling);
191         W{i}=W{i}*sqrt(scaling);
192     end
193     clear B0
194     if output == 'm'
195         A = cell24Dmatrix(A);
196         W = cell24Dmatrix(W);
197     end
198 
199 end
200 
201 function eigList=eigSort(M)
202 %Outputs the eigenvalues of a 4x4 matrix by the following rules
203     eigList=eig(M);
204 
205     [¬, pos]=sort(abs(imag(eigList)));
206     eigList(:) = eigList(pos);
207 
208     eigList(1:2) = sort(eigList(1:2),'descend');
209     eigList(3:4) = sort(eigList(3:4),'ascend');
210 end
211 
212 function eigRatioAW = ...
        eigenRatios(MC1,MC2,MC3,C1W,C2W,C3W,C1A,C2A,C3A,y)
213 %Calculate the ratio of the smallest eigenvalues to the sum of ...
        the rest
214     MC2 = rotate(MC2,y(1));
215     MC3 = rotate(MC3,y(2));
216 
217     H1 = HW(MC1,C1W);
218     H2 = HW(MC2,C2W);
219     H3 = HW(MC3,C3W);
220     K = H1.'*H1 + H2.'*H2 + H3.'*H3;
221     eigKW = sort(eig(K));
222 
223     H1 = HA(MC1,C1A);
224     H2 = HA(MC2,C2A);
225     H3 = HA(MC3,C3A);
226     K = H1.'*H1 + H2.'*H2 + H3.'*H3;
227     eigKA = sort(eig(K));
228 
229     eigRatioW = eigKW(1)/sum(eigKW(2:end)); %Frantz
```

```
230     eigRatioA = eigKA(1)/sum(eigKA(2:end)); %Frantz
231
232     eigRatioAW = eigRatioW + eigRatioA;
233 end
234
235 function M = rotate(M,theta)
236 %Rotate a muller matrix by theta
237     M=[ 1,  0,              0,              0;
238         0,  cos(2.*theta),  -sin(2.*theta), 0;
239         0,  sin(2.*theta),  cos(2.*theta),  0;
240         0,  0,              0,              1]...
241         *M*...
242         [ 1,  0,            0,              0;
243         0,  cos(2.*theta),  sin(2.*theta),  0;
244         0, -sin(2.*theta),  cos(2.*theta),  0;
245         0,  0,              0,              1];
246 end
247
248 function H = HW(m,c)
249 %Lars Martin - Basis for H_W
250     H = [m(1,1) - c(1,1) -c(2,1) -c(3,1) -c(4,1) m(1,2) 0 0 0 ...
        m(1,3) 0 0 0 m(1,4) 0 0 0;
251         -c(1,2) m(1,1) - c(2,2) -c(3,2) -c(4,2) 0 m(1,2) 0 0 0 ...
            m(1,3) 0 0 0 m(1,4) 0 0;
252         -c(1,3) -c(2,3) m(1,1) - c(3,3) -c(4,3) 0 0 m(1,2) 0 0 ...
            0 m(1,3) 0 0 0 m(1,4) 0;
253         -c(1,4) -c(2,4) -c(3,4) m(1,1) - c(4,4) 0 0 0 m(1,2) 0 ...
            0 0 m(1,3) 0 0 0 m(1,4);
254         m(2,1) 0 0 0 m(2,2) - c(1,1) -c(2,1) -c(3,1) -c(4,1) ...
            m(2,3) 0 0 0 m(2,4) 0 0 0;
255         0 m(2,1) 0 0 -c(1,2) m(2,2) - c(2,2) -c(3,2) -c(4,2) 0 ...
            m(2,3) 0 0 0 m(2,4) 0 0;
256         0 0 m(2,1) 0 -c(1,3) -c(2,3) m(2,2) - c(3,3) -c(4,3) 0 ...
            0 m(2,3) 0 0 0 m(2,4) 0;
257         0 0 0 m(2,1) -c(1,4) -c(2,4) -c(3,4) m(2,2) - c(4,4) 0 ...
            0 0 m(2,3) 0 0 0 m(2,4);
258         m(3,1) 0 0 0 m(3,2) 0 0 0 m(3,3) - c(1,1) -c(2,1) ...
            -c(3,1) -c(4,1) m(3,4) 0 0 0;
259         0 m(3,1) 0 0 0 m(3,2) 0 0 -c(1,2) m(3,3) - c(2,2) ...
            -c(3,2) -c(4,2) 0 m(3,4) 0 0;
260         0 0 m(3,1) 0 0 0 m(3,2) 0 -c(1,3) -c(2,3) m(3,3) - ...
            c(3,3) -c(4,3) 0 0 m(3,4) 0;
261         0 0 0 m(3,1) 0 0 0 m(3,2) -c(1,4) -c(2,4) -c(3,4) ...
            m(3,3) - c(4,4) 0 0 0 m(3,4);
262         m(4,1) 0 0 0 m(4,2) 0 0 0 m(4,3) 0 0 0 m(4,4) - c(1,1) ...
            -c(2,1) -c(3,1) -c(4,1);
263         0 m(4,1) 0 0 0 m(4,2) 0 0 0 m(4,3) 0 0 -c(1,2) m(4,4) ...
            - c(2,2) -c(3,2) -c(4,2);
264         0 0 m(4,1) 0 0 0 m(4,2) 0 0 0 m(4,3) 0 -c(1,3) -c(2,3) ...
            m(4,4) - c(3,3) -c(4,3);
265         0 0 0 m(4,1) 0 0 0 m(4,2) 0 0 0 m(4,3) -c(1,4) -c(2,4) ...
            -c(3,4) m(4,4) - c(4,4)];
266 end
```

```
267
268 function H = HA(m,c)
269 %Lars Martin - Basis for H_A
270     H = [m(1,1) - c(1,1) m(2,1) m(3,1) m(4,1) -c(1,2) 0 0 0 ...
        -c(1,3) 0 0 0 -c(1,4) 0 0 0;
271          m(1,2) m(2,2) - c(1,1) m(3,2) m(4,2) 0 -c(1,2) 0 0 0 ...
             -c(1,3) 0 0 0 -c(1,4) 0 0;
272          m(1,3) m(2,3) m(3,3) - c(1,1) m(4,3) 0 0 -c(1,2) 0 0 0 ...
             -c(1,3) 0 0 0 -c(1,4) 0;
273          m(1,4) m(2,4) m(3,4) m(4,4) - c(1,1) 0 0 0 -c(1,2) 0 0 ...
              0 -c(1,3) 0 0 0 -c(1,4);
274          -c(2,1) 0 0 0 m(1,1) - c(2,2) m(2,1) m(3,1) m(4,1) ...
             -c(2,3) 0 0 0 -c(2,4) 0 0 0;
275          0 -c(2,1) 0 0 m(1,2) m(2,2) - c(2,2) m(3,2) m(4,2) 0 ...
             -c(2,3) 0 0 0 -c(2,4) 0 0;
276          0 0 -c(2,1) 0 m(1,3) m(2,3) m(3,3) - c(2,2) m(4,3) 0 0 ...
             -c(2,3) 0 0 0 -c(2,4) 0;
277          0 0 0 -c(2,1) m(1,4) m(2,4) m(3,4) m(4,4) - c(2,2) 0 0 ...
              0 -c(2,3) 0 0 0 -c(2,4);
278          -c(3,1) 0 0 0 -c(3,2) 0 0 0 m(1,1) - c(3,3) m(2,1) ...
             m(3,1) m(4,1) -c(3,4) 0 0 0;
279          0 -c(3,1) 0 0 0 -c(3,2) 0 0 m(1,2) m(2,2) - c(3,3) ...
             m(3,2) m(4,2) 0 -c(3,4) 0 0;
280          0 0 -c(3,1) 0 0 0 -c(3,2) 0 m(1,3) m(2,3) m(3,3) - ...
             c(3,3) m(4,3) 0 0 -c(3,4) 0;
281          0 0 0 -c(3,1) 0 0 0 -c(3,2) m(1,4) m(2,4) m(3,4) ...
             m(4,4) - c(3,3) 0 0 0 -c(3,4);
282          -c(4,1) 0 0 0 -c(4,2) 0 0 0 -c(4,3) 0 0 0 m(1,1) - ...
             c(4,4) m(2,1) m(3,1) m(4,1);
283          0 -c(4,1) 0 0 0 -c(4,2) 0 0 0 -c(4,3) 0 0 m(1,2) ...
             m(2,2) - c(4,4) m(3,2) m(4,2);
284          0 0 -c(4,1) 0 0 0 -c(4,2) 0 0 0 -c(4,3) 0 m(1,3) ...
             m(2,3) m(3,3) - c(4,4) m(4,3);
285          0 0 0 -c(4,1) 0 0 0 -c(4,2) 0 0 0 -c(4,3) m(1,4) ...
             m(2,4) m(3,4) m(4,4) - c(4,4)];
286 end
287
288 function M = coordvec2matrix(vec)
289 %Jarle - Transforms a 16x1 coordinate vector to the ...
       corresponding 4x4 matrix
290     M=zeros(4);
291     for i=1:4
292        M(i,:) = vec((i-1)*4+1:i*4);
293     end
294 end
```

Appendix F

An unrealisable polarimeter design

In figure F.1 the inverse condition number of an unrealisable polarimeter is compared to the theoretical inverse condition number of the constructed polarimeter. The design is deemed unrealisable since an FLC acting as a HWP at 800 nm, which the design called for, could not be manufactured. The design was optimised in for use in the range 550 nm to 1150 nm with extra emphasis around 940 nm. Comparing the designs, the realised design performs better in the 500 nm to 840 nm range, while the unrealisable design performs better in the 840 nm to 1300 nm range.

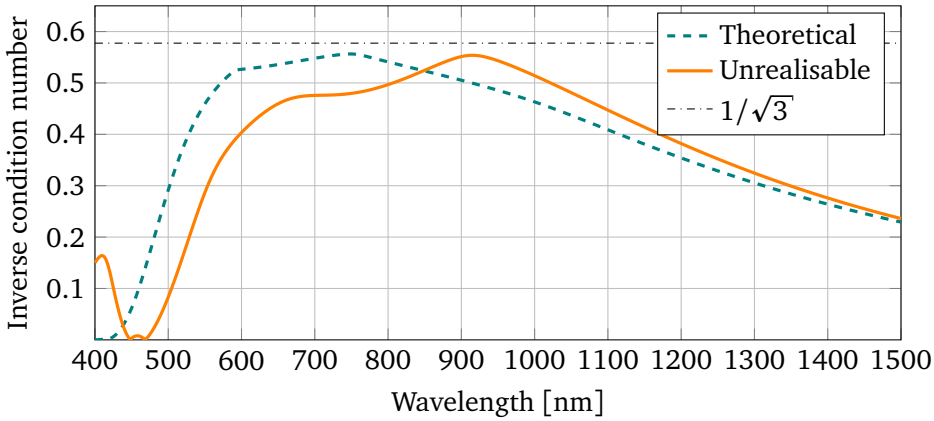

Figure F.1: Example of the inverse condition number of an unrealisable polarimeter design (solid line) compared to the theoretical inverse condition number of the constructed polarimeter (dashed line).

Appendix G

Schematics for uMMI PSG/PSA

See next pages.

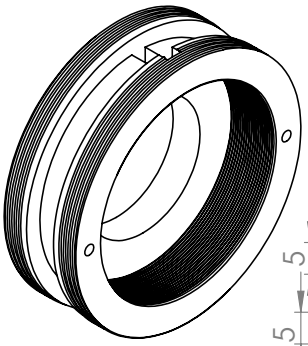

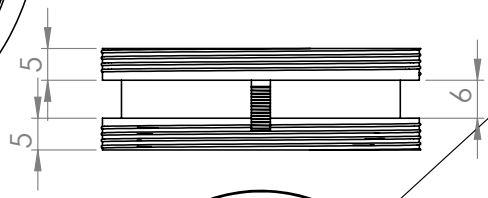

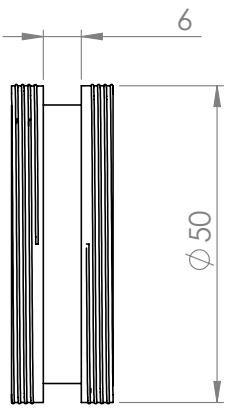

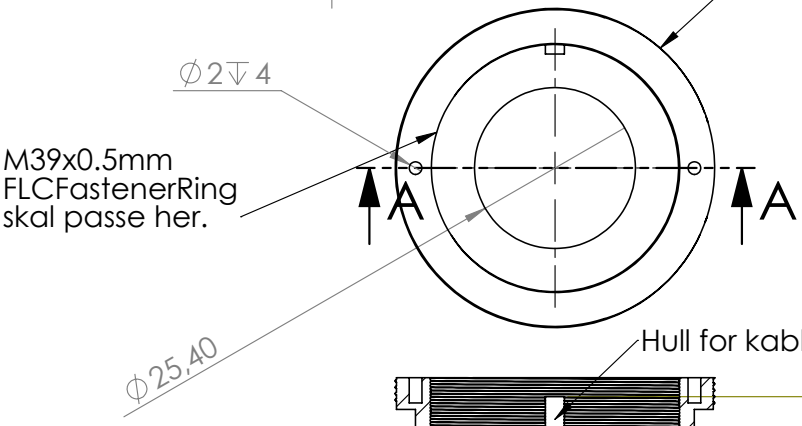

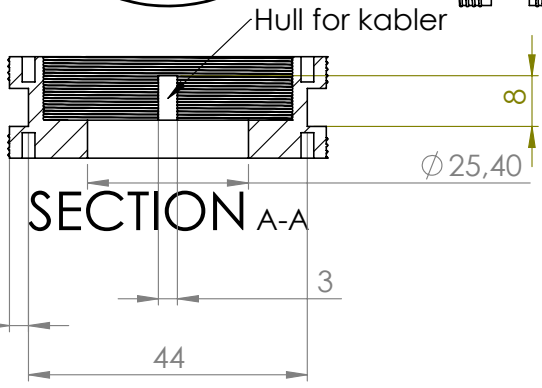

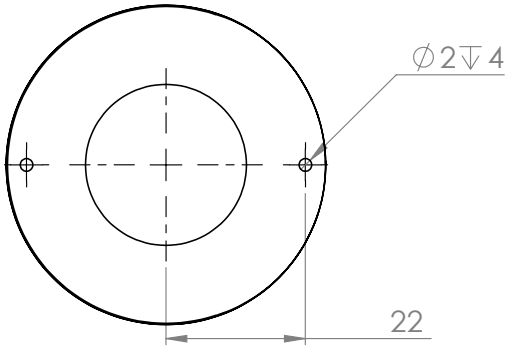

4xAluminium

Vegard Hagen
47903155

UNLESS OTHERWISE SPECIFIED: DIMENSIONS ARE IN MILLIMETERS SURFACE FINISH: TOLERANCES: LINEAR: ANGULAR:		FINISH:		DEBUR AND BREAK SHARP EDGES	DO NOT SCALE DRAWING	REVISION
	NAME	SIGNATURE	DATE		TITLE:	
DRAWN						
CHK'D						
APPV'D						
MFG						
Q.A				MATERIAL	DWG NO. FLCholder	A4
				WEIGHT:	SCALE:1:1	SHEET 1 OF 1

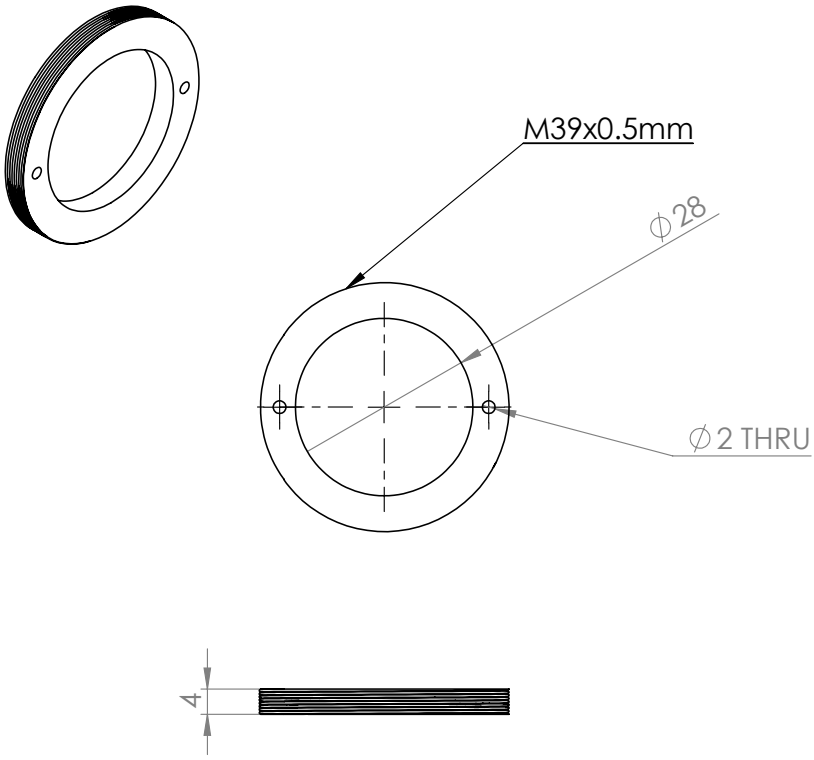

Festering til å montere inne i FLCholder.
Gjengene trenger ikke være like fine som angitt.

4xAluminium

Vegard Hagen
47903155

UNLESS OTHERWISE SPECIFIED: DIMENSIONS ARE IN MILLIMETERS SURFACE FINISH: TOLERANCES: LINEAR: ANGULAR:	FINISH:		DEBUR AND BREAK SHARP EDGES	DO NOT SCALE DRAWING	REVISION	
	NAME	SIGNATURE	DATE	TITLE:		
DRAWN						
CHK'D						
APPV'D						
MFG						
Q.A				DWG NO.	FLCfastenerRing	A4
			WEIGHT:	SCALE:1:1	SHEET 1 OF 1	

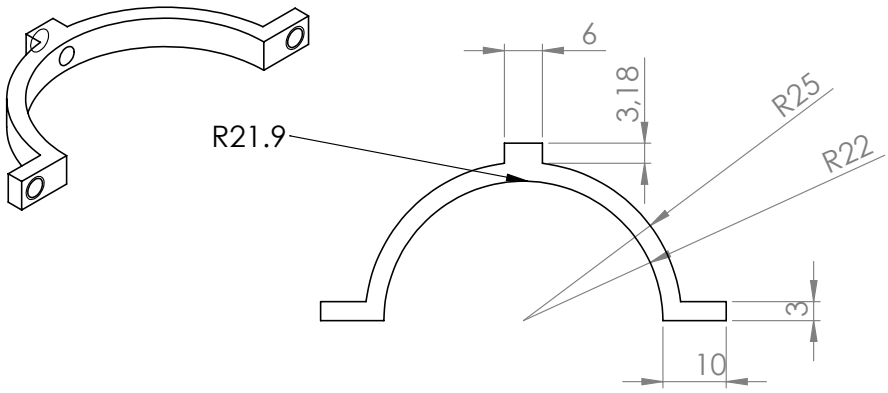

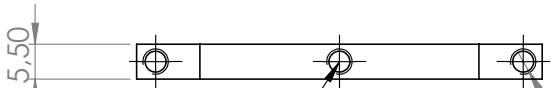

3 x ∅ 3,30 THRU ALL
M4 - 6H THRU ALL

For Thorlabs Ø1/2" Stainless Steel Optical Posts
#8-32

2+2 i aluminium.

Vegard Hagen
47903155

UNLESS OTHERWISE SPECIFIED: DIMENSIONS ARE IN MILLIMETERS SURFACE FINISH: TOLERANCES: LINEAR: ANGULAR:		FINISH:		DEBUR AND BREAK SHARP EDGES	DO NOT SCALE DRAWING	REVISION
	NAME	SIGNATURE	DATE		TITLE:	
DRAWN						
CHK'D						
APPV'D						
MFG						
Q.A				MATERIAL	DWG NO.	A4
					Post	
				WEIGHT:	SCALE:1:1	SHEET 1 OF 1

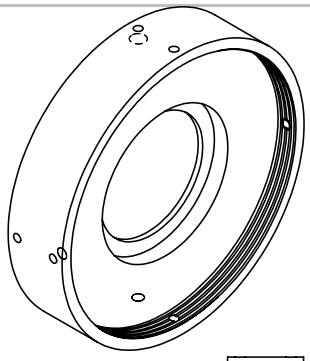

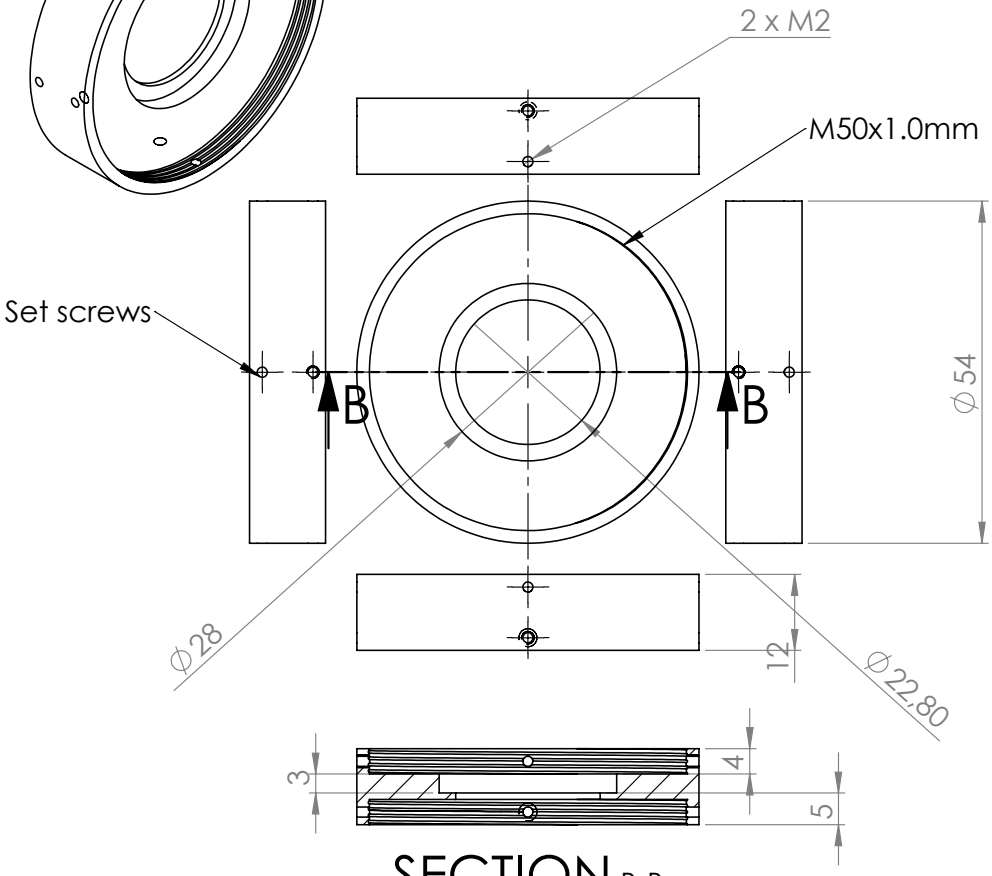

SECTION B-B

4xaluminium

Vegard Hagen

UNLESS OTHERWISE SPECIFIED: DIMENSIONS ARE IN MILLIMETERS SURFACE FINISH: TOLERANCES: LINEAR: ANGULAR:	FINISH:		DEBUR AND BREAK SHARP EDGES	DO NOT SCALE DRAWING	REVISION	
	NAME	SIGNATURE	DATE	TITLE:		
DRAWN						
CHK'D						
APPV'D						
MFG						
Q.A				DWG NO.	WPholder	A4
			WEIGHT:	SCALE:1:1	SHEET 1 OF 1	

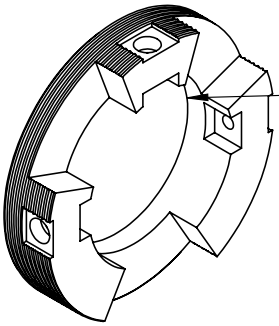

PolHolderB skal passe inni her kun én vei.
Designet må sikkert endres litt på.

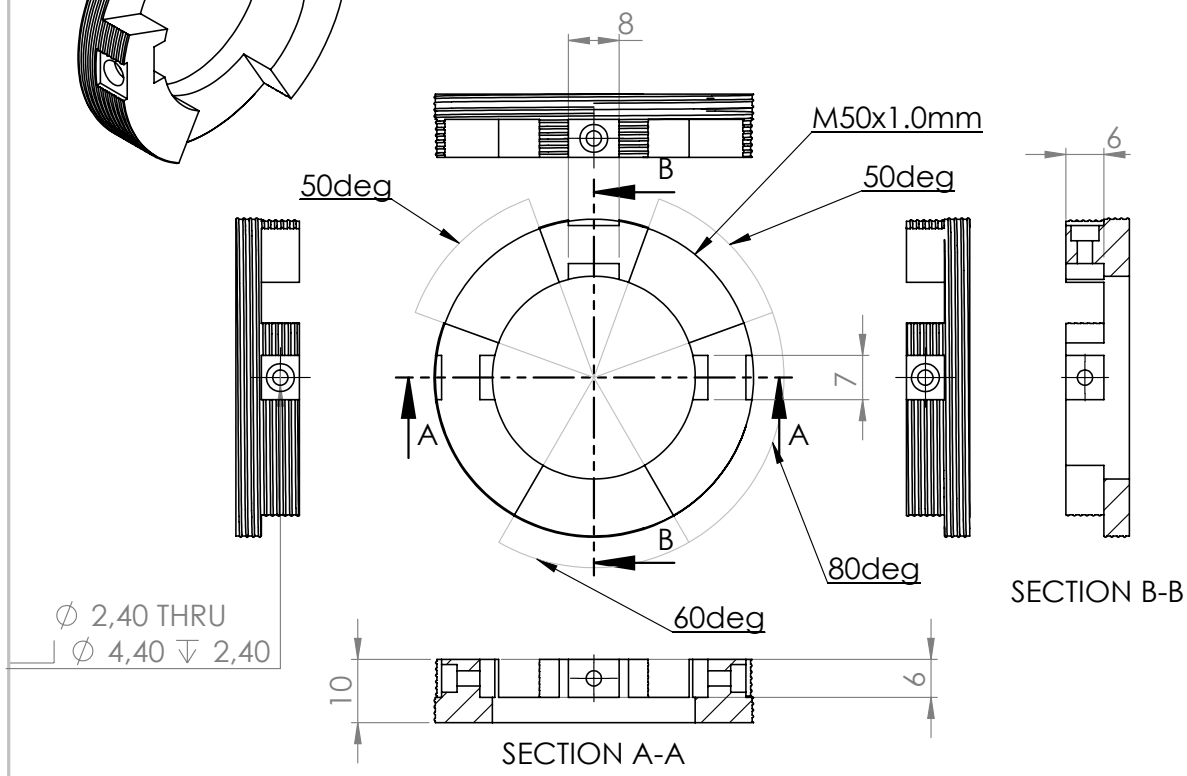

SECTION B-B

SECTION A-A

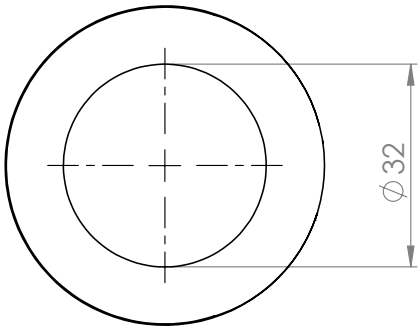

2xAluminium

Vegard Hagen
47903155

UNLESS OTHERWISE SPECIFIED: DIMENSIONS ARE IN MILLIMETERS SURFACE FINISH: TOLERANCES: LINEAR: ANGULAR:	FINISH:		DEBUR AND BREAK SHARP EDGES		DO NOT SCALE DRAWING	REVISION
	NAME	SIGNATURE	DATE		TITLE:	
DRAWN						
CHK'D						
APPV'D						
MFG						
Q.A				MATERIAL	DWG NO.	A4
					PolHolderA	
				WEIGHT:	SCALE:1:1	SHEET 1 OF 1

Denne delen skal kunne passe inn i PolHolderA

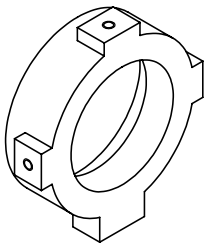

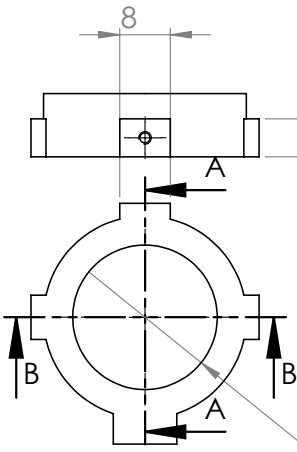

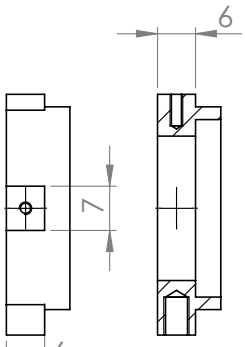

SECTION A-A

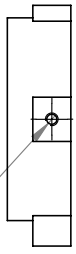

∅ 1,60 ↧ 5
M2 - 6H ↧ 5

∅22,80

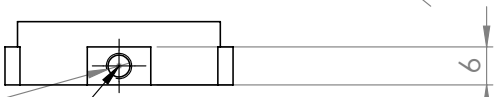

∅ 3,45 ↧ 6
8-32 UNC ↧ 6

For Thorlabs Ø1/2" Stainless Steel Optical Posts

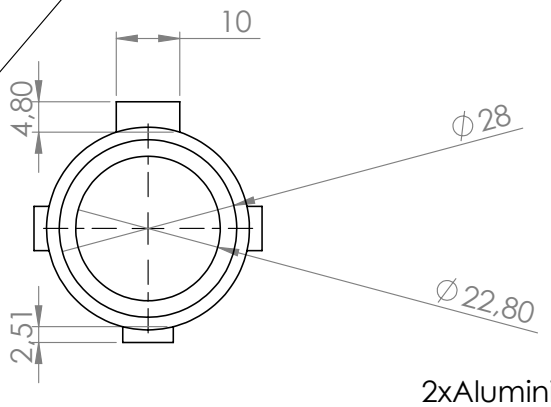

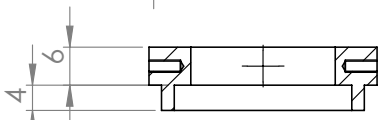

SECTION B-B

2xAluminium

Vegard Hagen
47903155

UNLESS OTHERWISE SPECIFIED: DIMENSIONS ARE IN MILLIMETERS SURFACE FINISH: TOLERANCES: LINEAR: ANGULAR:		FINISH:		DEBUR AND BREAK SHARP EDGES	DO NOT SCALE DRAWING	REVISION
	NAME	SIGNATURE	DATE		TITLE:	
DRAWN						
CHK'D						
APPV'D						
MFG						
Q.A				MATERIAL	DWG NO. PolHolderB	A4
				WEIGHT:	SCALE:1:1	SHEET 1 OF 1

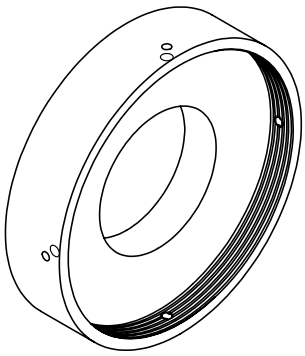

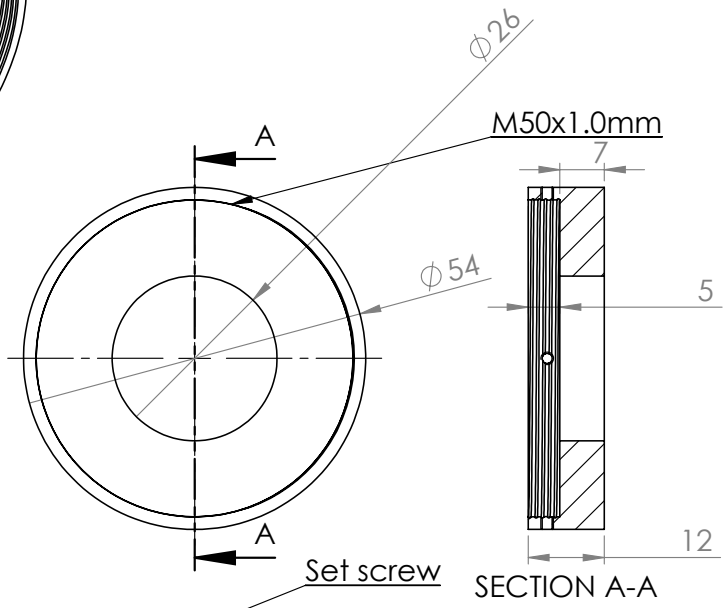

∅ 1,60 THRU ALL
M2 - 6H THRU ALL

4 x ∅ 2,26 ↧ 5
4-40 UNC ↧ 4,60

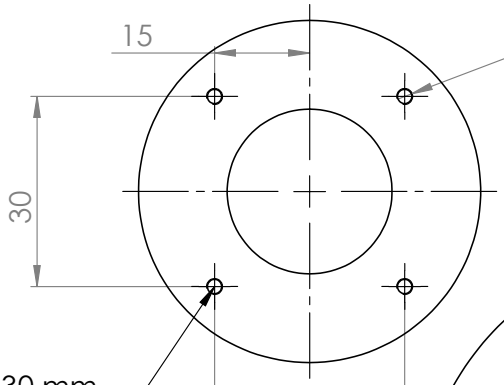

2xAluminium

Vegard Hagen
47903155

For ThorLabs 30 mm
cage rods
#4-40

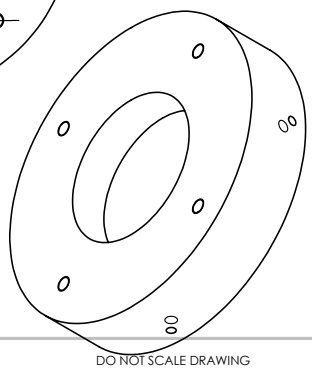

UNLESS OTHERWISE SPECIFIED: DIMENSIONS ARE IN MILLIMETERS SURFACE FINISH: TOLERANCES: LINEAR: ANGULAR:	FINISH:		DEBUR AND BREAK SHARP EDGES		DO NOT SCALE DRAWING	REVISION
	NAME	SIGNATURE	DATE			TITLE:
DRAWN						
CHK'D						
APPV'D						
MFG						
Q.A				MATERIAL		DWG NO. CageMount
						A4
				WEIGHT:	SCALE:1:1	SHEET 1 OF 1

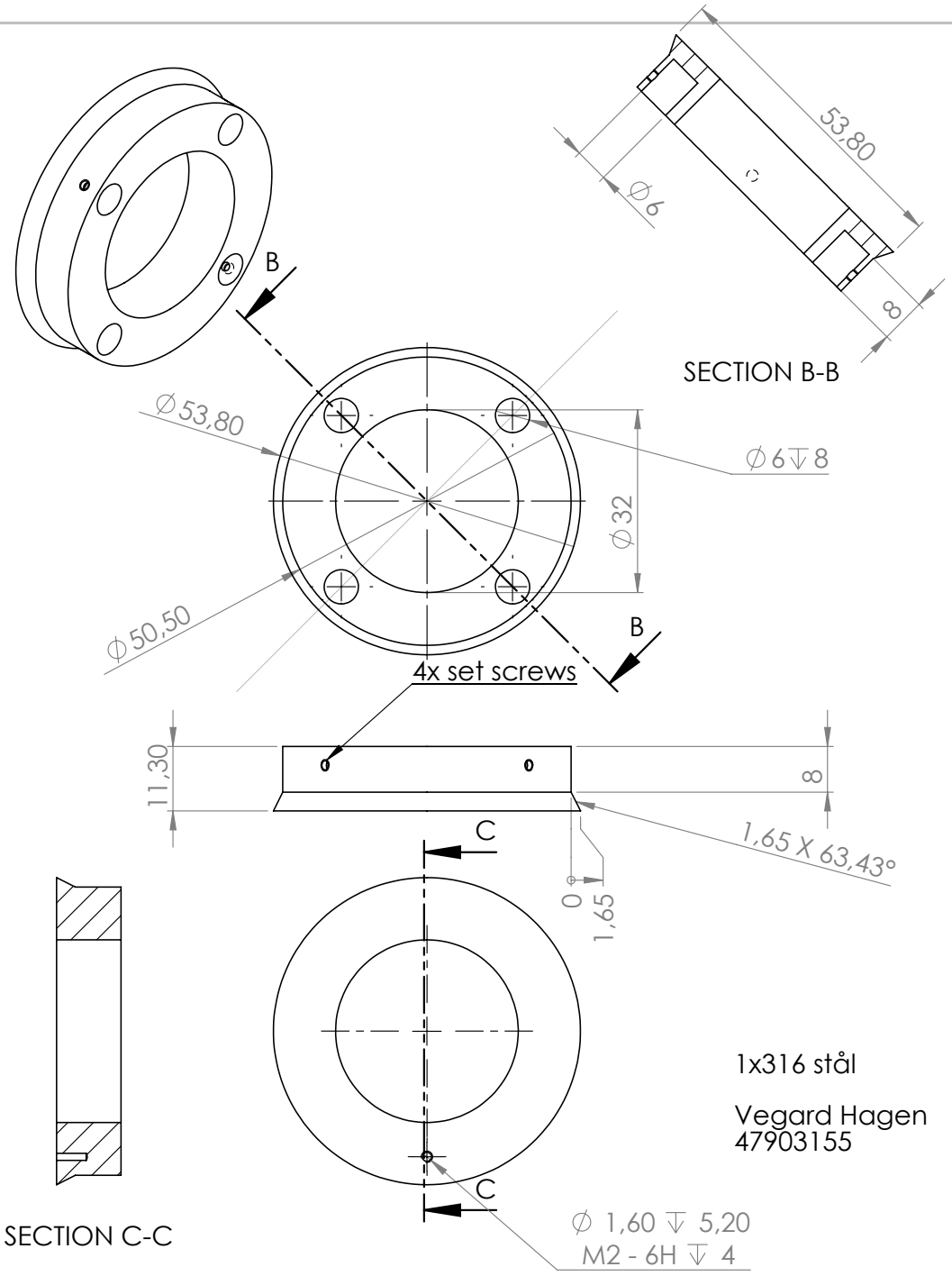

UNLESS OTHERWISE SPECIFIED: DIMENSIONS ARE IN MILLIMETERS SURFACE FINISH: TOLERANCES: LINEAR: ANGULAR:	FINISH:		DEBUR AND BREAK SHARP EDGES		DO NOT SCALE DRAWING	REVISION
	NAME	SIGNATURE	DATE			TITLE:
DRAWN						
CHK'D						
APPV'D						
MFG						
Q.A				MATERIAL		DWG NO. MicroscopeAdapter A4
				WEIGHT:	SCALE:1:1	SHEET 1 OF 1

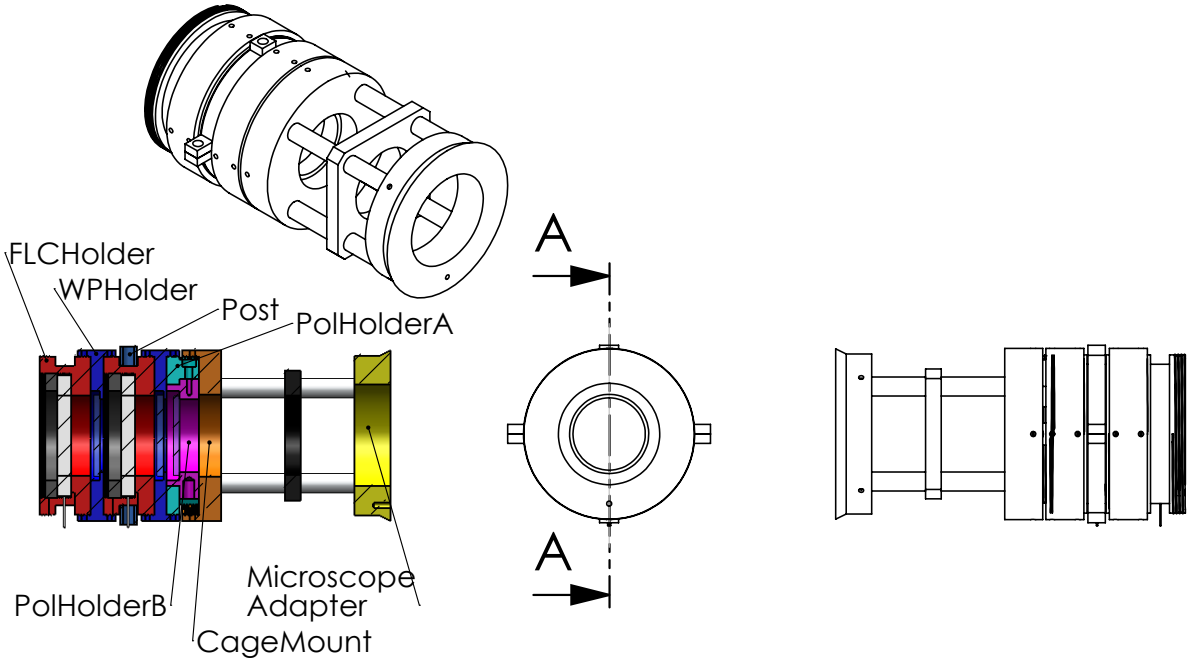

SECTION A-A

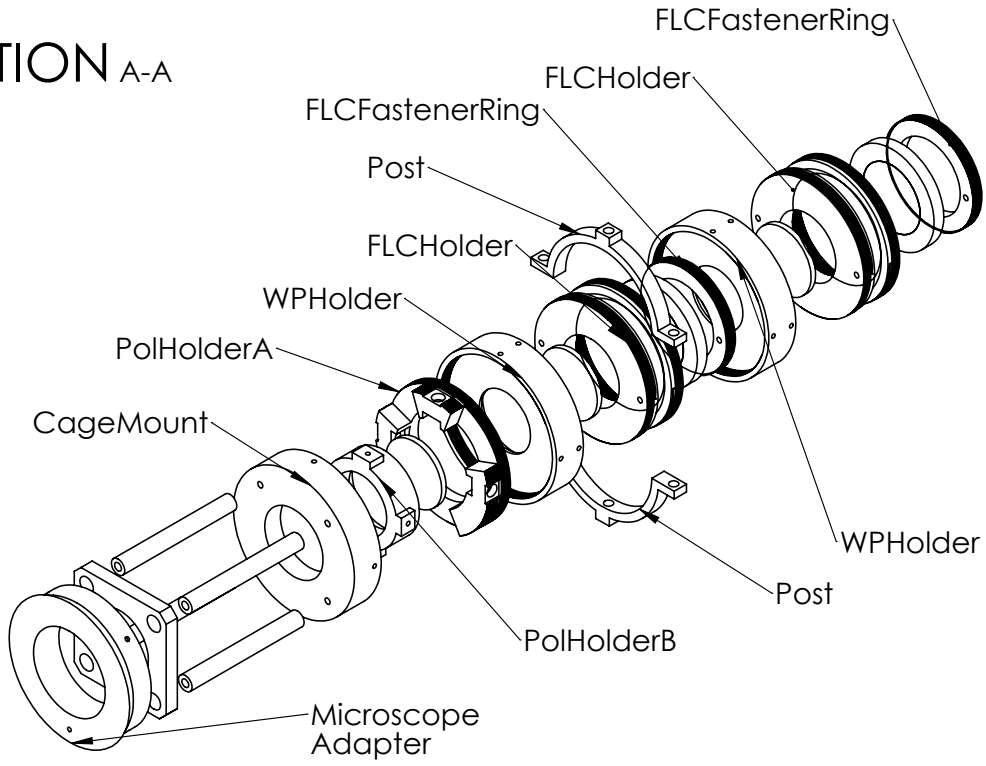

UNLESS OTHERWISE SPECIFIED: DIMENSIONS ARE IN MILLIMETERS SURFACE FINISH: TOLERANCES: LINEAR: ANGULAR:	FINISH:	DEBUR AND BREAK SHARP EDGES	DO NOT SCALE DRAWING	REVISION	
	NAME	SIGNATURE	DATE	TITLE:	
DRAWN					
CHK'D					
APPV'D					
MFG					
Q.A				DWG NO.	A4
				Holder	
			WEIGHT:	SCALE:1:2	SHEET 1 OF 1

Appendix H

Datasheet for CODIXX colorPol VISIR polarisers

See next page.

CODIXX

glass sheet polarizer

colorPol® VISIR 003589

linear VIS-NIR-polarizer Date: 15.07.2005

Wavelength range with **contrast > 100 000 : 1** (Contrast = ratio of parallel and perpendicular transmittance)	600 to 1200 nm
Transmittance (uncoated)	> 67 % up to 84 %
Wavelength range with **contrast > 10 000 : 1**	550 to 1500 nm
Transmittance (uncoated)	> 57 % up to 85 %

Spectral response

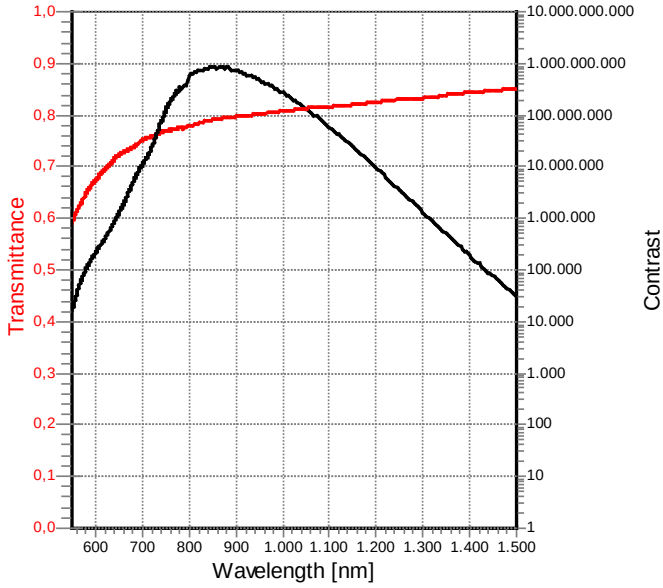

Filter thickness	2,0 ± 0,2 mm

Filter size

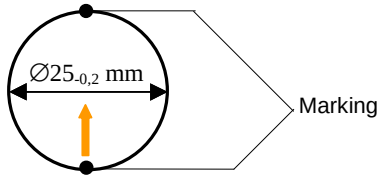

Polarization (electric field vector of transmitted light)

Clear aperture	90 % of surface dimension
Wavefront distortion (Ø10 mm)	< λ/4 at 633 nm
Acceptance angle	± 20°
Operating temperature	-20 .. +120 ℃

CODIXX AG
Betrieb Barleben
Steinfeldstraße 3
D – 39179 Barleben (Germany)

Phone: +49 39203 963 0
Fax: +49 39203 963 33
http://www.codixx.de
colorPol@codixx.de

Glossary

The following is an excerpt from Handbook of Optics.[10]

Analyser An element whose intensity transmission is proportional to the content of a specific polarisation state in the incident beam. Analysers are placed before the detector in polarimeters. The transmitted polarisation state emerging from an analyser is not necessarily the same as the state which is being analysed.

Birefringence A material property, the retardance associated with propagation through an anisotropic medium. For each propagation direction within a birefringent medium, there are two modes of propagation with different refractive indices n_1 and n_2. The birefringence Δn is $\Delta n = |n_1 - n_2|$.

Depolarisation A process which couples polarised light into unpolarised light. Depolarisation is intrinsically associated with scattering and with diattenuation and retardance which vary in space, time, and/or wavelength.

Diattenuation The property of an optical element or system whereby the intensity transmittance of the exiting beam depends on the polarisation state of the incident beam. The intensity transmittance is a maximum $P_{\max}$ for one incident state, and a minimum $P_{\min}$ for the orthogonal state. The diattenuation is defined as $(P_{\max} - P_{\min})/(P_{\max} + P_{\min})$.

Diattenuator Any homogeneous polarisation element which displays significant diattenuation and minimal retardance. Polarisers have a diattenuation close to one, but nearly all optical interfaces are weak diattenuators. Examples of diattenuators include the following: polarisers and dichroic materials, as well as metal and dielectric interfaces with reflection and transmission differences described by Fresnel equations; thin films (homogeneous and isotropic); and diffraction gratings.

Dichroism The material property of displaying diattenuation during propagation. For each direction of propagation, dichroic media have two modes of propagation

with different absorption coefficients. Examples of dichroic materials include sheet polarisers and dichroic crystals such as tourmaline.

Eigenpolarisation A polarisation state transmitted unaltered by a polarisation element except for a change of amplitude and phase. Every polarisation element has two eigenpolarisations. Any incident light not in an eigenpolarisation state is transmitted in a polarisation state different from the incident state. Eigenpolarisations are the eigenvectors of the corresponding Mueller or Jones matrix.

Ellipsometry A polarimetric technique which uses the change in the state of polarisation of light upon reflection for the chatacyerisation of surfaces, interfaces, and thin films (after Azzam, 1993).

Homogeneous polarisation element an element whose eigenpolarisations are orthogonal. Then, the eigenpolarisations are the states of maximum and minimum transmittance and also of maximum and minimum optical path length. A homogeneous element is classified as linear, circular, or elliptical depending on the form of the eigenpolarisations.

Inhomogeneous polarisation element an element whose eigenpolarisations are not orthogonal. Such an element will display different polarisation characteristics for forward and backward propagating beams. The eigenpolarisations are generally not the states of maximum and minimum transmittance. Often inhomogeneous elements cannot be simply classified as linear, circular, or elliptical.

Ideal polariser A polariser with an intensity transmittance of one for its principal state and an intensity transmittance of zero for the orthogonal state.

Linear polariser A device which, when placed in an incident unpolarised beam, produces a beam of light whose electric field vector is oscillating primarily in one plane, with only a small component in the perpendicular plane (after Benner, 1993).

Nonpolarising element An element which does not change the polarisation state for arbitrary states. The polarisation state of the output light is equal to the polarisation state of the incident light for all possible input polarisation states.

Parially polarised light light containing an unpolarised component; cannot be extinguished by an ideal polariser.

Polarimeter an optical instrument for the determination of the polarisation state of a light beam, or the polarisation-altering properties of a sample.

Polarimetry The science of measuring the polarisation state of a light beam and the diattenuating, retarding, and depolarising properties of materials.

Polarisation any process which alters the polarisation state of a beam of light, including diattenuation, retardance, depolarisation, and scattering.

Polarisation coupling Any conversion of light from one polarisation state into another state.

Polarised light light in a fixed, elleiptically (including linearly or circularly) polarised state. It can be extinguished by an ideal polariser. For polychromatic light, the polarisation ellipses associated with each spectral component have identical ellipticity, orientation, and helicity.

Polariser A strongly diattenuating optical element designed to transmit light in a specified polarisation state independent of the incident polarisation state. The transmission of one of the eigenpolarisations is very nearly zero.

Polarisation element Any optical element which alters the polarisation state of light. This includes polarisers, retarders, mirrors, thin films, and nearly all optical elements.

Pure diattenuator A diattenuator with zero retardance and no depolarisation.

Pure retarder A retarder with zero diattenuation and no depolarisation.

Retardance A polarisation-dependent phase change associated with a polarisation element or system. The phase (optical path length) of the output beam depends upon the polarisation state of the input beam. The transmitted phase is a maximum for one eigenpolarisation, and a minimum for the other eigenpolarisation. Other states show polarisation coupling and an intermediate phase.

Retardation plate a retarder constructed from a plane parallel plate or plates of linearly birefringent material.

Retarder A polarisation element designed to produce a specified phase difference between the exiting beams for two orthogonal incident polarisation states (the eigenpolarisations of the element). For example, a quarter-wave linear retarder has as its eigenpolarisations two orthogonal linearly polarised states which are transmitted in their incident polarisation states, but with a 90° (quarter-wavelength) relative phase difference introduced.

Spectropolarimetry The spectroscopic study of the polarisation properties of materials. Spectropolarimetry is a generalisation of conventional optical spectroscopy. Where conventional spectroscopy endeavours to measure the reflectance or transmission of a sample as a function of wavelength, spectropolarimetry also determines the diattenuating, retarding, and depolarising properties of the sample. Complete characterisation of these properties is accomplished by measuring the Mueller matrix of the sample as a function of wavelength.

Waveplate A retarder.